ULB FACULTÉ DES SCIENCES

UNIVERSITÉ LIBRE DE BRUXELLES

Full Off-Specular and Specular Reflectometry for Soft Thin Film Analysis

Thesis submitted by Aljoša HAFNER

in fulfilment of the requirements of the PhD Degree in Sciences
(ULB - ”Docteur en sciences”)

Academic year 2018 – 2019

Supervisors :
Prof. Michele SFERRAZZA (Université libre de Bruxelles)
Dr. Philipp GUTFREUND (Institut Laue - Langevin)

NEUTRONS FOR SOCIETY

Université Libre de Bruxelles, Brussels, Belgium
Department of Physics
Institut Laue - Langevin, Grenoble, France
Large Scale Structures group

Aljoša Hafner

Full Off-Specular and Specular Reflectometry for Soft Thin Film Analysis

PhD thesis

Supervisor | Prof. Michele Sferrazza
ILL Co-Supervisor | Dr. Philipp Gutfreund

2019

Abstract

Specular reflectivity (SR) and off-specular neutron scattering (OSS) are non-destructive scattering techniques, which, through deuteration (exchange of hydrogen atoms with deuterium), give a high contrast even among very similar chemical species and are therefore highly suitable for investigations of soft thin films. While readily available software exists for analysis of SR, there are no such existing tools for OSS. Through a combination of both, the former yielding a density profile in the direction normal to the sample surface and the latter yielding an in-plane lateral structure at each of the buried interfaces, one can obtain detailed information of buried morphology on length scales ranging from $\sim$ Å to $\sim 10\,\mu$m. OSS analysis was developed to analyze buried interfaces in absolute scale, with only structural parameters being free. Moreover, the SR and OSS are intricately linked and have to be fitted to the data simultaneously, constraining the model to a high degree. The OSS was applied to investigation of soft interfaces as model systems.

The stability and instability of thin polymer layers have been studied extensively in the last decades, both as their applications as coatings have become part of our daily life, and in fundamental soft matter research. The mechanism of immiscible polymer film decomposition was investigated by preparing bilayers of deuterated polystyrene (d-PS) and protonated poly(methyl methacrylate) (h-PMMA) of different thicknesses on Si substrates. The in-plane lateral cutoff length was measured at the PS/PMMA interface as a function of d-PS thickness. For preannealed films with thickness $d_{\mathrm{dPS}} < 250\,$Å, the result follows the prediction of the capillary waves cutoff length. For thicker films, spontaneous nucleation of the top layer, with a clear OSS signature, was observed. This was also the case for the non-preannealed samples, showing that preannealing causes irreversible adsorption on the substrate and thus stabilizes the layer.

The bilayers were then measured also as a function of annealing time, measuring the nucleation of the top layer from the beginning. The measurements show that the breakup starts immediately after the start of annealing. For a sufficiently thick PMMA layer, the expected PS/PMMA interfacial width was measured. Different cutoff lengths were measured at different regimes of nucleation. Furthermore, a thick/thin/thick PMMA/PS/PMMA trilayer was prepared on an Si substrate, isolating the influence of the substrate to study the hypothesized spinodal dewetting of the thin layer. The roughnesses of the interfaces of the thin layer grow with the same rate and their peaks and valleys are supposed to oscillate in anti-phase. As the simulation subsequently showed, the difference between the in-phase and anti-phase oscillations is too small to be measured with the current instruments. The minimum detectable amount of material would be 3 stacked repeating units of PMMA/PS/PMMA, where the results of the simulations show a noticeable difference. Such a system was measured and is qualitatively compared to the simulations.

Contents

1 Introduction

Neutron scattering

Scattering of radiation with matter is one of the fundamental processes in physical science. It involves the description of the interaction of radiation being altered (either in direction or energy) when passing through a medium. This involves many different forms of radiation, from sound waves and long electromagnetic waves, down to particle interaction with molecules and atoms. The properties of radiation (such as wavelength or particle type) determine the interaction mechanisms and thus the observables of the experiment. By changing the particle type, one selects the sensitivity of the probe to different inhomogeneities or contrast in the samples. The same sample will therefore look different whether investigated with infrared photons, electrons, X-rays or neutrons, each yielding complementary information. It is because of this that, although providing unique results, a single technique will often not yield sufficient information for a full description of the system. Scattering facilities and laboratories these days are equipped with a wide variety of different analytical techniques in order to help with data analysis.

Neutron scattering is, as its name suggests, a technique, where a sample is placed into a neutron beam and the scattered neutrons are recorded by a detector. Since neutrons are one of the constituents of the nucleus, which is held together by the strong nuclear force, it is not a trivial task to produce them. On its own, a free neutron is unstable, with a mean lifetime of a little bit under $t = 15\,\mathrm{min}$. The exact value is still a part of ongoing research [1]. The source of neutrons in experiments is usually one of the two types: a nuclear reactor or a spallation source. Since all the experiments in this thesis were performed at the Institut Laue - Langevin (ILL), only a reactor source is briefly described. The fission reaction:

$$\mathrm{n} + {}^{235}_{92}\mathrm{U} \rightarrow \text{Fission product 1} + \text{Fission product 2} + 3\,\mathrm{n}, \tag{1.1}$$

produces 3 neutrons in the core of the reactor. The neutrons are then slowed down by moving through the so-called moderator, which in the ILL case is heavy water. In order to have a low enough wavelength to be used for most of the experiments, some of them are further slowed down by moving through a so-called cold source (liquid deuterium). Due to their large penetration depth and very weak interaction with almost any material, it is very hard to focus and transport them. The neutron guides exploit the phenomenon of total external reflection (neutron refractive index for most of materials is below 1)

and bring a substantial portion of the, by now slow, neutrons to the instruments. The experiments are roughly divided into elastic and inelastic experiments, meaning either diffraction or energy loss/gain experiments, such as spectroscopy or backscattering [2].

Reflectometry

One of the elastic neutron scattering techniques is reflectometry, where an incoming beam of neutrons impinges on the sample at very low angles, defined by a narrow slit, and is then reflected through a receiving slit into the detector at the angle equal to the incoming one. The ratio between the number of reflected and transmitted neutrons is called reflectivity and is generally recorded as a function of momentum transfer. The data from neutron experiments is generally analyzed within the scope of weak scattering regime in Born approximation, meaning single scattering events by plane waves. However, due to the low angles involved and the specular condition, reflectivity is readily calculated using Fresnel optical methods, namely Parratt's recursive algorithm or Abelès optical matrix method [3], [4], [5]. Contrasting with the Born approximation, the latter are dynamical theories and provide an exact solution of reflectivity. However, this is only valid for ideally flat interfaces, which do not exist in reality. For most of the purposes, the dynamical theory is corrected for this by introducing the so-called Nevot-Croce factors [6], which correctly describe a majority of real-world interfaces by assuming that the height deviations from the ideal interface are normally distributed. Due to neutron contrast being sensitive to the nucleus, different isotopes appear as distinct media. This can be exploited very favorably in soft matter studies, replacing hydrogen with deuterium. In this way, even chemically identical species can be investigated. It was demonstrated that the Flory-Huggins interaction parameter χ for deuterated and protonated species is almost the same. Therefore, such isotope replacement does not significantly alter the thermodynamical properties [7]. Another property making the neutron a suitable tool for biological [8], [9] or soft matter applications [10] is its very short wavelength (its energy being on the order of $E \sim$ meV). Finally, due to the lack of electric charge, it is a highly penetrative probe, enabling in-situ investigations of various systems.

Allowing for detection of scattering into the angles different to the incoming, we get the so-called off-specular scattering. This can either be achieved by changing the outgoing angle, but is usually done by placing a large 2D detector instead. It arises either from the roughness of the layers, scattering diffusely into different directions, or scattering into specific angles due to periodic inhomogeneities in the sample. The first thing to note when doing so is the greatly reduced intensity of the beam reflected into angles different than specular. This posed an important challenge in the past, limiting the practical use of the off-specular scattering technique if compared with X-rays. Due to the angles being different, the exact solution of the problem becomes impossible and various approximation methods have been developed. Most of the initial progress comes from X-rays [11], [12], [13], however, despite the treatment applied to the two probes being very similar, the results cannot be applied immediately to neutrons [14]. Thanks to more and more

neutron reflectometers being equipped with new, highly efficient ^{3}He 2D detectors, the improved neutron flux at the sample position, as well as lower background obtained by optimizing the instruments, off-specular scattering is coming into general use of the neutron scattering community. Moreover, when measuring the specular reflectivity at such improved instruments, the off-specular part is readily recorded alongside the specular. It is therefore much easier to assess whether a dedicated measurement is necessary or not. In the past, most of the off-specular neutron development was done for the description of the relatively strong scattering coming from magnetic thin-layer systems. These show periodic structures and/or domains of varying magnetization and therefore scatter into discrete lines of high intensity [15], [16], [17]. As mentioned before, the biological [18] and soft matter experiments are readily performed on reflectometers. These systems exhibit features on many different length scales that could greatly benefit from using the additional information provided by the off-specular scattering. However, their features are usually not periodic and are therefore usually visible as diffuse scattering of low intensity [19].

With more and more experiments being performed, there is an ever greater demand for suitable analysis tools. The community has in the past mostly used the off-specular tools designed for X-rays. However, these cannot be applied directly to neutrons due to experimental differences (different coherence length, contrast, focusing, etc.). The treatment that has emerged as the most suitable during the years is to calculate the differential scattering cross-section within the distorted wave Born approximation. Even though a considerable amount of literature on the topic exists, there has so far been no readily available software. One has to note that, due to their generally low contrast between different polymers and more generally organic matter, X-rays have a drawback for probing soft matter, and most of the development has been done on well-defined solid state systems. In this study the existing equations were first implemented for neutrons in a highly modular Python program, and rigorously compared to measurements of real systems prepared and performed by us. The program and its workflow does not only allow for the calculation of the differential scattering cross-section, but also allows for easy treatment of data obtained from different instruments, in different representations of reciprocal space, and access to highly capable plotting tools available in the matplotlib library of Python [20].

After performing several experiments it became obvious that in order to provide an effective tool for soft matter, the specular and off-specular parts have to be unified in a common framework, which will allow for scattering to be calculated in absolute intensity. This means that no additional scaling factors or free parameters are available. This restricts the calculation to a high degree, as it links the specular reflectivity and the off-specular scattering, which to our knowledge has not been performed before on such systems. The results obtained from such procedure are highly reliable and thus make off-specular scattering an additional constraint and information which has to fit with the model.

Short- and long- range force at interfaces

As model systems for our experiments, we have selected thin polymer films. These systems have been a focus of a number of studies in the last decades. Some of the most interesting phenomena arise due to geometrical confinement effects when the films get thinner. Most notably, confinement even has influence on macroscopic physical properties, such as the glass transition temperature [21].
The phenomenon of dewetting is a process where a liquid on a surface subsequently withdraws via a spontaneous process and forms distinctive droplet patterns [22]. The instability of thin polymer films is subject to two distinctive forces acting on it and its interfaces. There is a competition between short- and long-range force [23], the former dipolar electrostatic force acting below $< 10\,\text{nm}$, and the latter van der Waals force acting on greater distances $< 100\,\text{nm}$. The short-range forces mostly govern the interfacial properties, such as the interfacial tension. Depending on the strength of the forces, a system of thin films will be either stable or instable. Moreover, experimentally, one can turn the influence of different contributions on or off by preparing thinner or thicker films of various compositions and/or by functionalizing the substrate. A number of studies has been performed in similar fashion in order to reconstruct the effective interfacial potential and other quantities which are otherwise inaccessible and hard to predict [24]. The mechanism of a thin-film breakup is still under investigation, as some studies point into the direction of heterogeneous spontaneous nucleation, where the holes would show a random (Poisson) spatial distribution [25] and others into the direction of spinodal decomposition, showing a preferred length scale λ_s between the holes [26]. It is predicted that for thin films, at least the early stages of spinodal dewetting would follow the Cahn-Hilliard (CH) theory, with a range of instabilities growing the fastest [27]. The CH equation is a mathematical description of a phase separation occurring in a binary blend. The blend spontaneously separates into two domains, each consisting purely of one component [28]. The power of the equation lies in the fact that a characteristic spinodal length scale can be predicted as a function of the second derivative of the effective interfacial potential. The equation was first used to describe the phase separation of binary alloys, but has later been applied to describe spinodal dewetting of polymers [29]. Understanding the process would give us the power to control it and both influence technological applications, as well as understand phenomena where dewetting is present elsewhere, such as in biology [30]. The experimental data, combined with development in theoretical understanding and numerical simulations [31], [32], [33] is therefore of extreme importance for the complete picture.
One of the processes that govern the behavior of the above-lying polymer interface in a system of a polymer layer on a solid substrate, is the process of irreversible adsorption [34]. The exact macromolecular architecture at the interface is still a subject of investigation. It is known that the macromolecules will tend to irreversibly adsorb to an attractive substrate. Each of the monomers will adsorb independently with the energy on the order of kT. However for the molecule to detach, the energy needed is much greater, as all the monomers must be collectively detached [35]. The extent of the adsorbed layer depends on the molecular weight and the annealing time, and it governs

the behavior of films below and around this critical thickness [36], [37].

Neutron scattering has been involved with investigations of phenomena happening in thin polymer films for quite some time, both by specular reflectivity [10], [24], [38] off-specular scattering [39], [40] and grazing incidence scattering [19], [41].

Overview of the thesis

Firstly, neutron reflectometry is geometrically defined in section 2.1.1 and the specular reflectivity case is revisited. Most of the things in the chapter are well known and generally used in neutron reflectometry. However, one of the key components of the off-specular scattering (OSS) algorithm is the calculation of neutron field inside the multilayer, namely the amplitudes of up- and down- ward moving neutrons. In general in the literature, the calculation of the amplitudes is taken directly from X-ray off-specular articles, where the substrate usually has the highest scattering length density (SLD). Due to deuteration and in general a much more varied SLDs of materials for neutrons, one can end up with a mixture of high- and low- SLD materials. Therefore, the X-ray derived algorithms (presented in section 2.1.5) numerically diverge when the momentum transfer is below the critical angle of a material inside the multilayer. A robust algorithm for calculation of the amplitudes, without numerical issues, is derived and described in section 2.1.5 [42].

Secondly, the main part of the thesis is the derivation of the OSS algorithm from the basic assumptions of the distorted wave Born approximation (DWBA) and is described in chapter 2.2. The problem of reciprocal space representation is discussed in the beginning and is crucial for the understanding of different features seen in experimental spectra [43]. Due to neutron reflectometry being performed both in single wavelength mode, where the angle of the detector is changed to vary the momentum transfer, and time-of-flight (ToF) mode, where the incoming and outgoing angles are kept fixed and a band of wavelengths impinges on the sample and is recorded as a function of their speed (i.e. time of flight through the experimental system), the experimental space is either a function of (θ_s, θ_d) or $(\lambda, \theta_s + \theta_d)$, where θ_s and θ_d are the angles from the source and to the detector, and λ is the wavelength. Because the transformations between spaces are not symmetric and linear, a software has been developed to help with re-binning and transforming different measurements [44]. Furthermore, physical phenomena will show differently in different spaces. Should the features come from lateral height deviations proportional to the lateral momentum transfer q_x, they will show as parallel lines in (q_x, q_z) space. On the other hand, if they are coming from optically-related phenomena, such as Yoneda wings or interference of the neutrons inside the sample, then they will show as parallel lines in (p_i, p_f) space, where p_i (p_f) is the projection of the incoming (outgoing) wavevector $\vec{k_i}$ $(\vec{k_f})$ on the perpendicular $z-$ axis.

Furthermore, the general DWBA algorithm and its differential scattering cross-section is developed first for scattering from a single interface and then from a multilayer in 2.2.1. Real interfaces often show a characteristic height-height correlation function [11], [13], [45], which describes the self-affine fractal-like structure as described in section 2.2.3. Two special cases are then presented and the differential scattering cross-section is then

derived for inhomogeneities coming from the interfacial roughness in section 2.2.2 or for inhomogeneities from throughout the layer in section 2.2.4.

The theoretical part of the thesis is rounded off with the description of a straightforward algorithm for the calculation of what we call complete reflectometry. That is a calculation of combined specular reflectivity (with Parratt's formalism) and off-specular scattering (with DWBA). This is done in chapter 3. In the beginning, the scaling of specular to off-specular parts is done by integrating over the incoming and outgoing angle resolutions. This smears the off-specular part, but, more importantly, reduces the infinitesimally small solid angle of reflectivity into a finite, resolution limited specular peak. Furthermore, as one of the integrals represents integration over the Snell's law, the scaling is automatically obtained after this step.

The experimental part consists of two chapters (chap. 4 and chap. 5), both dealing with investigations of buried thin polymer films, using specular and off-specular reflectometry, as well as other auxiliary techniques, namely atomic force microscopy (AFM) and ellipsometry. First, a study on the effect of preannealing of an overlying polymer-polymer interface is presented. For this, two series of polystyrene/poly(methyl methacrylate) (PS/PMMA) bilayer polymer samples with varying PS thickness on silicon (Si) substrates were prepared. Once, the bottom layer was preannealed prior to the deposition of the top layer, to allow the macromolecules to irreversibly adsorb to the substrate. In the other series, the layers were deposited immediately after each other. Both series were then further annealed to reach equilibrium of the polymer/polymer interface. The effect was studied both with specular reflectivity and OSS. The results show a clear difference between the two cases, but also point in the direction of a breakup of the top layer for insufficiently thick PMMA. In the second chapter, several additional PS/PMMA bilayers were investigated. In section 5.2, the non-preannealed system was observed as a function of annealing time, where the process of a breakup of the top layer is followed from the initial stages. All the samples were annealed ex-situ in a vacuum oven and then cooled down to room temperature. In section 5.3, systems with very thick capping PMMA layers were investigated, indeed showing no breakup of the top layers. The polymer-polymer interface was studied in all the cases. However, in order to extract quantitative information out of different contributions to OSS, a series of model systems had to be studied for the algorithm to be verified and, most importantly, for the qualitative information from the measurements to be understood.

In the last part, extensions of the bilayer systems are presented, firstly with three-layer systems of thick-thin-thick polymer on Si substrates in section 5.4, and secondly with multilayers in section 5.5. The full power of the developed OSS algorithm is shown by simulating some exciting interfacial morphologies, such as simultaneous dewetting of multiple polymer-polymer interfaces and their contribution to the experimental spectrum. Due to the nature of OSS, the measurements are burdened with low intensity. However, by predicting the absolute intensity of the scattering in advance, one can predict the possible experimental outcome in advance, both by focusing the measurement to the area of reciprocal space where the expected features have the biggest contribution, and by preparing experimental systems that enhance these features.

2 Specular and off-specular reflectometry

2.1 Specular reflectometry

Neutron reflectometry has by now become an established technique for the analysis of thin layered systems. Not only in soft or hard condensed matter physics, but also in biology, where lipid bilayers are readily investigated [8], [9], [46], [47]. The advantage of (specular) reflectivity over other scattering techniques is that one can analyze the data using optical methods alone and that for a system of ideally flat layers there exists an analytical solution.

X-ray reflectivity was already observed in 1931 by H. Kiessig [48], who measured the total external reflection of X-rays from a Ni mirror. The oscillations coming from layer thickness are called *Kiessig fringes*, after him. Neutron reflectivity was first observed by E. Fermi and W. H. Zinn in 1946 [49], when they reported observation of critical external reflection of neutrons from different materials, namely graphite, glass, aluminium, beryllium, copper, zinc, nickel and iron. Thus they confirmed that the refractive index of those materials for neutrons is smaller than unity, $n < 1$.

Some of the key properties that make the neutron a very suitable probe for soft matter systems are described in the following paragraphs. Firstly, the neutron is neutral and has a spin, therefore it only interacts with the nuclei or the atom's spin. This makes it a highly penetrative and non-destructive probe for measuring buried structures. Additionally, the interaction with the nucleus means that it has different sensitivity to different isotopes of the same element. In the case of polymers, exchanging hydrogen atoms for deuterium, one can achieve a high contrast even between the same chemical species, since the two have different scattering length densities for neutron.

2.1.1 Experimental description of reflectometry

What is called reflectometry is in fact a general word for description of a subset of a more general experimental setup called the grazing incidence geometry. It consists of the so-called specular and off-specular reflectometry and grazing incidence small angle scattering (GISAS). The experiments are defined by a very small incoming angle of radiation impinging on the sample and reflecting under a very shallow angle into the detector. During these measurements, both angles are on the order of a few degrees. A sketch of a typical reflectometer can be seen in figure 2.1 and the whole landscape is

shown in figure 2.4b. As shown in fig. 2.4b, the difference between the two techniques is the variation of either the outgoing angle θ_f in the off-specular scattering (OSS) case or the azimuthal angle Θ_y in GISANS case. Geometrical conditions and constraints make the two techniques sensitive to different length scales.

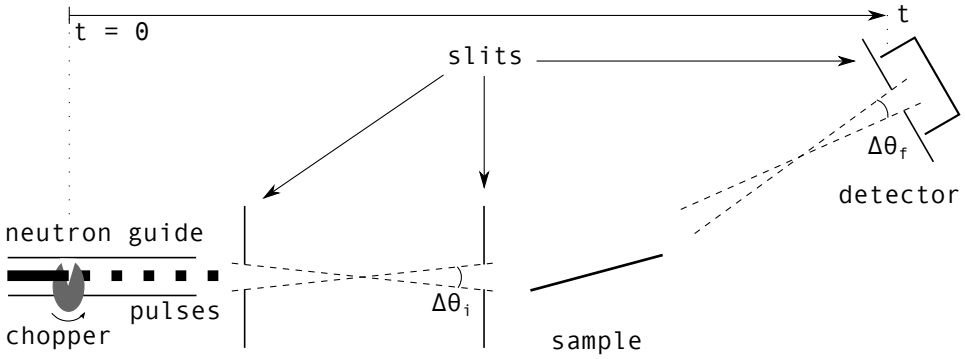

Figure 2.1: Schematic of a time-of-flight reflectometer showing the beam chopper, taking care of its temporal structure and various optical elements.

In specular reflectometry, the scattering intensity is measured as a function of the momentum transfer q_z:

$$q_z = \frac{2\pi}{\lambda} \left(\sin\theta_i + \sin\theta_f\right) , \tag{2.1}$$

with λ being the wavelength, θ_i the incoming angle from the source and θ_f the outgoing angle to the detector. The smearing over q_z consists of 3 contributions, namely the mechanical precision, which today is so good that it can be neglected, and the spread in angles and wavelength, which can be calculated by error propagation as:

$$\frac{\Delta q_z}{q_z} = \sqrt{\left(\frac{\Delta\theta_i + \Delta\theta_f}{2\theta}\right)^2 + \left(\frac{\Delta\lambda}{\lambda}\right)^2} . \tag{2.2}$$

When performing neutron reflectometry, one can use two different modes, namely the time of flight (ToF) or angle dispersive mode. In the first, a white beam of a range of wavelengths impinges on the sample at a constant incoming angle $\theta_i = \theta_0$. The neutrons are detected with a 3D detector with 2 spatial dimensions and a third, temporal dimension. This is due to the fact that the neutron as a non-relativistic mass particle has quite low velocity. Its velocity, wavelength and energy are related through the following expressions:

$$\lambda = \frac{h}{p} = \frac{h}{mv} \text{ and } v = \sqrt{\frac{2E}{m}} = \sqrt{\frac{3k_B T}{m}} , \tag{2.3}$$

with h being the Planck's constant, p being the magnitude of the neutron momentum, E the neutron's energy and k_B the Boltzmann's constant. Cold neutrons with wavelengths

from 2 Å to 27 Å used in reflectometry experiments therefore have speeds from around $2000\,\mathrm{m\,s^{-1}}$ to $150\,\mathrm{m\,s^{-1}}$. Neutrons first pass through a chopper, which marks $t = 0$. Wavelengths of the incoming white beam are then discriminated in the detector based on the time it took the neutrons to pass through the experimental setup. In such case, the wavelength resolution is on the order of a few percent $10^{-2} < \frac{\Delta\lambda}{\lambda} < 10^{-1}$. [50]

The angular spread is controlled with two slits, one just after the chopper and one just in front of the detector. The two slits shown in figure 2.1 determine the divergences $\Delta\theta_i$ and $\Delta\theta_f$ respectively. Furthermore, there is a third slit just in front of the sample in order to constrain the beam size to a desired size. Resolution is a very important aspect, as it often happens that the resolution and sample roughness have the same effect on the measurement, smearing the, otherwise sharp, maxima and minima. The effect of resolution is shown in Fig. 2.2. All the curves are simulations of the same sample with 2 layers, namely h-PMMA and d-PS with 1000 Å and 500 Å on an Si substrate.

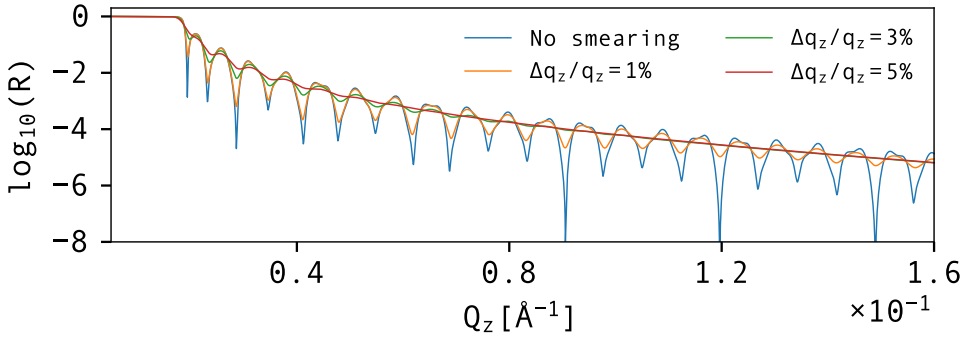

Figure 2.2: Effect of resolution shown in different simulations. The fringes of two different layers are well separated for good resolution and disappear very quickly with only slightly worse conditions.

Generally, only a single Gaussian smearing function is used to describe resolution. Usually the width is chosen so it depends only on q_z, meaning that $\frac{\Delta q_z}{q_z} = \text{const.}$. In order to achieve that, the relative wavelength resolution (the pulse length) is kept constant as $\frac{\Delta\lambda}{\lambda} = \text{const.}$ and the opening of the slits for different angles is adjusted so that $\frac{\Delta\theta}{\theta} = \text{const.}$ In order to record the whole reflectivity curve in a wide q_z range in ToF mode, multiple angles are used.

Unless otherwise stated, all the measurements presented in this thesis were performed on the D17 reflectometer at Institut Laue - Langevin in Grenoble, France [50]. Its neutron guide provides it with one of the highest flux of cold neutrons of any reflectometer in the world, which makes it an ideal setup for off-specular reflectivity. Besides that, it also has a very low background and therefore has a big dynamic range of 7 orders of magnitude. The data was first reduced with COSMOS [51], where background was subtracted and the measurement was integrated and divided with the direct beam intensity.

2.1.2 Reflectivity from a single interface

Scattering length density

For scattering from an assembly of Avogadro's number N_A atoms with scattering lengths b [fm], mass density ρ [g cm^{-3}] and molecular mass M [g mol^{-1}], we can define a macroscopic quantity called the scattering length density (SLD) [2]:

$$Nb = 10^{-29}\frac{N_\mathrm{A}\rho}{M}\sum_{\text{nuclei}} b_{\text{nuclei}}\,. \tag{2.4}$$

The prefactor of 10^{-29} is due to SLD usually being expressed in Å^{-2}:

$$\left[\frac{\frac{\mathrm{g}}{\mathrm{mol\,cm^3}}}{\frac{\mathrm{g}}{\mathrm{mol}}}\mathrm{fm} = \frac{\mathrm{fm}}{\mathrm{cm^3}} = \frac{10^{-5}\,\text{Å}}{10^{24}\,\text{Å}^3} = 10^{-29}\,\text{Å}^{-2}\right]\,. \tag{2.5}$$

Neutron refractive index

In analogous way as for visible light, a refractive index n of a medium can be defined for neutrons. For most materials, the value is $n < 1$. This gives rise to some interesting phenomena which are the basis for neutron reflectivity. Starting with the simplest example of scattering at an interface between two semi-infinite media and implying energy conservation upon scattering, the following relation can be obtained [52]:

$$E_0 = E_1 + V\,, \tag{2.6}$$

with $\hbar$ being the reduced Planck's constant, k being the magnitude of the wavevector, m being the mass of the neutron and $Nb = Nb_1 - Nb_0$ being the scattering length density (SLD) difference of the two materials as defined in eq. 2.4 and

$$E_0 = \frac{\hbar^2k^2}{2m}\;;\; E_1 = \frac{\hbar^2k^2}{2m}n^2\;;\; V = \frac{2\pi\hbar^2}{m}Nb\,. \tag{2.7}$$

The refractive index can then be obtained quickly with some algebra [53]:

$$n^2 = 1 - \frac{4\pi}{k^2}Nb\,, \tag{2.8}$$

with $k = \frac{2\pi}{\lambda}$ and λ being the wavelength of the neutrons, the expression for n is

$$n^2 = 1 - \frac{\lambda^2}{\pi}Nb\,. \tag{2.9}$$

As equation 2.9 shows, n depends only on the neutron wavelength and the SLD of a material. Obeying Snell's law at the interface, with θ_i being the incoming angle of waves coming from the source and $n_0 = 1$ being the refractive index in upper material and θ_t being the angle of waves transmitted into the medium with refractive index n_1:

$$n_0 \cos\theta_i = n_1 \cos\theta_t \,, \tag{2.10}$$

and then setting the transmitted angle $\theta_t = 0$. After Taylor expansion we can then obtain an expression for the critical angle of total external reflection θ_c:

$$\theta_c \approx \lambda\sqrt{\frac{Nb}{\pi}} \,, \tag{2.11}$$

or expressed as critical momentum transfer q_c:

$$q_c = 4\sqrt{\pi Nb} \,. \tag{2.12}$$

For angles below the critical angle, all the neutrons get externally reflected, therefore showing a plateau of reflectivity.

Fresnel reflection and transmission coefficients

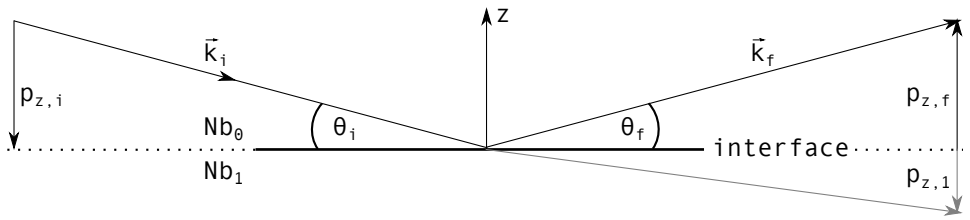

Figure 2.3: Schematic of specular reflectivity, the conditions are: $\theta_i = \theta_f$ and $|p_{z,i}|= |p_{z,f}|$. The momentum transfer is equal to $Q_z = p_{z,f} - p_{z,i} = \frac{4\pi}{\lambda}\sin\theta$. Further in the text, the index z is omitted and p is used to denote the projection of $\vec{k}$ on the z axis.

Consider a single interface between two semi-infinite media, where $p_{z,0}$ and $p_{z,1}$ are the projections of the wavevector $\vec{k}$ of incoming waves on the $z-$ axis above (0) and below (1) the interface as shown in figure 2.3. They can be calculated as:

$$p_{z,1} = \sqrt{p_{z,0}^2 - p_{z,c}^2} = \sqrt{p_{z,0}^2 - 4\pi(Nb_1 - Nb_0)} \,, \tag{2.13}$$

where $p_{z,0} = |\vec{k}|\sin\theta_i$ with θ_i being the angle of the waves coming from the source, $|\vec{k}|= \frac{2\pi}{\lambda}$ being the magnitude of the wavevector, $p_{z,c}$ being the critical wavevector of total external reflection, and Nb_0 and Nb_1 being the SLD of material above and below the interface respectively. From here on, p denotes the projection of $\vec{k}$ on the z axis and the index z is omitted, therefore $p_{z,i} = p_i$ (incoming) and $p_{z,f} = p_f$ (outgoing).
By assuming that the surface of the interface is ideally flat, then the incoming wave function of neutrons can be described as a product:

$$\Psi(\vec{r}) = \psi(z)\exp\left(i\vec{k}_{\parallel}\vec{r}_{\parallel}\right) , \tag{2.14}$$

with the transverse component $\psi(z)$ being described by the ordinary differential equation of the second order:

$$\left[\frac{d^2}{dz^2} - p_c^2(z) + p_0^2\right]\psi(z) = 0\,. \tag{2.15}$$

If the $p_c^2(z)$ term is independent of the $z-$ coordinate, then the solution of the equation is straightforward, following from $p^2 = p_0^2 - p_c^2$, and is equal to $\psi(z) = \exp(ipz)$. In such case, a general solution can be represented as a superposition of reflected and transmitted waves with amplitudes r and t and wavenumbers $\pm p = \sqrt{p_0^2 - p_c^2}$:

$$\psi(z) = te^{ipz} + re^{-ipz}\,. \tag{2.16}$$

Assuming that in a small coherence volume close to the surface, both the incident and reflected waves coexist, then the wave function above the surface ($z \leq 0$) is equal to:

$$\psi(z) = \psi_0(z) = e^{ip_0 z} + r_0 e^{-ip_0 z}\,, \tag{2.17}$$

and below the surface ($z \geq 0$):

$$\psi(z) = \psi_1(z) = t_1 e^{ip_1 z}\,. \tag{2.18}$$

Solving the equation at the condition $z = 0$, one obtains from $\psi_0(0) = \psi_1(0)$ and from its derivatives $\psi_0'(0) = \psi_1'(0)$ the Fresnel reflection coefficient $r_{0,1}^F$ and the Fresnel transmission coefficient $t_{0,1}^F$:

$$r_{0,1}^F = \frac{p_0 - p_1}{p_0 + p_1} \quad ; \quad t_{0,1}^F = \frac{2p_0}{p_0 + p_1}\,. \tag{2.19}$$

Since $p_1 = \sqrt{p_0^2 - p_c^2}$, then for purely real potential and $p_0 > p_c$, r will be proportional to $r \sim p_0^{-2}$ and t will approach $t \to 1$. It is noted also that at $p_0 = p_c$, the value of transmission coefficient t will be equal to $t = 2$, which means that the probability density is enhanced (while keeping the neutron flux constant) by a factor of $|\psi_0(0)|^2 = 4$. In the vicinity of the surface, there is a constructive interference of incoming and reflected waves, as they are exactly in phase at $z = 0$.

2.1.3 Parratt's recursive algorithm

So far only reflection from a single interface has been assessed, but in order to describe realistic systems, one has to extend this to a multilayer with ideally flat interfaces. One of the possibilities is to use the so-called Parratt's recursive algorithm [3]. It is one of the two widespread choices for calculation of reflectivity from a multilayer, the other one being the Abeles transfer matrix method. Several implementations of the algorithm exist and can be found in [4, 53, 54]. A multilayer can typically be represented as a system of N slabs between two semi-infinite media, the medium above the sample ($j = 0$, $z < 0$) and the substrate ($j = N + 1$, $z > z_N$) and is shown in figure 2.4a. Each $j-$ th layer

has the following properties, namely thickness $d_j = z_j - z_{j-1}$, and SLD Nb_j. If we denote the first layer as $j = 1$, then the medium lying above ($z < 0$) and the substrate ($z > z_N$) have no thickness property, but do have the SLD Nb_0 and Nb_{N+1}. This means that for N layers, there are N thicknesses and $N + 2$ SLDs. This nomenclature is used throughout the following text where all the sums run from 1 to N and the substrate and initial medium are taken care of with proper indices.

Fresnel reflection coefficient defined in eq. 2.19 for a single interface has the general form:

$$r^F_{j,j+1} = \frac{p_j - p_{j+1}}{p_j + p_{j+1}}\,, \tag{2.20}$$

where, as before, $p_j = \sqrt{p_0^2 - 4\pi N b_j}$ and $p_0 = \frac{2\pi}{\lambda}\sin\theta_i$. The recurrent equation for the ratio of reflected and transmitted amplitudes inside the $j-$ th layer $X_j = r_j/t_j$ can now be defined as:

$$X_j = \frac{r^F_{j,j+1} + X_{j+1}}{1 + r^F_{j,j+1} X_{j+1}} e^{2i\phi_j}\,, \tag{2.21}$$

with $\phi_j = d_j p_j$ being the phase shift of the waves travelling through $j-$ th layer. The system can be solved by assuming that there is no reflection from the substrate $r_{N+1} = 0 \implies X_{N+1} = 0$, immediately yielding:

$$X_N = r^F_{N,N+1} e^{2i\phi_N}\,. \tag{2.22}$$

The final result of this recursion is the ratio X_0. By definition $t_0 = 1$, therefore X_0 is nothing else than reflectance or specular reflectivity of the multilayer:

$$R = |X_0|^2 = \left|\frac{r_0}{t_0}\right|^2 = |r_0|^2\,. \tag{2.23}$$

In order to more correctly describe reflectivity from real multilayers one also needs to include the roughness at the interfaces. This can be, to a good approximation, taken care of by modifying the Fresnel reflection coefficient (eq. 2.19) with the so-called Nevot-Croce factor $r^{F*}_j = r^F_j \exp\left(-2p_j p_{j+1}\sigma_j^2\right)$, where σ_j is the respective width of the interface [6]. In this case the σ represents the width of a Gaussian and is related to the full width half maximum as FWHM $= 2.355\sigma$.

2.1.4 Neutron field in a multilayer

Many systems can be represented as a series of stratified layers with a 1D potential profile. In the case of thin films deposited one after another it is straightforward to design such a model. However, the concept of stratification could also be used in the systems which themselves do not consist of distinctive layers, but rather resemble a layered structure when a 1D projection of their profile is taken, for example a lipid

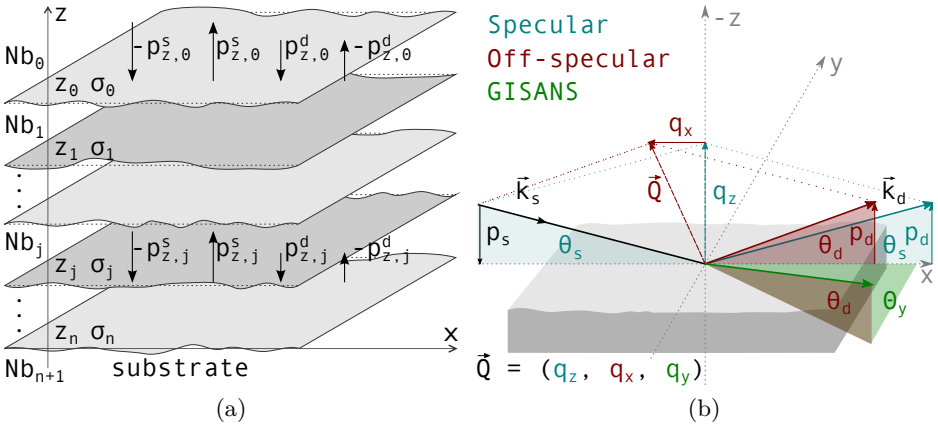

(a) (b)

Figure 2.4: (a) Schematic of a multilayer. (b) Schematic of the grazing incidence geometry.

bilayer where the two layers are the lipid head and the lipid tail. Regardless of the physics, any such profile can be approximated with the use of Riemann sum:

$$V(z) = \sum_{j=1}^{N} V_j(z)\,, \tag{2.24}$$

where $V_j(z)$ is constant for $z_{j-1} \leq z < z_j$. $V_0 = 0$, located in $z \leq 0 \implies z = 0$, representing the vacuum and $V_N = V_s$ in $z > z_N$, representing the semi-infinite substrate. Returning back to equation 2.16 with such potential, the following result is obtained:

$$\psi(z) = \sum_{j=1}^{N} \left(t_j e^{ip_j(z-z_{j-1})} + r_j e^{-ip_j(z-z_{j-1})} \right) \Longleftarrow z > 0\,. \tag{2.25}$$

Parratt's recursive algorithm yields the total reflectivity of the system. In order to calculate the amplitudes of both upward and downward moving waves, the transmission t_j and reflection r_j amplitudes in each layer, the neutron amplitude continuity requirement at each interface has to be taken into account. This yields the following system of two equations:

$$e^{i\phi_j} t_j + e^{-i\phi_j} r_j = t_{j+1} + r_{j+1}\,, \tag{2.26}$$

$$p_j \left(e^{i\phi_j} t_j - e^{-i\phi_j} r_j \right) = p_{j+1} \left(t_{j+1} - r_{j+1} \right)\,. \tag{2.27}$$

One can express the amplitudes r_j and t_j from eqs. 2.25 as:

$$r_j = e^{i\phi_j} \frac{\left(r^F_{j,j+1} + X_{j+1}\right) t_{j+1}}{t^F_{j,j+1}}\,, \tag{2.28}$$

$$t_j = e^{-i\phi_j} \frac{\left(1 + r^F_{j,j+1} X_{j+1}\right) t_{j+1}}{t^F_{j,j+1}}\,. \tag{2.29}$$

Dividing the two equations, a generalized expression for the ratio $X_j = r_j/t_j$, which links the ratio in layer $j+1$ with that in j, is obtained. Its calculation was already described by eq. 2.21 and it can now also be used to first explicitly calculate t_j with the help of equations 2.29 and 2.19. Assuming $t_0 = 1$ and $\phi_0 = 0$ results in the following expression for t_1:

$$t_1 = \frac{t^F_{0,1}}{1 + r_{0,1} X_1}\,. \tag{2.30}$$

After obtaining all the transmission amplitudes (downward moving waves), one can then simply calculate the amplitude of reflected (upward) moving waves as:

$$X_j = \frac{r_j}{t_j} \implies r_j = X_j t_j\,. \tag{2.31}$$

2.1.5 Robust calculation of neutron field

During the calculation, as many Fresnel transmission and reflection coefficients as there are interfaces have to be computed. In turn, this means that the refracted wave vector has to be calculated for each layer with scattering length density Nb_j, as shown in eq. 2.13. From this equation it follows that if the critical momentum transfer p_c in the layer is larger than the initial momentum transfer p_0, then $p_c^2 > p_0^2 \implies p_0^2 - p_c^2 < 0$ and $\sqrt{p_0^2 - p_c^2}$ will have a purely imaginary solution. In practical terms this means that below the critical angle, the distorted wave vector as defined by eq. 2.13 for a purely real SLD will be imaginary [42]. In case of exponents $e^{-i\phi}$ being present in the calculation, this would mean that they become very large or even diverge. This happens when a layer of high SLD is buried above a layer of lower SLD. Compared to most other algorithms presented in the literature (including the original one by Parratt), the one described above is significantly improved in this regard, as it does not contain such exponents. This is especially relevant in the case of soft matter, where it is common to have a combination of deuterated films with high SLD and protonated with low SLD, and makes the calculation of both amplitudes numerically robust.

The final step is to calculate the total neutron field inside a layer by the use of eq. 2.25. Due to the presence of the phase term $e^{-ip_j(z-z_{j-1})}$, the same problem of diverging exponents could arise. To solve this, an auxiliary amplitude $\widetilde{r}_j$ can be introduced, such that $r_j = e^{i\phi_j}\widetilde{r}_j$. Equation 2.31 then becomes:

$$\widetilde{r}_j = \widetilde{X}_j t_j \,, \tag{2.32}$$

with $\widetilde{X}_j$ being

$$\widetilde{X}_j = \frac{r^F_{j,j+1} + X_{j+1}}{1 + r^F_{j,j+1} X_{j+1}} e^{i\phi_j} \,. \tag{2.33}$$

Using these results, we can then rewrite eq. 2.25 as:

$$\psi(z) = \sum_{j=1}^{N} \left(t_j e^{ip_j(z-z_{j-1})} + \widetilde{r}_j e^{i(\phi_j - p_j(z-z_{j-1}))} \right) \iff z > 0 \,, \tag{2.34}$$

$$\psi(z) = \sum_{j=1}^{N} \left(t_j e^{ip_j(z-z_{j-1})} + \widetilde{r}_j \right) \,. \tag{2.35}$$

2.2 Off-specular reflectometry

By relaxing the condition that the incoming angle from the source θ_i and outgoing angle θ_f have to be the same ($\theta_i \neq \theta_f$), one also records out of specular reflection. This means that the lateral wavevector component $q_{x,y}$ will be non-zero. In the grazing incidence geometry in general, the momentum transfer is a vector with 3 components:

$$\begin{aligned} \vec{Q} = (q_z,\, q_x,\, q_y) &= \left(\vec{k}_f - \vec{k}_i,\, \vec{k}_f^{\,\parallel} - \vec{k}_i^{\,\parallel} \right) = \\ &= \frac{2\pi}{\lambda} \left(\sin\theta_f + \sin\theta_i,\, \cos\theta_f \cos\Theta_y - \cos\theta_i,\, \sin\Theta_y \cos\theta_f \right) \,, \end{aligned} \tag{2.36}$$

however, the azimuthal angle in off-specular experiments is kept at $\Theta_y = 0$, therefore $\cos\Theta_y = 1$ and $\sin\Theta_y = 0$:

$$\vec{Q} = \frac{2\pi}{\lambda} \left(\sin\theta_f + \sin\theta_i,\, \cos\theta_f - \cos\theta_i,\, 0 \right) \,. \tag{2.37}$$

Keeping in mind that $q_x \ll q_z$, they probe very different real space dimensions. This is also connected to the coherence length, which in the lateral direction is on the order of $l_{\text{coh}} \sim 50\,\mu\text{m}$, and is thus much bigger than in the perpendicular direction ($l_{\text{coh}} < 1\,\mu\text{m}$) [55].

Depending on the instrument, the off-specular spectrum can be recorded either in single wavelength measurement or in time-of-flight (ToF), where the angle is kept constant and a band of wavelengths is used. This, together with the fact that we are in grazing incidence geometry, brings forward a very interesting problem, namely the representation of the reciprocal space. As the measurements are done in the close vicinity to the critical angle, the reciprocal space is quite distorted due to different scattering (reflection and

refraction) events. This is the region ($q_z < 3q_c$) where the Born approximation, which considers only single scattering events and plane waves throughout the sample, clearly breaks down by diverging, as shown in figure 2.5.

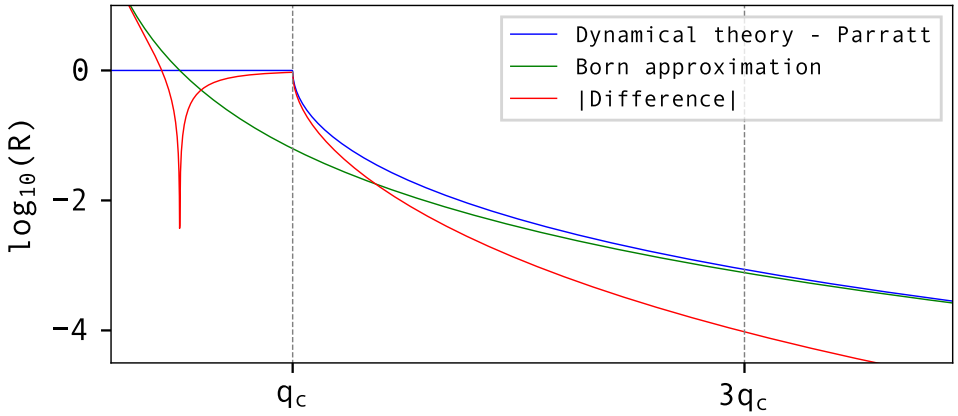

Figure 2.5: Comparison between the dynamical theory, calculated with Parratt's algorithm, and the Born approximation. Around $\sim 3q_c$, the difference becomes very small.

In a single wavelength measurement, different scans, which are the most relevant for off-specular measurements, can be performed: θ_f scan, during which the incident angle θ_i is kept fixed and both q_z and q_x are varied, and ω rocking scan, where both θ_i and θ_f are varied, so that the q_z is kept constant and the q_x is being changed. The detector scan, being the most basic measurement, unfortunately does not keep q_z constant, as both q_x and q_z are changed during the measurement. Being close to the critical angle, this means cutting through features with irregular spacing. The ω scan is done at constant q_z and only the q_x is varied, which more clearly shows the reciprocal space spacing of the lateral features out of specular peak (which only depend on the q_x). This necessarily means that both measurements have a different *natural* reciprocal space representation, as e.g. representing the detector scan data as $(q_x, R(q_z, q_x))$ would necessarily also show features dependent purely on q_z. This arises due to the fact that the transformations between the reciprocal space representations are non-trivial, being a function of 3 variables, the projections of the two wave vectors p_i and p_f and the lateral wave vector transfer q_x.

On the other hand, during the ToF measurement, the incoming angle $\theta_i = \theta_0$ is kept constant and the wave vector transfer p_i is varied by a velocity selection, which selects a narrow band of wavelengths, since neutrons of different wavelengths travel at different velocities. The reflected neutrons are then detected by a 3-dimensional detector with 2 spatial and one temporal dimension, based on their time of flight from the chopper to the detector. The *natural* space would therefore be $(\theta_i + \theta_f, \lambda)$. The features in both mentioned spaces appear very different. There are even more representations which all show different features. A longer, albeit still incomplete discussion on the topic can be found in [43].

In brief, the 3 variables determining the reciprocal space are themselves also functions of

θ_i, θ_f and λ. From this it follows that the only independent and unique representation is $(\theta_i, \theta_f, \lambda)$ space. The data is usually measured as a function of only 2 variables, e.g. (θ_i, θ_f) at fixed λ or (θ_f, λ) at fixed θ_i in ToF mode. This means that neither provide complete information. Furthermore, the transformation of data from $I(\theta_i^{\text{fixed}}, \theta_f, \lambda)$ to $I(\theta_i^{\text{fixed}}, p_i, p_f)$ is not symmetric to the exchange of p_i and p_f and q_x. This means that the data recorded on the same sample, represented in (q_z, q_x) space, will appear different for different wavelength. This is not a problem in our data analysis workflow, since all the scattering parameters are calculated from the 3 independent variables and the algorithm presented in the rest of this thesis outputs the intensity as $I(\theta_i, \theta_f, \lambda)$.

As a general rule, one should be aware of the reciprocal space representation issue and choose the one which best shows the features of the sample. If the features are coming from the morphology of the interface, they are a function of q_x and vice versa, if the predominant features come from the interference of waves inside of the sample and optical phenomena, they are a function of p_i and p_f.

Off-specular scattering arises from correlated lateral inhomogeneities located at one or more interfaces inside the sample. They will either appear as discrete peaks or diffuse intensity, depending on their shape and size. The signal coming from real interfaces, especially in soft matter is often of the diffuse type. Long-range correlations are not a consequence of a periodic structure, but rather of statistical origin, meaning that a given correlation length exists, but without explicit meaning of the shape of correlations in real space. As more and more reflectometers become equipped with 2-dimensional detectors, the off-specular signal is readily measured alongside specular measurements. The measurement time which is spent on specular measurement is not sufficient for good statistics in the off-specular area. However, in case of any noticeable signal, a dedicated off-specular measurement can be performed. As will be shown later, off-specular 2D information constrain the specular fits to a very high degree, acting almost as an additional contrast.

Only a very brief overview of the relevant literature is given at this point. Most of the analysis of off-specular scattering is performed in the frame of the distorted wave Born approximation. The first paper dealing with DWBA applied to off-specular scattering is the one by Sinha et al. [11], and is still regarded as an introduction into the DWBA for reflectivity. After developing the formalism for a single interface, Holy et al. have expanded it to a multilayer [13, 56]. In addition to using the height-height correlation function for a self-affined surface, Holy et al. introduced a vertical out-of-plane correlation which describes the roughness replication in the perpendicular direction by exponential decay. It was very shortly after that the use of such correlation was published by Schlomka et al. [45]. Furthermore, they tried to describe off-specular scattering also by an exact dynamical theory [57], but it turned out that up to this day it is too complicated and never came into general use. There have been several important contributions to the algorithm, mainly by further expanding the differential scattering cross section into an intensity calculation by integration over the solid angle. One of the first and rigorous papers dealing with that is the one by Daillant et al. [12, 58], where an explicit equation for the absolute intensity for single wavelength measurements is given.

Several reviews exist on the topic which also add various valuable information. The one from Tolan [59] contains a large selection of different soft matter systems and explanations of the correlation functions with good comparisons to the experiments. Another very good review, covering most of the topics in off-specular reflectivity and DWBA, is the one from Pynn et al. [39]. A large book which describes scattering of X-rays from various systems was published by Daillant [52], but the notation is not very suitable for neutron scattering, as the potential is mostly developed in terms of a refractive index instead of SLD. Finally, a very good review with examples was published recently by Lauter et al. [42], which rigorously presents the contributions and contains a very good robust calculation of wave field inside the sample.

2.2.1 Differential scattering cross-section in distorted wave Born approximation

Among different approaches to solve off-specular scattering, the distorted wave Born approximation (DWBA) has emerged as one of the most robust techniques. It is a perturbation method where the actual rough surface is represented as a small perturbation to the ideal potential calculated from Fresnel theory. The scattering potential $V(\vec{r})$ is split into the ideal potential $\bar{V}(\vec{r}) = \bar{V}(z)$ and the small perturbation due to the lateral deviations of SLD $\delta V(\vec{r})$ [11]:

$$V(\vec{r}) = \bar{V}(\vec{r}) + \delta V(\vec{r}) = \bar{V}(z) + \delta V(x, z)\,. \tag{2.38}$$

With interface at position $z = 0$ and the potential $\bar{V}(z)$ being equal to:

$$\bar{V}(z) = \frac{2\pi\hbar^2}{m} \begin{cases} Nb \;;\; z > 0\,, \\ 0 \;;\; z < 0\,, \end{cases} \tag{2.39}$$

Examining the second (perturbation) term, the potential is more complicated this time, as it is both $z-$ and $(x, y)-$ dependent and formally defined as:

$$\delta V(x, z) = \frac{2\pi\hbar^2}{m} \begin{cases} Nb \text{ for } z(x, y) < z < 0 \text{ if } \Delta z(x, y) < 0\,, \\ -Nb \text{ for } z(x, y) > z > 0 \text{ if } \Delta z(x, y) > 0\,, \\ 0 \text{ otherwise}\,. \end{cases} \tag{2.40}$$

This represents the interface as a sum of the SLD contrast between two layers, $Nb_j - Nb_{j-1}$, and a series of small $(x, y)-$ in-plane dependent deviations $z(x) \ll d_j$, where $d_j = z_j - z_{j-1}$ is the thickness of a layer. These deviations represent the roughness of the interface.

Extending and rewriting this further into the notation introduced before, the total scattering cross-section consists of two contributions:

$$\frac{\mathrm{d}\sigma}{\mathrm{d}\Omega} = \left(\frac{\mathrm{d}\sigma}{\mathrm{d}\Omega}\right)_{\mathrm{spec}} + \left(\frac{\mathrm{d}\sigma}{\mathrm{d}\Omega}\right)_{\mathrm{off-spec}} = \tag{2.41}$$

$$= S_{\mathrm{spec}}(\theta_i)|R(q_z)|^2\delta(\theta_f - \theta_i)\delta(\Theta_y) + \left(\frac{\mathrm{d}\sigma}{\mathrm{d}\Omega}\right)_{\mathrm{off-spec}}, \tag{2.42}$$

with $S_{\mathrm{spec}}(\theta_i)$ being the geometrical factor dependent on the incoming angle θ_i, $R(q_z)$ the Fresnel reflectivity of the system obtained with e.g. Parratt's algorithm, and δ being the Dirac delta function ensuring the specular condition, $\theta_f = \theta_i$. The second term is:

$$\left(\frac{\mathrm{d}\sigma}{\mathrm{d}\Omega}\right)_{\mathrm{off-spec}} = \left|f(\vec{q}_\parallel; p_f, p_i)\right|^2 , \tag{2.43}$$

where the amplitude $f(\vec{q}_\parallel; p_f, p_i)$ is defined as

$$f(\vec{q}_\parallel; p_f, p_i) = \langle\Psi_f|\delta V(\vec{r})|\Psi_i\rangle = \tag{2.44}$$

$$= -\int \mathrm{d}\vec{r}\Psi_f(\vec{r})\Delta Nb(\vec{r})\Psi_i(\vec{r})\,. \tag{2.45}$$

The SLD deviations are now represented as $\Delta Nb(\vec{r}) = Nb(\vec{r}) - \bar{N}b(z)$. These represent the deviations due to roughness from the laterally averaged SLD in the $z-$ direction. One has to note that the SLD is not averaged over the whole area of the beam but rather the coherence volume. The coherence length for a typical neutron experiment is much smaller ($\sim 50\,\mu\mathrm{m}$) than the beam size ($\sim 2\,\mathrm{cm}$), but still much larger than the in-plane features ($\sim 1\,\mu\mathrm{m}$), let alone the thickness of the layers ($\sim 1000\,\text{Å}$).

As stated before, the wavefunctions Ψ_i and Ψ_f are a superposition of the laterally and perpendicularly dependent parts:

$$\Psi_i(\vec{r}) = e^{i\vec{k}^i_\parallel\vec{r}_\parallel}\Psi_i(z) = e^{i\vec{k}^i_\parallel\vec{r}_\parallel}\left(t^i_j e^{ip^i_j(z_j - z_{j-1})} + r^i_j e^{-ip^i_j(z_j - z_{j-1})}\right), \tag{2.46}$$

$$\Psi_f(\vec{r}) = e^{i\vec{k}^f_\parallel\vec{r}_\parallel}\psi_f(z) = e^{i\vec{k}^f_\parallel\vec{r}_\parallel}\left(t^f_j e^{ip^f_j(z_j - z_{j-1})} + r^f_j e^{-ip^f_j(z_j - z_{j-1})}\right). \tag{2.47}$$

Taking into account that the SLD in perpendicular direction of a slice between z_j and z_{j-1} is homogeneous, this clearly shows that the amplitude defined in equation 2.45 only depends on the lateral component of the wavevector transfer $\vec{q}_\parallel = \vec{k}^f_\parallel - \vec{k}^i_\parallel$. The perpendicular components $\psi_{i,f}(z)$ on the other hand depend only on the $z-$ direction and, as before, eq. 2.16, describes the transmitted and reflected neutrons moving in downward or upward direction.

Analogously to the eq. 2.13, the corresponding distorted wavevectors in the $j-$th layer are defined as:

$$p_j^i = \sqrt{p_0^{2;i} - p_c^2} = \sqrt{p_0^{2;i} - 4\pi(Nb_j - Nb_0)}\,, \tag{2.48}$$

$$p_j^f = \sqrt{p_0^{2;f} - p_c^2} = \sqrt{p_0^{2;f} - 4\pi(Nb_j - Nb_0)}\,. \tag{2.49}$$

As before, due to refraction while propagating through the sample, the wavevectors have to be modified. As can be seen, they are in general complex quantities. For $p_c^2 > p_0^2$, i.e. below the critical edge of the total reflection, they will become purely imaginary. This is something to keep in mind as it can cause numerical issues discussed at relevant positions in the text.

For the simplest case of a single interface between two semi-infinite media, the transmission amplitudes $t_{0,1}^i = t_{0,1}^{F,i}$ and $t_{0,1}^f = t_{0,1}^{F,f}$ are the only remaining contribution. They are given by the Fresnel equations shown in the eq. 2.19. Careful examination of the terms shows that, correctly, the amplitude goes to zero for $p_0 = 0$ and approaches 1 as $p_0 \gg p_c$. Furthermore, the maximum is at $p_0^2 = p_c^2$ where $t_{0,1}^{i,f} = 2$. The consequence of this is a very interesting effect, known as Yoneda wings or peaks, which occur in the vicinity of the critical angle when:

$$p_0^2 = p_c^2\,. \tag{2.50}$$

It is a purely optical effect, arising from the enhancement of the neutron field. Furthermore, since Born approximation does not take the perturbed wavefield into the account, it cannot replicate this important feature in the recorded off-specular spectrum.

By inserting the wavefunctions and assuming that $d_j = z_j - z_{j-1}$, equation 2.45 can be rewritten as:

$$f(\vec{q}_\parallel; p_f, p_i) = \\ -\sum_{j=1}^{N} \int_{z_{j-1}}^{z_j} \mathrm{d}z \left(t_j^f e^{ip_j^f d_j} + r_j^f e^{-ip_j^f d_j}\right) \Delta N b_j(\vec{q}_\parallel, z) \left(t_j^i e^{ip_j^i d_j} + r_j^i e^{-ip_j^i d_j}\right)\,. \tag{2.51}$$

This can be further simplified by carefully inserting the assumptions presented above. First let us start by taking into account that in a given slice j, the mean potential is constant and the z coordinate can be rewritten as $\bar{z}_j = (z_j - z_{j-1})/2$.:

$$\Delta N b_j(\vec{q}_\parallel, z) \approx \Delta N b_j(\vec{q}_\parallel, \bar{z}_j) = \Delta N b_j(\vec{q}_\parallel)\,, \tag{2.52}$$

The amplitude then becomes:

$$f(\vec{q}_\parallel; p_f, p_i) = \\ -\sum_{j=1}^{N} \Delta\overline{Nb}_j(\vec{q}_\parallel) \int_{z_{j-1}}^{z_j} \mathrm{d}z \left(t_j^f e^{ip_j^f z} + r_j^f e^{-ip_j^f z}\right) \left(t_j^i e^{ip_j^i z} + r_j^i e^{-ip_j^i z}\right)\,. \tag{2.53}$$

After the integration, we finally arrive to the following equation, which can easily be implemented in a computer algorithm:

$$f(\vec{q}_\parallel; p_f, p_i) = \\ -\sum_{j=1}^{N} d_j \Delta\overline{Nb}_j(\vec{q}_\parallel) \left(t_j^f t_j^i F_j^{t,t} + t_j^f r_j^i F_j^{t,r} + r_j^f t_j^i F_j^{r,t} + r_j^f r_j^i F_j^{r,r} \right) , \quad (2.54)$$

with F being the following Laue functions, representing the analytical integrals over z:

$$F_j^{t,t} = \frac{e^{i(\phi_j^f + \phi_j^i)} - 1}{i(\phi_j^f + \phi_j^i)}, F_j^{t,r} = \frac{e^{i(\phi_j^f - \phi_j^i)} - 1}{i(\phi_j^f - \phi_j^i)}, \\ F_j^{r,t} = \frac{e^{i(-\phi_j^f + \phi_j^i)} - 1}{i(-\phi_j^f + \phi_j^i)}, F_j^{r,r} = \frac{e^{-i(\phi_j^f + \phi_j^i)} - 1}{-i(\phi_j^f + \phi_j^i)} .$$

As already defined in section 2.1.5, one can now use the auxiliary amplitudes in order to get rid of the three Laue functions that contain the aforementioned undesirable factors $e^{-i\phi^{i,f}}$. If the phases are purely complex, which can occur below the critical edge, these factors can diverge and cause numerical instability. Using the auxiliary reflection amplitude from eq. 2.32, the equation 2.54 is then rewritten as:

$$f(\vec{q}_\parallel; p_f, p_i) = \\ -\sum_{j=1}^{N} d_j \Delta\overline{Nb}_j(\vec{q}_\parallel) \left[\left(t_j^f t_j^i + \widetilde{r}_j^f \widetilde{r}_j^i \right) F_j^{t,t} + \left(t_j^f \widetilde{r}_j^i + \widetilde{r}_j^f t_j^i \right) \widetilde{F_j} \right] , \quad (2.55)$$

$$F_j^{t,t} = \frac{e^{i(\phi_j^f + \phi_j^i)} - 1}{i(\phi_j^f + \phi_j^i)}, \widetilde{F_j} = \frac{e^{i\phi_j^f} - e^{i\phi_j^i}}{i(\phi_j^f - \phi_j^i)} . \quad (2.56)$$

With this, the central DWBA mechanism has been described. In fact, the contributions which are the most important in the experimental spectra presented in this work, are actually the ones coming from the wavefield modulation inside the layers. The following sections will focus on the term $\Delta N b_j(\vec{q}_\parallel)$, which contains the actual information about the morphology of the interface.

2.2.2 Scattering from interfacial roughness

In this section, the DWBA cross-section is further developed for a common case where the off-specular scattering is coming from the roughness at the interface between two media.

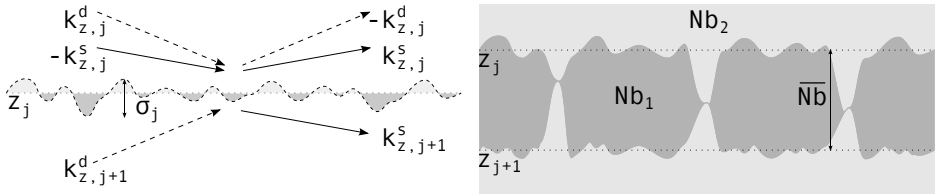

(a) (b)

Figure 2.6: (a) Schematic of the $j-$th interface in the DWBA. (b) Schematic of the mixed phase layer with $\overline{Nb}$ and the two phases Nb_1 and Nb_2 which comprise it.

The tiny SLD deviations $\Delta Nb(x, y, z)$ (as shown in fig. 2.6a), where the true interfacial position $z_j(x, y)$ is fluctuating around the mean coordinate, $\bar{z}_j(z)$ can be defined as a 2D dependent SLD:

$$Nb_j(x, y) = \begin{cases} Nb_{j-1}(z) \text{ for } \delta z_j(x, y) < 0\,,\ z_j(x, y) < \bar{z}_j(z)\,, \\ Nb_j(z) \text{ for } \delta z_j(x, y) > 0\,,\ z_j(x, y) > \bar{z}_j(z)\,. \end{cases} \tag{2.57}$$

This ensures that the interfacial region is not treated differently than the "bulk" of the layers below or above and it can be seen in terms of deviations: it is then defined as $\min(\delta z(x, y)) < z < \max(\delta z(x, y))$. The deviations are therefore positive and negative, describing the shape of the interface along the whole coherence volume with a certain cutoff height/depth. By examining the distribution of depths for a real case in terms of coordinates (x, y), it can be shown that for real interfaces, the deviations $\delta z(x, y)$ are often Gaussian distributed. For such an interfacial profile, the width can easily be described with a single parameter σ_j and the projection of such interface on the $z-$ axis is an error function. This correctly corresponds to the definition of "roughness" described by the Nevot-Croce factors in section 2.1.3.

Doing so, one has to strictly obey the rule that the deviations averaged over the whole coherence volume must be zero: $\langle \delta z_j(x, y; \bar{z}_j \pm \delta z(x, y)) \rangle = 0 \implies \langle \Delta Nb_j(x, y; \bar{z}_j \pm \delta z(x, y)) \rangle = 0$ and their squares $\langle \Delta Nb_j(x, y; \bar{z}_j \pm \delta z(x, y))^2 \rangle \geq 0$.

In such cases, the solutions of the wavefunctions $\psi_j^{i,f}$ below and $\psi_{j-1}^{i,f}$ above the interface, are considered to be valid across the whole layer j, including the interfacial regions $\widetilde{z} = \bar{z}_j \pm \delta z(x, y)$. This means that for the regions below and above the smooth interface, the wavefield is considered to be constant. It corresponds to the respective solution of the 1D wave equation for SLD $Nb(\widetilde{z})$. The approximation is only valid and works well in the region where $p_j^f \sigma_j \ll 1$ and $p_j^i \sigma_j \ll 1$ [13].

Making a graded interfacial profile which consists of more layers is therefore a common and powerful technique which allows for investigation of almost arbitrary SLD profiles. In other terms, as it will be seen in experimental chapters, focusing on the change of the ideal potential, keeping the perturbation fairly simple, yields very good results.

With all this in mind, revisiting the equation 2.45 for scattering from SLD deviations $\Delta Nb_j(x, y; \delta z_j(x, y))$, one obtains the following relation:

$$f(\vec{q}_\parallel; p_f, p_i) = -\int_{\widetilde{z}} \mathrm{d}\widetilde{z}\, \psi_j^f \Delta Nb(q_x, q_y; \widetilde{z}) \psi_j^i(\widetilde{z})\,, \tag{2.58}$$

where the deviations in reciprocal space are the 2D Fourier transform of the deviations in real space:

$$\Delta Nb_j(q_x, q_y; \widetilde{z}) = \int_{S(\delta z)} \mathrm{d}x\, \mathrm{d}y\, e^{i(q_x x + q_y y)} \Delta Nb_j(x, y; \widetilde{z})\,. \tag{2.59}$$

For low roughness ($p_j^{i,f}\sigma_j \ll 1$), we can further simplify the equations:

$$\psi_j^{i,f}(\widetilde{z}) \approx t_j^{i,f} + r_j^{i,f} = t_{j-1}^{i,f} e^{i\phi_{j-1}^{i,f}} + r_{j-1}^{i,f} e^{-i\phi_{j-1}^{i,f}}\,, \tag{2.60}$$

with $\phi_{j-1}^{i,f} = p_{j-1}^{i,f} d_{j-1} = p_{j-1}^{i,f}(z_j - z_{j-1})$ being the phase shift upon waves travelling through $j-$th layer. This results in the simplified expression for the amplitude:

$$f(\vec{q}_\parallel; p_f, p_i) = \\ -(t_j^i + r_j^i)(t_j^f + r_j^f)(\Delta Nb_j - \Delta Nb_{j-1}) \iint_{S_0} \mathrm{d}x\, \mathrm{d}y\, e^{i(q_x x + q_y y)} \delta z_j(x, y)\,. \tag{2.61}$$

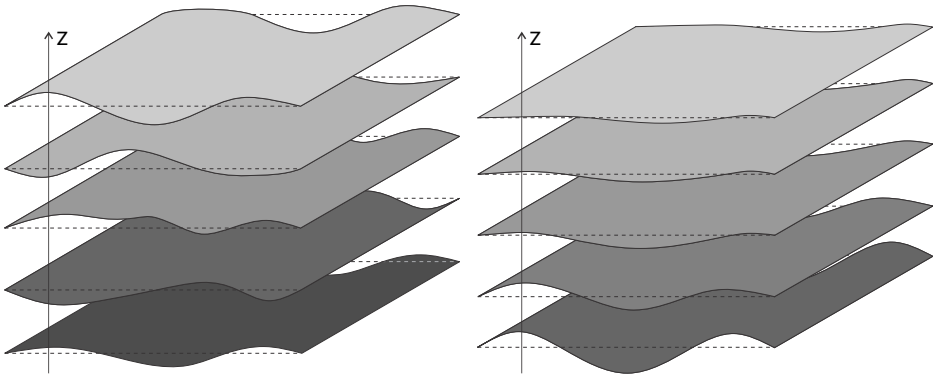

(a) (b)

Figure 2.7: Difference between (a) no vertical correlation and (b) with correlation.

2.2.3 Low roughness case and self-affine interface

It was assumed that the deviations from the true interface are distributed according to the Gaussian distribution, meaning that the projection of the density profile on $z-$ axis is an error function. If the height deviations are correlated on some length scale, they can be described by a height-height correlation function $\mathcal{C}$. It turns out that one of the most widespread is the correlation function of a self-affine surface:

$$\mathcal{C}(\rho) = \sigma^2 \exp\left[-\left(\frac{\rho}{\xi_\rho}\right)^{2h}\right], \tag{2.62}$$

with $\rho = \sqrt{(x-x')^2 + (y-y')^2}$, ξ_ρ being the cutoff correlation length and h being the Hurst parameter [13]. If $h = 0.5$, then $\mathcal{C}$ describes an exponential decay. Furthermore, h is connected to the Hausdorff fractal dimension as $D = 3 - h$. Since $D = 2.5$ corresponds to a regular 2D Brownian surface, it can be seen that selecting $h = 0.5$ is a reasonable choice [60]. Furthermore, the Fourier transform of eq. 2.62 with $h = 0.5$ also has an analytical solution, which speeds up calculations considerably. Due to these reasons, the value of h is kept at $h = 0.5$ throughout the work.

In off-specular neutron reflectivity, the beam slits are kept open in the azimuthal direction, so the data is averaged over the y azimuthal coordinate, more precisely over the azimuthal angle Θ_y, as:

$$\overline{\left(\frac{\mathrm{d}\sigma}{\mathrm{d}\Omega}\right)}^{y}_{\text{off}} = \int \mathrm{d}\Theta_y \left(\frac{\mathrm{d}\sigma}{\mathrm{d}\Omega}\right)_{\text{off}} = \frac{\lambda}{2\pi}\int \mathrm{d}q_y \left(\frac{\mathrm{d}\sigma}{\mathrm{d}\Omega}\right)_{\text{off}}. \tag{2.63}$$

The differential scattering cross-section $\left(\frac{\mathrm{d}\sigma}{\mathrm{d}\Omega}\right)_{\text{off}}$ was introduced in eq.2.43 and the amplitude in eq. 2.59. Substituting these two equations into eq. 2.63 finally yields the averaged differential cross-section in y:

$$\overline{\left(\frac{\mathrm{d}\sigma}{\mathrm{d}\Omega}\right)}^{y}_{\text{off}} = S_{\text{off}}(\theta_i)\lambda \sum_{j,k=1}^{N+1} G_{j,k}(q_x; p_f, p_i), \tag{2.64}$$

where S_{off} can be found in eq. 3.16 and $G_{j,k}(q_x; p_f, p_i)$ contains both the linear combinations of the transmission and reflection amplitudes, as well as the correlator $G_{j,k}(x; p_f, p_i)$:

$$G_{j,k}(q_x; p_f, p_i) = \int \mathrm{d}x\, e^{iq_x x} G_{j,k}(x; p_f, p_i), \tag{2.65}$$

$$G_{j,k}(x; p_f, p_i) = (t_j^i + r_j^i)(t_k^i + r_k^i)^*(t_j^f + r_j^f)(t_k^f + r_k^f)^* \\ (Nb_j - Nb_{j-1})(Nb_k - Nb_{k-1})^* \mathcal{C}_{j,k}^{\delta z}(x), \tag{2.66}$$

$$\mathcal{C}_{j,k}^{\delta z}(x', y') = \frac{1}{S_{\text{off}}}\int \mathrm{d}x'\mathrm{d}y' \delta z_j(x', y')\delta z_k(x', y'). \tag{2.67}$$

The correlation function at $x = 0$ must be equal to $\mathcal{C}_{j,j}(0) = \sigma_j^2$ or its mean squared roughness. If the indices j and k are not equal, then there might not be any correlation and $\mathcal{C}_{j,k} = 0$. In fact, a better way to treat out-of-plane correlations between interfaces (shown in figure 2.7) is to assume an exponential decay in roughness, obtaining [45, 56]:

$$\mathcal{G}_{j,k}(z) = \sigma_j \sigma_k \exp\left(-\frac{|z_j - z_k|}{\xi_z}\right). \tag{2.68}$$

Out of this equation it can also be seen that the higher the correlation length ξ_z, the more correlated the interfaces will be, as $\frac{|z_j - z_k|}{\xi_z} \to 0 \implies \exp^0 \to 1$. On the other hand, if $z_j = z_k$, then the term will be zero and $\mathcal{C}_{j,j}(0) = \sigma_j^2$. Furthermore, if both σ_j and σ_k are positive, then the interfaces oscillate in-phase and, vice-versa, if one is positive and another negative, they oscillate in anti-phase.
Assuming that the lateral correlations also decay exponentially, we can use equation 2.62:

$$\mathcal{C}_{j,k}(x) = \mathcal{C}_{j,k}(0) \exp\left(-\frac{|x|}{\xi_x}\right) . \tag{2.69}$$

The correlation function in reciprocal space is the 1D Fourier transform of $C_{j,k}(q_x)$:

$$C_{j,k}(q_x) = \int \mathrm{d}x \, e^{iq_x x} \mathcal{C}_{j,k}(x) . \tag{2.70}$$

The benefit of using this correlation function (with $h = 0.5$) is that it has an analytical solution (Gradsteyn & Ryzhik, 3.893.2 (p. 477).), so the result can be further simplified as:

$$C_{j,k}(q_x) = 2\sigma_j\sigma_k \frac{\xi_x}{1 + (q_x\xi_x)^2} e^{-\frac{|z_j - z_k|}{\xi_z}} . \tag{2.71}$$

This, unsurprisingly, results in a Lorentzian function in reciprocal space.
All the equations can now be combined into an explicit expression for off-specular scattering cross-section, averaged over y:

$$\overline{\left(\frac{\mathrm{d}\sigma}{\mathrm{d}\Omega}\right)}^{y}_{\mathrm{off}} = S_{\mathrm{off}}(\theta_i) \sum_{j,k=1}^{N+1} \Delta N b_j \Delta N b_k^* \\ (t_j^i + r_j^i)(t_j^f + r_j^f)(t_k^i + r_k^i)^*(t_k^f + r_k^f)^* \frac{2\lambda\sigma_j\sigma_k\xi_x}{1 + (q_x\xi_x)^2} e^{-\frac{|z_j - z_k|}{\xi_z}} , \tag{2.72}$$

or with all the bilinear combinations of the neutron wave field from equation 2.55 expanded:

$$\overline{\left(\frac{\mathrm{d}\sigma}{\mathrm{d}\Omega}\right)}^{y}_{\mathrm{off}} = \\ S_{\mathrm{off}}(\theta_i) \sum_{j=1}^{N+1} \sum_{k=1}^{N+1} \Delta N b_j \Delta N b_k^* \left[\left(t_j^f t_j^i + r_j^f r_j^i\right) F_j^{t,t} + \left(t_j^f r_j^i + r_j^f t_j^i\right) \widetilde{F_j}\right] \\ \left[\left(t_k^f t_k^i + r_k^f r_k^i\right) F_k^{t,t} + \left(t_k^f r_k^i + r_k^f t_k^i\right) \widetilde{F_k}\right]^* 2\lambda\sigma_j\sigma_k \frac{\xi_x}{1 + (q_x\xi_x)^2} e^{-\frac{|z_j - z_k|}{\xi_z}} . \tag{2.73}$$

Analyzing the expression, one can quickly see that contributions of individual layers are rather small, but the overall cross-section grows quadratically with the number of layers

due to the sum. It also increases with the same rate for increasing interfacial roughness σ and increasing SLD contrast ΔNb.

As the integral

$$\int \mathrm{d}q_x \, \frac{2\xi}{1+(q_x\xi_x)^2} = 2\pi \tag{2.74}$$

is normalized and therefore independent of ξ_x, it can be seen that by increasing ξ_x, intensity is increased and width is decreased. That results in decreased intensity of Yoneda peaks. Because of this, counterintuitively, a system with longer correlation length will have off-specular intensity distributed in very close vicinity to the specular peak and, vice versa, for a system with shorter correlation length, the intensity will be spread over larger q_x.

In fact, in the limit $\xi_x \to \infty$ and $\theta_i > 0$:

$$\frac{2\xi_x}{1+(q_x\xi_x)^2} \to 2\pi\delta(q_x) = \frac{\lambda}{\sin\theta_i}\left(\delta(\theta_i-\theta_f)+\delta(\theta_i+\theta_f)\right) . \tag{2.75}$$

In the DWBA, the off-specular differential cross-section therefore merges with the specular reflectivity, which can readily be seen by omitting the transmission and reflection amplitudes in the equation 2.73.

2.2.4 Scattering from deviations through the layer

If the correlated deviations are not only located at an interface, but throughout the layer, e.g. holes, then the aforementioned approach can be used as well. There are, however, a few slight modifications that have to be considered. First, the deviations in the case of the interfacial roughness were defined as $\Delta Nb_j = Nb_j - Nb_{j-1}$. In the case of deviations throughout the layer, we first have to define a mean SLD potential $\overline{Nb}_j$ in the (x, y) plane.

The first case is a simple system of two regularly spaced ($l_1 = l_2$, if l is the size of the phase) phases with $Nb_{j,1}$ and $Nb_{j,2}$ respectively. Assuming that the size of the phases is much lower than the lateral coherence length, $l_1, l_2 \ll l_{\mathrm{coh}}$, the mean SLD seen by specular reflectometry will be equal to:

$$\overline{Nb}_j = \frac{Nb_{j,1}+Nb_{j,2}}{2} , \tag{2.76}$$

meaning the mean of the two phases. Their respective contrasts seen in off-specular direction will then be:

$$\Delta Nb_{j,1} = Nb_{j,1} - \overline{Nb}_j \;\; ; \;\; \Delta Nb_{j,2} = Nb_{j,2} - \overline{Nb}_j . \tag{2.77}$$

There will therefore be two contributions coming from such a layer, one from each of the phases: each contrast will be quite small, as they represent only the difference to the mean SLD. It is imperative that in such formulation, the condition $\overline{\Delta Nb}_j = 0$ must be respected, meaning that if $\Delta Nb_j \neq 0$, then one of the terms is negative and

another is positive. This is not a problem, as the cross-section depends on $\overline{\Delta Nb^2}_j$ and is $\overline{\Delta Nb^2}_j \geq 0$.

This is nothing else than a special case ($c = 0.5$) of the more general form taking into account the volume fraction c of a given phase with Nb_1 inside a layer j with SLD Nb_2, e.g. nanoparticles embedded in a layer or irregularly spaced holes in a layer. Then the mean SLD can be calculated as:

$$\overline{Nb}_j = (1-c)Nb_1 + cNb_2\,. \tag{2.78}$$

The differential scattering cross section for $j-$th layer will then consist of two form factors and a (negative) cross term:

$$\begin{aligned}
\overline{\left(\frac{\mathrm{d}\sigma}{\mathrm{d}\Omega}\right)}^{y}_{\mathrm{off},j} &= S_{\mathrm{off}}(\theta_i) \sum_{\mu,\nu,\eta,\zeta} \left|\Delta\overline{Nb}\right|^2 \underbrace{a^{i,f}_{\mu,\nu}\left(a^{i,f}_{\eta,\zeta}\right)^* C(q_x;\xi)}_{G(q^{i,f};q_x,\xi)} = \\
&= S_{\mathrm{off}}(\theta_i) \sum_{\mu,\nu,\eta,\zeta} \Big[(1-c)\left|\Delta Nb_1\right|^2 G\left(q^{i,f};q_x,\xi_1\right) + c\left|\Delta Nb_2\right|^2 G\left(q^{i,f};q_x,\xi_2\right) \\
&+ c(1-c)\Delta Nb_1 \Delta Nb_2 G\left(q^{i,f};q_x,\xi_{12}\right)\Big]\,,
\end{aligned} \tag{2.79}$$

where $\Delta Nb_1 = \overline{Nb} - Nb_1$, $\Delta Nb_2 = \overline{Nb} - Nb_2$ and $C(q_x;\xi)$:

$$C\left(q_x;\xi\right) = d^2 \frac{\xi_x}{1+(q_x\xi_x)^2}\,, \tag{2.80}$$

with d being the thickness of the layer, because $C(0) \sim d^2|\Delta Nb|^2$. If one of the contrasts or concentrations is small, then the term can be neglected for brevity, as very small terms have almost no contribution to the final recorded spectrum.

3 Full reflectometry

In this chapter, specular reflectivity and off-specular scattering are united into an intensity spectrum. Even though each of them has different resolution and different conditions, the scaling of off-specular scattering to specular reflectivity is not arbitrary. One has to keep in mind that it is not universal, but instrument dependent, and therefore has to be reformulated for single wavelength measurements. Even though a lot of papers dealing with off-specular scattering exist, such a rigorous treatment which would allow for calculation of off-specular intensity in absolute units is lacking.
Firstly, specular reflectivity is revisited and properly smeared over the divergences in incoming and outgoing angles, then the same is done for off-specular scattering, where at least the resolution and the geometrical factors are different. Finally, an explicit formula is given for calculation of specular and off-specular intensity, which allows not only the analysis, but also for prediction of intensity for a hypothesized experiment.

3.1 Scaling of specular to off-specular differential cross-section

As already stated, the total differential cross-section is the sum of the two differential cross-sections of specular reflectivity and off-specular scattering:

$$\left(\frac{\mathrm{d}\sigma}{\mathrm{d}\Omega}\right) = \left(\frac{\mathrm{d}\sigma}{\mathrm{d}\Omega}\right)_{\mathrm{spec}} + \left(\frac{\mathrm{d}\sigma}{\mathrm{d}\Omega}\right)_{\mathrm{off-spec}} . \tag{3.1}$$

The first term is equal to:

$$\left(\frac{\mathrm{d}\sigma}{\mathrm{d}\Omega}\right)_{\mathrm{spec}} = S_{\mathrm{spec}}(\theta_i)|R(q_z)|^2\delta(\theta_f - \theta_i)\delta(\Theta_y) , \tag{3.2}$$

with $S_{\mathrm{spec}}(\theta_i)$ being the area of the incident beam on the sample surface at the angle θ_i, $R(q_z)$ being the reflection amplitude, and the delta functions taking care of the specular conditions. The differential scattering cross-section at this step diverges at $\theta_i = \theta_f$ and $\Theta_y = 0$, as by definition it describes scattering from an infinitely large sample into an infinitesimally small angle. By introducing a finite area of the beam, the number becomes finite, but still diverges for the infinitely small angle. Only after integration over the solid angle will the total scattering cross-section become finite:

$$\sigma_{\mathrm{spec}}^{\mathrm{total}} = \phi_{\mathrm{spec}}(\theta_i)|R(q_z)|^2 . \tag{3.3}$$

It can immediately be seen that at the total reflection ($|R(q_z)|^2 = 1$), the total cross-section is then just equal to the area of the beam illuminating the sample, therefore all the incoming intensity gets reflected.

The area pre-factor depends on the ratio between the sample area S_0 and the beam size S_b on the sample. The latter is a function of the incoming angle and can be larger than the former below the over-illumination angle, when only a part of the beam interacts with the sample. This angle is defined as: $S_0 \sin\theta_i \leq S_b$. If the surface is fully illuminated at the illumination angle θ_{ill}, the two areas are equal: $S_0 = S_b \implies S_{\text{spec}}(\theta_i) = S_b$. The pre-factor $\phi_{\text{spec}}(\theta_i) = S_{\text{spec}}(\theta_i)/S_b$ is equal to:

$$\phi_{\text{spec}}(\theta_i) = \begin{cases} \frac{\sin\theta_i}{\sin\theta_{\text{ill}}} & ; \ \theta_i \leq \theta_{\text{ill}}\,, \\ 1 & ; \ \theta_i > \theta_{\text{ill}}\,. \end{cases} \tag{3.4}$$

In time-of-flight (ToF) experiments, the angle is usually selected such that this pre-factor is 1.

In order to account for the divergence in the angle, one has to convolve eq. 3.2 with the divergence of the incident beam, wavelength spread and the detector angle divergence. Even though these contributions might be coupled, it is usually possible to independently integrate over each one of them, (provided that their corresponding functions are normalized), combining them in a common resolution function W:

$$W = W_{\theta_i} W_{\theta_f} W_{\Theta_y} W_{\lambda}\,. \tag{3.5}$$

Furthermore, we can assume that each of the functions describes a Gaussian distribution over the respective quantity:

$$W_{\theta_i} = \frac{1}{\sqrt{2\pi}\Delta_{\theta_i}} \exp\left(-\frac{(\theta_i - \theta_i')^2}{2\Delta_{\theta_i}^2}\right), \tag{3.6}$$

$$W_{\theta_f} = \frac{1}{\sqrt{2\pi}\Delta_{\theta_f}} \exp\left(-\frac{(\theta_f - \theta_f')^2}{2\Delta_{\theta_f}^2}\right), \tag{3.7}$$

$$W_{\Theta_y} = \frac{1}{\sqrt{2\pi}\Delta_{\Theta_y}} \exp\left(-\frac{\Theta_y^2}{2\Delta_{\Theta_y}^2}\right), \tag{3.8}$$

$$W_{\lambda} = \frac{1}{\sqrt{2\pi}\Delta_{\lambda}} \exp\left(-\frac{(\lambda - \lambda')^2}{2\Delta_{\lambda}^2}\right). \tag{3.9}$$

It has to be considered that in the case of neutron reflectometry, the width of $\Delta_{\Theta_y} \gg \Delta_{\theta_i} \sim \Delta_{\theta_f}$. Because of this, the smearing over the Θ_y angle can be neglected and simply the expression for the y averaged differential cross-section (eq. 2.64) can be used.

Performing the convolution of the differential scattering cross-section with the resolution function W:

$$\overline{\left(\frac{\mathrm{d}\sigma}{\mathrm{d}\Omega}\right)}_{\mathrm{spec}} = \int \mathrm{d}\theta_i' W(\theta_i - \theta_i', \theta_f - \theta_i') S_{\mathrm{spec}}(\theta_i') \overline{|R(q_z')|^2}^{\lambda}, \tag{3.10}$$

removes the δ functions from before and causes the cross-section to become finite. The term $\overline{|R(q_z')|^2}^{\lambda}$ is equal to:

$$\overline{|R(q_z')|^2}^{\lambda} = \int \mathrm{d}\lambda' W_{\lambda}(\lambda - \lambda') |R(q_z')|^2, \tag{3.11}$$

with $q_z' = \frac{4\pi}{\lambda'} \sin\theta_i'$. In the case of Gaussian smearing, the δ functions go away and what is left is of Gaussian shape with the effective width $\Delta = \sqrt{\Delta_{\theta_i}^2 + \Delta_{\theta_f}^2}$ being equal to the geometrical mean of the individual widths of the angle divergence:

$$I_{\mathrm{spec}}(\theta_f, \theta_i; \lambda) = \frac{e^{-\frac{(\theta_f - \theta_i)^2}{2\Delta^2}}}{\sqrt{2\pi}\Delta} \overline{|R(q_z)|}^2, \tag{3.12}$$

with

$$\overline{|R(q_z)|}^2 = \int \mathrm{d}\theta' \phi_{\mathrm{spec}}(\theta_i) \frac{e^{-\frac{(\theta - \theta')^2}{2\widetilde{\Delta}^2}}}{\sqrt{2\pi}\widetilde{\Delta}} \overline{|R(q_z')|^2}^{\lambda}. \tag{3.13}$$

The final expression is smeared with another Gaussian with the expectation value $\theta = (\theta_i + \theta_f)/2$ and the effective width of $\widetilde{\Delta}$.
The smearing over the incident and outgoing angles can be decomposed into two distinct components: longitudinal and transverse. They smear the specular intensity, calculated via the Parratt formalism. The first one, combined with wavelength smearing, over the wavevector projection q_z onto the normal to the surface, and the second one smearing the specular reflection in the surface plane. It can be seen that this substitutes the δ functions with the Gaussian function of small width $\Delta = \sqrt{\Delta_{\theta_i}^2 + \Delta_{\theta_f}^2}$. Despite the large maximum value of the differential cross-section smeared over the wavelength resolution, the integrated intensity never exceeds 1 because of the integral over $\theta_i + \theta_f$. At this step, the result of the differential scattering cross-section of specular reflection can be directly compared to the off-specular counterpart. Both smearing steps correctly scale the specular reflectivity with respect to the differential scattering cross-section as shown in equation 3.1.

3.2 Absolute intensity of reflectivity

In order to obtain the absolute intensity from the calculation, the off-specular differential scattering cross-section has to be assessed in a similar manner to the specular one from the previous section. They are then finally combined into a common spectrum, just as during the measurement. This is a necessary step especially in neutron reflectometry. As the intensity of the spectrum and its characteristic features are rather weak and due

to different contributions heavily intertwined with one another, it is virtually impossible to correctly assess the model without calculation in absolute intensity. There are a few differences while smearing one or another, but conceptually the steps are very similar.

Firstly, one has to keep in mind that since $\theta_i \neq \theta_f$, there is no δ function accounting for the specular reflection. The off-specular spectrum will therefore not have a Gaussian shape, but will still be smeared with the integrals along the angles and wavelength in both directions. Secondly, it may appear that resolution is not at all important, as the scattered intensity is distributed over much broader angular range. However, the source of off-specular scattering are the deviations which are smaller in size than the lateral coherence length and therefore intricately connected to the resolution. It is therefore crucial to have good resolution, as only then the off-specular contributions will be discriminated from the specular intensity. Because of this, the angular width is a function of the resolution and potential imperfections at distances larger than the coherence length, such as waviness or bending of the sample. These effects are also readily seen in the specular reflection asymmetrical line shape [61].

There exist a few more cases worth mentioning, as they are one of the common types of phenomena measured by off-specular scattering. Namely, the Bragg diffraction coming from periodic lateral patterns such as gratings or magnetic patterns in thin layers, where the dimension is very large, but still smaller than the coherence length [15, 16, 62]. Commonly observed spectra, which are heavily influenced by optical effects coming from interesting multilayer SLD structure, are also entirely resolution dependent. Even the most striking feature in the spectrum, the Yoneda peaks, are ideally sharp peaks, but are smeared due to the divergences.

Starting with the same assumptions as for the specular part, the off-specular differential scattering cross-section is equal to:

$$\overline{\left(\frac{\mathrm{d}\sigma}{\mathrm{d}\Omega}\right)}_{\mathrm{off}} = \int \mathrm{d}\theta_i' \mathrm{d}\theta_f' W(\theta_i - \theta_i', \theta_f - \theta_f') \overline{\left(\frac{\mathrm{d}\sigma}{\mathrm{d}\Omega}\right)}^{\lambda,y}_{\mathrm{off}}, \tag{3.14}$$

$$\overline{\left(\frac{\mathrm{d}\sigma}{\mathrm{d}\Omega}\right)}^{\lambda,y}_{\mathrm{off}} = \int \mathrm{d}\lambda' W_\lambda(\lambda - \lambda') \overline{\left(\frac{\mathrm{d}\sigma}{\mathrm{d}\Omega}\right)}^{y}_{\mathrm{off}}, \tag{3.15}$$

with $\overline{\left(\frac{\mathrm{d}\sigma}{\mathrm{d}\Omega}\right)}^{y}_{\mathrm{off}}$ being equal to eq. 2.64. Here the geometrical factor $S_{\mathrm{off}}(\theta_i)$ is equal to the area of the beam-illuminated sample:

$$S_{\mathrm{off}}(\theta_i) = \begin{cases} \frac{S_b}{\sin\theta_{\mathrm{ill}}} \; ; & \theta_i \leq \theta_{\mathrm{ill}}\,, \\ \frac{S_b}{\sin\theta_i} \; ; & \theta_i > \theta_{\mathrm{ill}}\,. \end{cases} \tag{3.16}$$

This can now be combined into a cross-section with both the wavelength resolution and smearing over the incident and outgoing angles:

$$\left(\frac{\mathrm{d}\sigma}{\mathrm{d}\Omega}\right)_{\mathrm{off-spec}} = \int \mathrm{d}\theta_i' W_{\theta_i}(\theta_i - \theta_i') S_{\mathrm{off}}(\theta_i) \int \mathrm{d}\theta_f' W_{\theta_f}(\theta_f - \theta_f') \int \mathrm{d}\lambda' W_\lambda(\lambda - \lambda') G(0, p_i', p_f') \frac{2\lambda'\xi}{1 + (q_x'\xi)^2} \,. \quad (3.17)$$

With this step, the two differential scattering cross-sections are now unified. In order to compare the intensities $I_{\mathrm{spec}}(\theta_f, \theta_i; \lambda)$ from eq. 3.12 and $I_{\mathrm{off}}(\theta_f, \theta_i; \lambda)$, the geometrical factor has to be normalized with the cross-section of the incident beam S_b. This also finally eliminates the size of the beam as a scaling parameter. After this step, the two can be compared as $I = I_{\mathrm{spec}} + I_{\mathrm{off}}$:

$$I_{\mathrm{off}}(\theta_f, \theta_i; \lambda) = \int \mathrm{d}\theta_i' \phi_{\mathrm{off}}(\theta_i') \int \mathrm{d}\theta_f' W_{\theta_i}(\theta_i - \theta_i') \int \mathrm{d}\lambda' W_\lambda(\lambda - \lambda') G(0, p_i, p_f) \frac{2\lambda'\xi}{1 + (q_x\xi)^2} \,, \quad (3.18)$$

with $\phi_{\mathrm{off}}(\theta_i)$ being beam size independent:

$$\phi_{\mathrm{off}}(\theta_i) = \begin{cases} \frac{1}{\sin\theta_{\mathrm{ill}}} \;; & \theta_i \leq \theta_{\mathrm{ill}} \,, \\ \frac{1}{\sin\theta_i} \;; & \theta_i > \theta_{\mathrm{ill}} \,. \end{cases} \quad (3.19)$$

Combining equations 3.12 and 3.18, we finally come to the equation for full reflectivity in absolute intensity for ToF mode ($\theta_i = \mathrm{const} \wedge \theta_i > \theta_{\mathrm{ill}}$) under the above-mentioned assumptions:

$$I_{\mathrm{full}}(\theta_f, \theta_i; \lambda) = I_{\mathrm{spec}}(\theta_f, \theta_i; \lambda) + I_{\mathrm{off}}(\theta_f, \theta_i; \lambda) = \underbrace{\int \mathrm{d}\theta' \frac{e^{-\frac{(\theta-\theta')^2}{2\widetilde{\Delta}^2}}}{\sqrt{2\pi}\widetilde{\Delta}}}_{\text{Angular resolution}} \underbrace{\int \mathrm{d}\lambda' \frac{e^{-\frac{(\lambda-\lambda')^2}{2\Delta_\lambda^2}}}{\sqrt{2\pi}\Delta_\lambda}}_{\text{Wavelength resolution}} \left[\underbrace{\frac{e^{-\frac{(\theta_f-\theta_i)^2}{2\Delta^2}}}{\sqrt{2\pi}\Delta} |R(q_z')|^2}_{\text{Specular part}} + \underbrace{\frac{1}{\sin\theta_i} G(0, p_i, p_f) C(q_x, \xi)}_{\text{Off-specular part}} \right] , \quad (3.20)$$

where $\widetilde{\Delta}$ is the effective angular divergence, Δ_λ the wavelength divergence and Δ the width of the specular peak. It is mostly assumed that $\widetilde{\Delta} = \Delta$. $G(0, p_i, p_f)C(q_x, \xi)$ is equal to:

$$G(0,p_i,p_f)C(q_x,\xi) = \sum_{j=1}^{N+1}\sum_{k=1}^{N+1} \Delta N b_j \Delta N b_k^* \left[\left(t_j^d t_j^s + r_j^d r_j^s\right) F_j^{t,t} + \left(t_j^d r_j^s + r_j^d t_j^s\right) \widetilde{F_j}\right] \left[\left(t_k^d t_k^s + r_k^d r_k^s\right) F_k^{t,t} + \left(t_k^d r_k^s + r_k^d t_k^s\right) \widetilde{F_k}\right]^* \sigma_j \sigma_k \, C(q_x,\xi)^{j,k}\,, \quad (3.21)$$

with $C(q_x,\xi)^{j,k}$ being equal to:

$$C(q_x,\xi)^{j,k} = \frac{2\lambda'\xi_{j,k}}{1+(q_x\xi_{j,k})^2} e^{-\frac{|z_j - z_k|}{\xi_z}}\,. \quad (3.22)$$

The algorithm presented here does not force the use of the specific correlation function used here. As long as the assumptions presented are the same, any correlation function can be used. One must keep in mind that analytically solvable functions are preferred, as numerical integration is very computationally expensive.

The biggest difference between the specular and off-specular part becomes apparent by comparing the specular and off-specular terms in eq. 3.20. Where the off-specular part is simply smeared over the angle and wavelength, the specular part has a very sharp peak around $\theta_i = \theta_f$ due to the specular reflection. For practical reasons, it is numerically better to divide the off-specular part from eq. 3.20 by the maximum of the normalized Gaussian shape of the specular peak, in order to keep the numbers obtained by the Parratt's algorithm, as they are already of correct magnitude. It is also obvious that the resolution does not play nearly as big role in the off-specular part as in the specular. It has an influence, but it only smears the already low intensity into a larger area. An assumption is also made that the off-specular intensity must be much smaller than that of specular, as the two are simply added together. If one wants to avoid that, the full treatment of the scattering should be taken into account, i.e. scattering into 4π angle. However, in the examples presented in this work, this is mostly not necessary, as $I_{\text{off-spec}} < 1\% I_{\text{spec}}$.

The consequence of the coexistence of the two spectra is that the fitting procedure is much more constrained as with the specular part only. As it was already discussed, the off-specular part carries information on the amplitudes inside the layers, which in turn are connected to their mean potential, itself being the result of specular reflectivity. It turns out that specular reflectivity has to be refined to a very high level. Usually the goodness of fit is assessed by minimizing the squared distance from the experimental points (x_i, y_i) to the model $(x_i, Y(x_i))$ with a χ^2 function [63]:

$$\chi^2 = \frac{1}{N-M}\sum_i^N \left(\frac{(y_i - Y(x_i; a_1 \cdots a_M))^2}{\sigma_i}\right)\,, \quad (3.23)$$

where N is the number of experimental points, M is the number of parameters, and σ_i is the Gaussian error of each measurement. For sufficient off-specular results, the specular reflectivity must be refined at least to around $\chi^2 < 2.5$. Even though χ^2 cannot

be taken as the only measure of the fit, the correlation matrix also being important, its results cannot be neglected. In all the results which have been fitted in this thesis, χ^2 was calculated according to eq. 3.23.

3.3 Estimation of off-specular intensity

In the previous few sections, a generalized approach has been described, which combines many existing ideas and solutions of off-specular scattering into one unified algorithm that allows for calculation of spectra in absolute intensity in the same straightforward way as solving specular intensity.
It is surely conceptually different and more time consuming, as the number of computational steps to calculate $R(n)$ scales as $R(n) \sim \mathcal{O}(n^2)$, opposed to the Parratt's formalism which scales as $R(n) \sim \mathcal{O}(n)$, where n is the number of layers in a multilayer. It is however not any harder in a practical way, as there are only a few additional parameters representing the morphology of a buried layer. As will be shown later, even using such a simple model as presented above, the experimental data from a variety of soft matter systems agrees very well with the calculations.
In order to better illustrate the quantitative power of the whole formalism, a semi-dimensionless analysis for a few cases is discussed here. If the width of the resolution function $\Delta_q \approx \frac{\pi}{\lambda}$ is very small and $q_x\xi << 1$, meaning that the coherence length $l^x_{\text{coh}} \gg \xi$, then the off-specular signal will be well resolved from the specular peak. In such regime, the resolution plays no role and the intensity is described by:

$$I_{\text{off}} \approx G(0, p_i, p_f)\frac{2\lambda\xi}{1 + (q_x\xi)^2}\,. \tag{3.24}$$

The Lorentzian term has a maximum at $q_x = 0$ and is equal to $2\lambda\xi$. The term then decays with q_x^{-2}, as $q_x \geq \xi^{-1}$. Plugging in the expression for q_x in angle and wavelength, one obtains the equivalent expression $|\theta_i - \theta_f| \geq \lambda(\pi\theta_i\xi)^{-1}$, from which it follows that the off-specular signal is well resolved if $\xi \leq \lambda(\pi\theta_i\Delta)$. Otherwise, one can observe the characteristic broadening of the specular peak, where the off-specular signal merges into the specular reflection. The characteristic Yoneda peaks are coming from the first term in the above equation, as they are an optical phenomenon and appear as enhancements at momentum transfers equal to the critical momentum transfers inside the multilayer $p_i, p_f = p_{j,c}$.
Furthermore, we always have to keep in mind the source of the SLD deviations, whether they are located at an interface or throughout a layer. This will determine the magnitude of the scattering as:

$$G(0, p_i, p_f) \approx \begin{cases} d_j^2|Nb_j(x) - \overline{Nb}_j|^2\,; & \text{for layer of thickness } d_j = z_j - z_{j-1}\,, \\ \sigma_j^2|Nb_j - Nb_{j-1}|^2\,; & \text{for roughness } \sigma_j\,. \end{cases} \tag{3.25}$$

For the case of deviations throughout the layer, the intensity will scale as $I_{\text{off}} \sim \lambda\xi d^2|\Delta Nb|^2$. Let us assume that $\lambda = 10\,\text{Å}$, $\xi = 1 \times 10^4\,\text{Å}$, $d = 20\,\text{Å}$ and $|\Delta Nb| = 1 \times 10^{-10}\,\text{Å}^{-4}$. In

such case, the value of $I_{\text{off}} \sim 0.004$ is very small, especially compared to the specular reflectivity, but it grows with the square of the thickness.

It can be seen from such an example that, unless the deviations are coming from a sufficiently thick layer or have very high contrast, their contribution to the spectrum will be weak. Even at Yoneda peaks, assuming the maximal enhancement of ~ 100, the scattering will still be quite weak. It is therefore crucial that each contribution gets evaluated carefully and separately.

4 Effect of preannealing on a polymer-polymer interface

4.1 Irreversible adsorption of macromolecules

It has been shown that the physical properties of thin films depend mainly on the interfacial behavior [64]. This is important in numerous applications of thin films, such as in microelectronic industry and other ever smaller functional devices (solar cells, light-emitting diodes (LEDs), etc.). In case of organic photovoltaics, the micro-morphology of the active layer is one of the key aspects in increasing efficiency [65]. Despite the well-known fact that macromolecules exhibit different properties when geometrically confined [66], the behavior of macromolecules at a nonrepulsive interface is not well characterized. One such phenomenon is the irreversibly adsorbed (physisorption) layer at the substrate, which grows as a function of time upon thermal annealing [34], [37]. The exact architecture of such a layer is not well established, as it is not trivial to non-destructively investigate a buried polymer interface.

The polymer chain will form irreversibly adsorbed layers on top of a surface even when the interactions with the monomer units are on the order of k_BT. The chain will stay attached due to the participation of many monomers in the process, a collective detachment of all the adsorbed monomer units is necessary [67]. The growth time of the adsorbed layer has been studied and follows a master curve if normalized for different parameters, such as degree of polymerization (i.e. molecular weight) or annealing temperature [35]. Furthermore, pre-annealing (thermal annealing) the bottom layer for a long time allows the macromolecules to equilibrate. Depositing another layer on top, the interface between the two polymers may be affected by the preannealing of the first layer, since the configuration of the chains may be related to the process.

One of the challenges related to the study of adsorbed material is the relatively hard accessibility of a buried polymer interface. Due to their non-destructive nature and the ability to selectively deuterate different molecular species, neutrons are a suitable probe for buried polymer-polymer and/or polymer-solid interfaces. With the use of specular and off-specular neutron reflectivity, we are able to access two length scales at the same time, the profile perpendicular to the sample surface, yielding the thickness of the films with $\sim$ Å accuracy and the change of the density profile at the interface, and the structure parallel to the sample surface, yielding in-plane correlation lengths in

the range $\sim 300\,\mathrm{nm}$ to $\sim 10\,\mu\mathrm{m}$. According to self-consistent field theory, the interfacial width between two immiscible polymers is composed of two terms [68]:

$$\Delta^2 = \Delta_0^2 + \langle \Delta\zeta^2 \rangle \,, \tag{4.1}$$

where Δ_0^2 is the intrinsic interfacial width and $\langle \Delta\zeta^2 \rangle$ is the width caused by the capillary wave spectrum. The two contributions could be studied with neutron reflectivity and OSS. The amplitude of the capillary waves is related to the interfacial tension and the long cutoff length in thin polymer films is influenced by the long range van der Waals force [68]. As the volume density change of an adsorbed layer would be only marginal to the rest of the layer, it would most probably be within the experimental error of specular reflectivity. Such a layer has recently been reported [38], but we have not found it in our measurements. Evidence for the adsorbed layer could thus be seen as a change of either the amplitude or the cutoff length of the capillary wave spectrum (or both) at an above-lying interface. Since the cutoff would experimentally be seen as a diffuse, broadly distributed intensity, it would be very hard to assess the actual length without a program which links specular and off-specular scattering parts, together with their structural parameters, into one common framework, similarly to the one presented in chapter 3.

Studies of polymer interfaces with both X-rays and neutrons have confirmed the existence of capillary waves either at polymer-air [69], [70] or polymer-polymer interface [68], [71]. However, there are no standard tools for the analysis of neutron off-specular scattering. We have, therefore, a good model system for verification of the previously presented off-specular reflectometry algorithm.

4.2 Preparation of thin polymer films

Firstly, the preparation and pre-characterization of the samples used is described in detail. The sample preparation follows a standard protocol for preparing uniform and homogeneous thin films of various thicknesses on silicon substrates. Prior to any neutron scattering experiments, an estimation of the thickness and homogeneity of the deposited layers has to be made. This is usually done using laboratory ellipsometry equipment, which is a very accurate and fast method for determination of thicknesses and optical properties of thin layers. Unfortunately, due to the used polymers having very similar refractive indices, it is not very suitable for the evaluation of multilayers, except the total thickness. Furthermore, a brief overview of atomic force microscopy (AFM) will be given, as it was sometimes performed to investigate the top surface morphology.

In order to study the effect of thickness on the polymer-polymer interface, a series of samples with varying bottom layer thickness has to be prepared. This way, the distance from the substrate is gradually increased. Furthermore, to observe the effect of the adsorbed layer, screening the potential of the substrate, two structurally identical sample series were prepared. Both are composed of deuterated polystyrene (d-PS) and protonated poly(methyl methacrylate) (h-PMMA) on 2-inch silicon (Si) (100) substrates.

Both of the polymers were obtained from Polymer Source, Inc. and had a weight-averaged molecular weight of $M_w = 252\,\text{kDa}$ for d-PS and $M_w = 342.9\,\text{kDa}$ for h-PMMA respectively. Other properties of the polymers are described in table 4.2.

Firstly, the bottom d-PS layer was spin coated from toluene solutions of different concentrations in order to obtain different thicknesses from 120 Å to 1200 Å. For the first series, which is called *preannealed* in the text, the bottom d-PS layer was first annealed in a vacuum oven for 48 h at $T = 160\,^{\circ}\text{C}$ in order to allow for the irreversible adsorption of molecules onto the Si surface. This is well above the glass transition temperature of both polymers, $T_g = 95\,^{\circ}\text{C}$ for PS [72] and $T_g = 105\,^{\circ}\text{C}$ for PMMA [72].

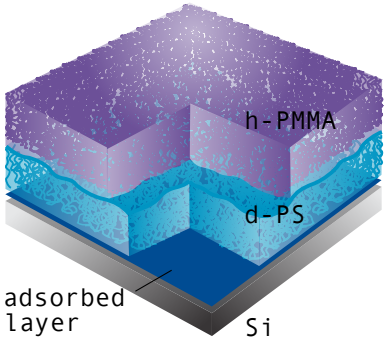

Figure 4.1: Schematic of the bilayer samples.

After the preannealing step, the h-PMMA layer of ∼ 1100 Å thickness was deposited on top, using the floating method. By spin coating the polymer onto a glass slide and then carefully submerging it into milliQ water, the polymer layer will detach and float on the milliQ water surface. It can then be picked up from below with the substrate with previously spin coated d-PS to create a bilayer.

Secondly, for the second series of samples called *non-preannealed* in the text, the top h-PMMA layer was deposited by floating onto the d-PS/Si system without any preannealing steps. The thicknesses of the d-PS layers in both series were carefully matched to correspond to each other by spin coating from the same solution. Finally, both series were annealed in a vacuum oven at $T = 160\,^{\circ}\text{C}$ for further 12 h in order to reach equilibrium at the d-PS/h-PMMA polymer-polymer interface. All the samples with their composition and names are shown in table 4.3 and schematically in figure 4.1.

After each spin coating, as well as the final bilayer, the layers were individually investigated for imperfections by eye and by variable angle Beaglehole Picometer ellipsometer, in order to achieve the correct concentration of the toluene solution for the experiments and to verify whether all the layers were properly deposited.

4.2.1 Chemicals

The two main polymers used are polystyrene (PS) and poly(methyl methacrylate) (PMMA), both in protonated (C_8H_8 and $C_5H_8O_2$) and deuterated (C_8D_8 and $C_5D_8O_2$) forms. They were obtained from Scientific Polymer Products, Inc., USA, Polymer Source, Inc., Canada, or PSS Polymer Standards Service GmbH, Germany. Furthermore, polystyrene sulfonate (PSS), freeze dried from an aqueous solution of poly(4-styrenesulfonic acid), obtained from Sigma Aldrich, Inc., was used in some cases as an underlying sacrificial layer to help with floating (Sec. 4.2.3). The polydispersity index (PDI) describes the distribution of molecular mass in a given polymer sample:

$$\text{PDI} = \frac{M_w}{M_n}\,, \tag{4.2}$$

with M_w being the weight average molecular weight and M_n being the number average molecular weight, with former quantity being more sensitive to molecules of high molecular mass and the latter to the molecules of low molecular mass. In general, the polydispersity index has the dimension PDI ≥ 1, where unity denotes macromolecules of only one length being present in the population. All the polymers of different molecular weights used had a PDI of at least PDI ≤ 1.11. The PDI for each individual compound is stated in the relevant sections that describe individual experiments.

All the solvents used are shown in table 4.1 and all the polymers with their respective molecular weights and PDIs are shown in table 4.2. They were used as received.

Table 4.1: Different solvents used with their properties and manufacturer.

Chemical	Manufacturer, product number, properties
Chloroform	Sigma Aldrich, 32211, p.a./ISO/Ph Eur, $99.0 - 99.4\%$
Acetone	Sigma Aldrich, 32201, p.a./ACS/ISO/Ph Eur, $\geq 99.5\%$
2-propanol	Sigma Aldrich, 33539, p.a./ACS/ISO/Ph Eur, $\geq 99.8\%$
Toluene	Sigma Aldrich, 32249, p.a./ACS/ISO/Ph Eur, $\geq 99.7\%$
Acetic acid	Sigma Aldrich, 33209, p.a./ACS/ISO/Ph. Eur., $\geq 99.8\%$

Table 4.2: List of all the polymers used for the experiments described in the thesis. PS - polystyrene, PMMA - poly(methyl methacrylate), PSS - polystyrene sulfonate, d - deuterated, h - protonated.

Polymer	M_w [kDa]	M_n [kDa]	PDI	Manufacturer
d-PS	66	60	1.1	Polymer Source
d-PS	252	240	1.05	Scientific Polymer Products
h-PMMA	298	292	1.02	Scientific Polymer Products
h-PMMA	343	336	1.02	Scientific Polymer Products
h-PMMA	317	301	1.05	PSS
d-PMMA	230	207	1.11	PSS
PSS	$\sim$75			Sigma Aldrich

Table 4.3: List of samples with their structural properties and annealing times with comments where the samples had to be excluded from the analysis due to holes in the top h-PMMA layer (heterogeneous nucleation) or due to the substrate being bent. Samples with 1 in the name are the non-preannealed series and samples without are the preannealed series.

Name	d_{dPS} [Å] $M_w = 252\,\mathrm{kDa}$	d_{hPMMA} [Å] $M_w = 342.9\,\mathrm{kDa}$	Annealing [h] $[T = 160\,^{\circ}\mathrm{C}]$	Remark
A	892	1221	48 + 12	
B2	1261	1051	48 + 12	
C	640	1063	48 + 12	
D	514	1096	48 + 12	
E	237	1184	48 + 12	
F	131	1101	48 + 12	Holes
A1	849	985	12	
B1	1250	1005	12	Bent
C1	626	1053	12	
D1	527	1106	12	
E1	236	1092	12	Holes
F1	142	1100	12	

4.2.2 Spin Coating

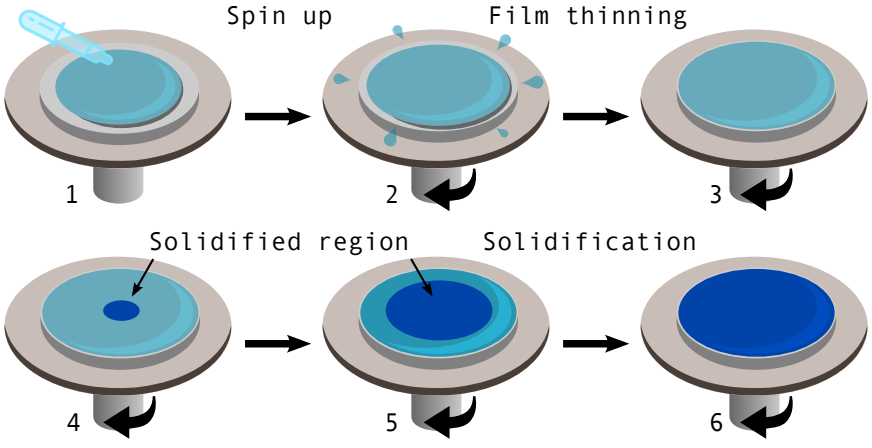

Figure 4.2: Schematic of the spin coating process showing the 6 stages.

Spin coating is one of the standard processes for deposition of soft thin films, the others being dip coating and spray coating, used both in industry as well as in laboratories [73].

It enables relatively fast and reproducible deposition of homogeneous films from a few nm to several µm. Polystyrene (PS) and poly methylmethacrylate (PMMA), like most other polymers, are in a solid, glassy state at room temperature. They can be dissolved in a good solvent, usually chloroform, toluene or some other good and rapidly evaporating organic solvent. The solution is first filtered with a PTFE (teflon) filter of pore size of around 0.5 µm, then deposited on a wafer and spun at a chosen angular velocity ω for enough time that the solvent completely evaporates. First the wafers are cleaned in a four-step process which is designed to eliminate as many different contaminants as possible:

1. ultrasonicate for 15 min in a very mild solution of DECON90 soap and water,
2. ultrasonicate for 15 min in chloroform,
3. ultrasonicate for 15 min in acetone,
4. ultrasonicate for 15 min in isopropanol.

For both polymers, polystyrene (PS) and poly(methyl methacrylate) (PMMA), toluene was used as a solvent. All the solutions were prepared at least 24 h in advance to allow for proper dissolution. All the samples were deposited on 2-inch (100) wafers of 5 mm thickness. The main parameters influencing the final film thickness d are the polymer concentration c_g, the molecular weight of the polymer M, the angular velocity ω, and the solution viscosity η [74]. In order to keep the number of varying parameters as low as possible, the program of the spin coater was always kept the same and only the concentration was changed. At a fixed speed, the thickness d will scale roughly as $d \sim c_g \eta^{1/3}$ [75]. The program used was the following:

1. 2 s at $\omega = 500$ rpm,
2. 55 s at $\omega = 3000$ rpm.

During the process shown in fig. 4.2, the solution will undergo different phases, in which its mechanics are governed by different properties. Initially, an excessive amount of solution is placed on the wafer (1) because of high volatility of the solvent [76]. The initial stage of the process (2) is very short ($t < 4$ s) and the film does not have much time to spread. During this stage, solvent viscosity is the main factor behind the spreading of the solution. After a few seconds, all the solvent will evaporate (3) and solidification will start (4) ($10\,\text{s} > t \geq 4\,\text{s}$). The wafer is then spun until the whole film is solidified and all the remaining solvent evaporates (5, 6) [76], [77].

By changing the concentration of the solution ($\sim 2\,\text{g}\,\text{l}^{-1}$ to $30\,\text{g}\,\text{l}^{-1}$), one can reach a very large range of possible thicknesses (~ 80 Å to 3500 Å), perfectly sufficient for the purpose of the studies described in this work. The films deposited this way are very homogeneous across a large area of the Si wafers. The dome in thickness expected due to a gradient in angular velocity across the wafer only starts to appear at around $d \sim 1000$ Å and even then the relative thickness deviations $\Delta d/d$ are less than $\Delta d/d < 3\%$.

4.2.3 Floating method

As described in the previous section, a single layer on a substrate can easily be prepared with spin coating. If one wants to build a multilayer, however, just spin coating on

top of one another is not suitable, as deposition of another solution from a good solvent would also dissolve the layer below. Briefly, floating is a technique of depositing multiple layers on top of each other with the help of detaching a thin film, floating it on water and then picking it up from below with the already spin-coated wafer, creating a stacked multilayer system.

The glass slides of 5 cm x 5 cm dimension are cleaned according to the same four-step procedure as described before. Then, a solution of a given concentration is spin coated to achieve the desired thickness. After that, the slide with the polymer is slowly submerged into a bath of milliQ water. The idea is that when the water comes in between the slide and the polymer, the layer will float on the water and it can then be picked up by the substrate with previously deposited layers.

However, for thin films and due to some contaminants remaining on the glass or a tiny difference in composition between different glass slides the procedure is quite difficult and sometimes has to be repeated several times. We have also used a different approach. First a sacrificial layer of PSS, which is dissolvable in water, but not in toluene, is deposited. On top of that, we put the desired layer, which is to be stacked on top of our multilayer. Upon spin coating, a bath of milliQ water is prepared with the multilayer already in it. The water level is then carefully raised, causing the PSS layer to very quickly dissolve and release the top layer to start floating on the water surface. At this point, the layer is not manipulated any further to avoid damage or distortion. The water level is then carefully lowered and the substrate meticulously positioned underneath the floating layer, which then lays on top. The sample is then dried for at least an hour in the fume hood. This way, a large amount of layers can be stacked on top of each other. Neutron reflectometry measurements show that multilayers prepared in such a way have a very well-defined structure. On the other hand, there might be consequences on the dewetting. These will be discussed in later chapters.

Spin coating from acetic acid solution

Another way used for spin coating of multilayers is to use orthogonal solvents for different layers, meaning that the polymers are dissolved in different solvents which only solubilize one and not another layer. For PS and PMMA, this could be achieved by using toluene for PS and acetic acid for PMMA. The acetic acid should not dissolve PS. However, our control experiments showed that this is not always the case. By putting a substrate with a thin PS layer into contact with acetic acid, in our case the layer for longer annealing times macroscopically dewetted the substrate.

4.2.4 Ellipsometry

Ellipsometry is a widespread analysis technique for investigation of thin layers, more precisely their dielectric properties. It exploits the property that each of the components, the $p-$ and $s-$ polarized light, is being reflected and transmitted differently upon interaction with the sample. It measures the reflectance $\mathcal{R}$, which is in general a complex

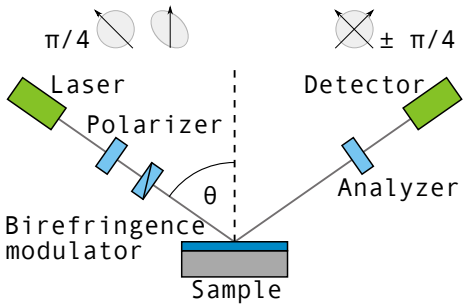

Figure 4.3: Schematic of the fixed wavelength ellipsometer. The angle θ is the incoming angle and is changed during the measurement. All the elements are properly marked and on the top of the figure the change in polarization is marked for each step.

quantity and represents the ratio between the Fresnel coefficients of $p-$ and $s-$ polarized lights:

$$\mathcal{R} = \frac{r_p}{r_s} = \tan(\Psi) e^{i\Delta}\,, \tag{4.3}$$

with Ψ and Δ being the ellipsometric angles, where Ψ represents the amplitude and Δ the phase difference [78]. The incident angle of the measurement has to be chosen close to the Brewster angle $\theta_B = \arctan\left(\frac{n_2}{n_1}\right)$, where n_2 is the refractive index of the second material and n_1 of the first one. Around this angle, the difference between the reflections of $s-$ and $p-$ polarized lights is the biggest, as the $p-$ polarized light is not reflected at the Brewster's angle.

All the measurements were done on a Beaglehole variable angle ellipsometer, the source of which is a HeNe laser of a fixed wavelength of $\lambda = 632.8\,\text{nm}$. The light emitted by the laser is first polarized by a polarizer. It then passes through a birefringence modulator, an electronic element which makes elliptically polarized light with a given frequency of 50 Hz. After the light impinges on the sample, each component gets reflected differently. Finally, an analyzer of $\pm 45°$ which discriminates both amplitudes of the $p-$ and $s-$ polarizations is put in front of the detector. All this can be seen in figure 4.3, where the schematic is shown at the bottom and the polarization change after each step at the top. The device measures the two components, the real and the imaginary part:

$$\text{Re}(\mathcal{R}) = \tan\Psi\cos\Delta \;\;;\;\; \text{Im}(\mathcal{R}) = \tan\Psi\sin\Delta\,. \tag{4.4}$$

At the Brewster angle, the real part will get to 0 and the highest contrast will be achieved. Each measurement yields only two points, each at a different polarization axis. In order to complete the measurements, the angle is scanned at least $\pm 50°$ around the Brewster angle of Si ($\theta_B = 75.6°$ at $\lambda = 632.8\,\text{nm}$).

4.3 Experimental results

4.3.1 Reflectivity model and results

The samples of different thicknesses of d-PS layer were measured in order to obtain the interfacial width as a function of thickness, i.e. the distance from the substrate. During the reflectometry measurements, only the squared modulus of the reflectivity is recorded, with phase information being lost, as already described in chapter 2.1. In order to establish the structure of a sample in real space, a model has to be constructed and then iteratively compared (fitted) to the data. For the samples presented here, there is an obvious choice with each individual physical layer being itself a layer in the model. The interfacial width is considered to be the width of an error function; the projection of a Gaussian distribution of height deviations from the ideal smooth interface. Additionally to the polymer layers, there is always a thin oxide layer covering bare Si substrates. Depending on the crystal cut, the thickness can be as low as $\sim 25\,\text{Å}$ for Si (111) [79] or as high as $\sim 40\,\text{Å}$ for Si (100) [80] and are typically around $\sim 20\,\text{Å}$.

Firstly, a 3-layer model SiO_2 / d-PS / h-PMMA was constructed, with Si as a substrate and air as the top semi-infinite medium. While a 3-layer model including roughness at the interfaces is sufficient to describe the Kiessig fringes coming from the thicknesses of the top and bottom layers, it is unable to reproduce the fine modulation of the data, especially around the minima. It is at least very complicated, if not impossible, to fit the data without rough prior knowledge of the parameters (shown in table 4.3). By fitting with this information as starting parameters, one can see how well the model matches with the data. It turns out that in our case, a 3-layer model is insufficient in correctly describing this fine structure. As will be shown later, the additional interfacial layer, necessary to get a satisfying specular fit, is extremely important to account for the off-specular scattering intensity. By adding an additional layer between the d-PS and h-PMMA, one can start to correctly describe the data. By introducing this layer, the tail region of the interface is extended, showing an asymmetric shape. This is shown in figure 4.4b and is very well reflected in the χ^2 values and by zooming in on the fitted curves, as shown in figure 4.5. This implies that the h-PMMA top layer is nucleating on top of the d-PS. Even though the choice of the model seems arbitrary, the off-specular measurements, discussed later, clearly point to a much bigger interfacial region than a simple 3-layer model with Gaussian roughness would suggest. The recorded intensity requires a much larger scattering volume, than the one predicted by the Gaussian roughness alone.

Another aspect to note are the holes in the top layer, which was investigated with atomic force microscopy (AFM) and is described in section 4.3.3. When the SLD deviations come from the thickness of the whole layer, this can only marginally change the SLD of a layer in the specular model (e.g. a few percent of air in h-PMMA is within the fit error, where the nominal SLD is $1.059 \times 10^{-6}\,\text{Å}^{-2}$), which is averaged over large areas of the coherence length, but cause visible off-specular signal, as the intensity scales with the thickness d as $\sim d^2$.

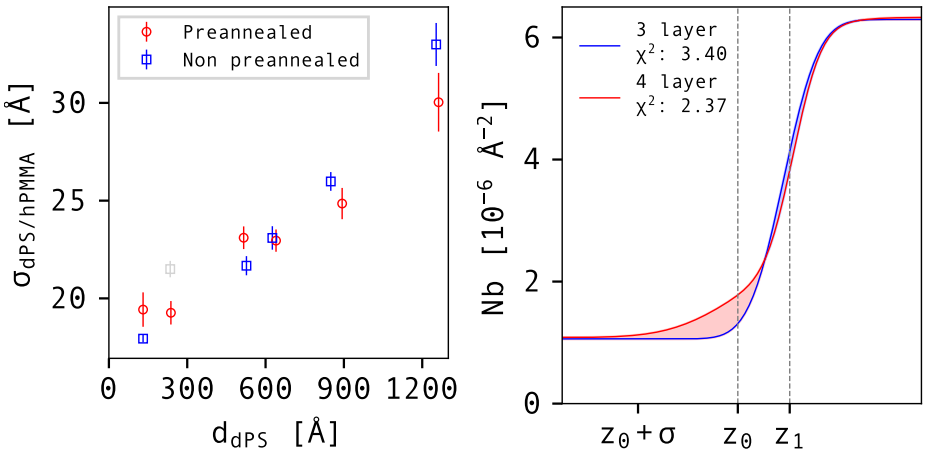

(a) (b)

Figure 4.4: (a) Plot of the Gaussian roughness between d-PS and h-PMMA, assuming only a 3-layer model. There is no difference between the two series visible. (b) Comparison of the interfacial region of the two SLD profiles, from 3-layer and 4-layer models, that elsewhere look identical.

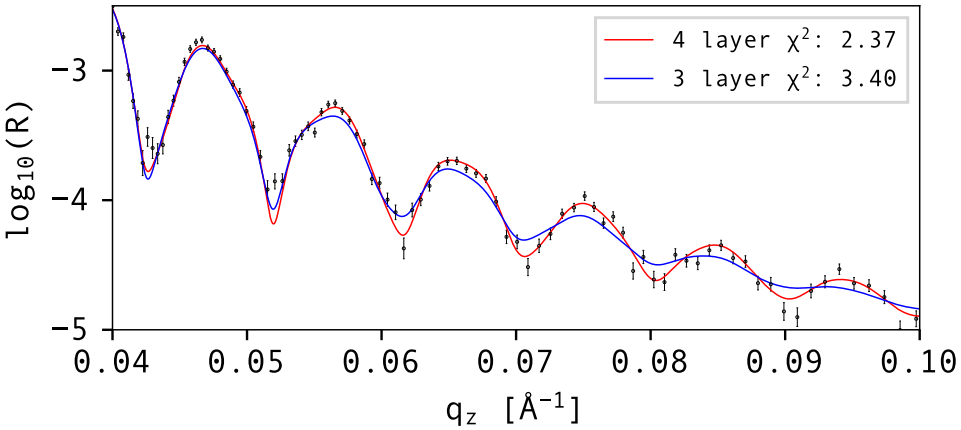

Figure 4.5: Zoom of specular reflectivity using a 3-layer and a 4-layer model, clearly showing the reproduction of features by the second.

Eventually, all the specular reflectivity was fitted with a 4-layer model as described above, however, the 4-layer model deviates negligibly for the two thinnest preannealed samples (F and E), showing a possible stabilization of the bottom layer through irreversible adsorption. The measured data and the fitted curves are shown in figure 4.6 and their corresponding SLD profiles in figure 4.7. It can be seen that there is not much apparent difference between the two series of samples. This is also reflected in the Gaussian width of the interface, as shown in figure 4.4a. By using the 4-layer model, one can define the

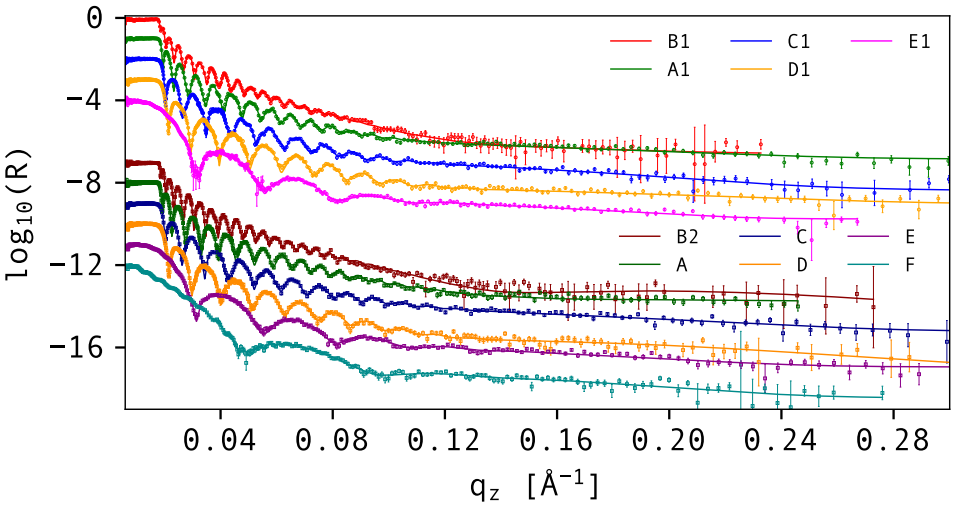

Figure 4.6: Specular reflectivity for non-preannealed and preannealed samples with corresponding fits. All sample parameters are in table 4.3. Curves are offset by factor 10x for clarity.

extent of the d-PS excess at the interface (i.e. the total extent of d-PS in h-PMMA) as:

$$d_{\text{excess}} = \int_{z_{\text{int}}} x(z)dz\,, \tag{4.5}$$

where $x(z)$ is the dimensionless volume fraction of d-PS, which ranges from 0 in the h-PMMA layer and goes to 1 in the d-PS layer:

$$x(z) = \frac{Nb(z) - Nb_{\text{dPS}}}{Nb_{\text{hPMMA}} - Nb_{\text{dPS}}}\,. \tag{4.6}$$

The integration z_{int} runs over the whole interfacial region from $z_0 + \sigma$ to z_1 from figure 4.4b. This way, an interface with asymmetric shape can be correctly evaluated, the excess representing the area below the normalized volume fraction, and is in units of Å. A dependence on thickness and difference between the two series can now be seen in figure 4.8. A trend emerges, which was not visible before, that for the preannealed samples the total interfacial extent is around 55 Å. This corresponds to the interfacial width between h-PMMA and d-PS on the order of $\sigma = 55\,\text{Å}/2.355 \sim 23\,\text{Å}$. However, for the non-preannealed samples, a significant deviation from the expected width from the model is observed.

Additionally, such an asymmetric profile at an interface may be indicative of a layer breakup (i. e. d-PS in the top layer) and may be connected to the surface dewetting observed. The asymmetry is much more pronounced for thicker layers ($d > 250\,\text{Å}$), where the deviation from the 3 layer model is bigger. The quantification of the excess is also the basis for calculation of the off-specular scattering, as the whole interfacial region is assumed to be involved in the correlated roughness.

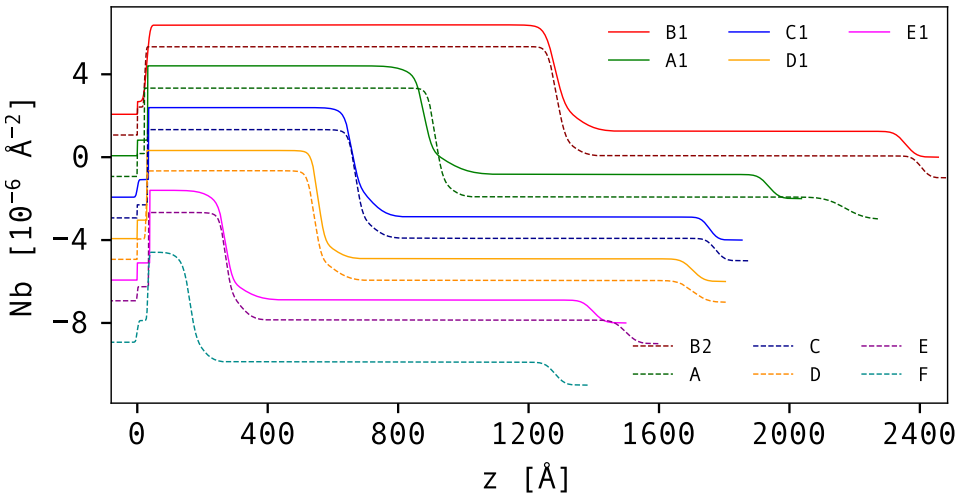

Figure 4.7: Scattering length density profiles for non-preannealed and preannealed samples from specular reflectivity fits. All the sample parameters are in table 4.3. Curves are offset by factor 10x for clarity. $z = 0$ denotes the location of the Si / SiO_2 interface.

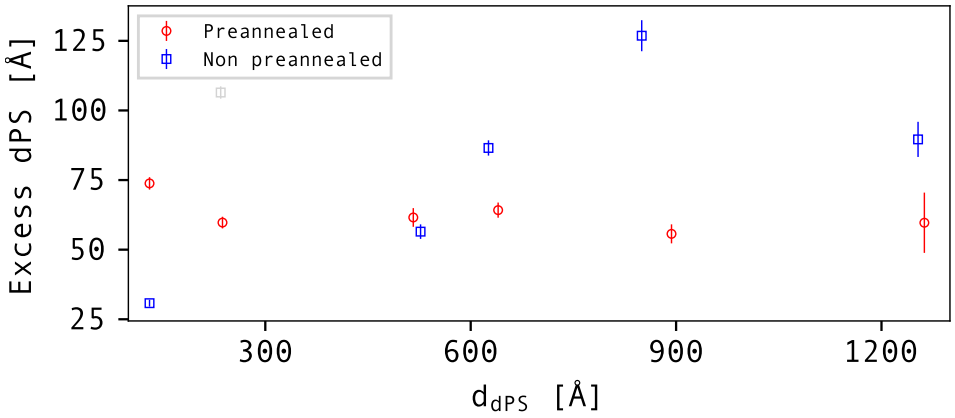

Figure 4.8: Excess length of d-PS at the d-PS / h-PMMA interface. Since the interface is asymmetric, the excess of d-PS is plotted, rather than only roughness.

4.3.2 In-plane correlation length

In-plane correlation length can be extracted with the use of the DWBA off-specular formalism, previously presented in chapter 2.2, more precisely, using equation 3.20. The consequence of the correlation length ξ in real space is a cutoff at a given wavevector $q_{\text{cutoff}} = 2\pi/\xi$. As shown in figure 4.9, the off-specular region of both series of samples looks very different, whereas the interfacial width remains more or less constant for preannealed samples and increases with thickness for non-preannealed samples. Since the Lorentzian peak shape is normalized (Eq. 3.20), a higher width ξ means a higher peak

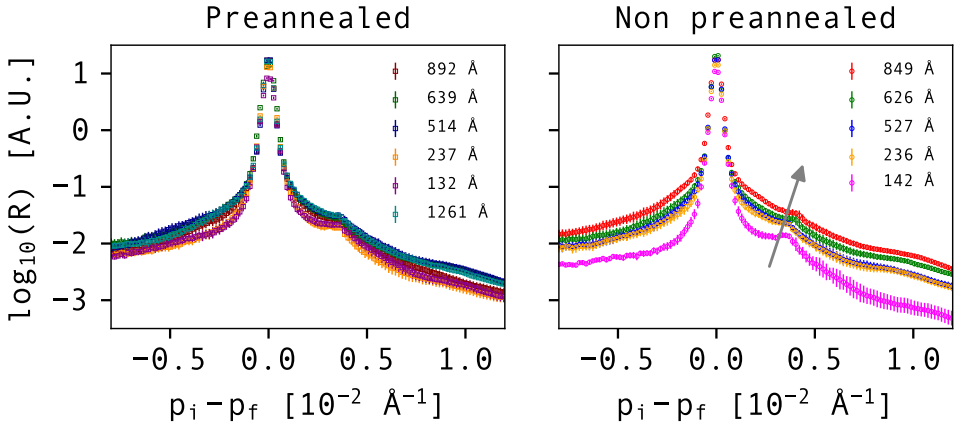

Figure 4.9: Integrated intensity along q_z in $(p_i - p_f, q_z)$ space, where optical effects are much better visible. It can clearly be seen that the off-specular spectrum broadens with increasing thickness of the bottom layer in non-preannealed samples. The peak at $p_i - p_f = 0.37 \times 10^{-2}\,\text{Å}^{-1}$ corresponds to the h-PMMA Yoneda peak. The labels denote the thickness of the bottom d-PS layer.

with narrower width, rather than the other way around. Prior measurements have shown that the width of a polymer-polymer interface measured with neutron reflectometry is larger than that predicted purely by self-consistent field theory because of the additional amplitude of thermally excited capillary waves [81], [82]. For such an interface, two cutoff length scales can be hypothesized. The first one being the high wavevector cutoff, coming from the intrinsic interface [68]:

$$a_{\text{int}} = \frac{\sqrt{2} w_l}{\sqrt{\pi}}\,, \tag{4.7}$$

with w_l being connected to the Flory-Huggins theory by the statistical length of one monomer $a = 7\,\text{Å}$ and the interaction parameter $\chi = 0.037$ as estimated from small angle neutron scattering measurements [83]:

$$w_l = \frac{a}{\sqrt{\chi}}\,. \tag{4.8}$$

The second one being the low wavevector cutoff, coming from the dispersive capillary wave term [68]:

$$a_{\text{dis}} = \sqrt{\frac{4\pi\gamma d^4}{|A_{\text{eff}}|}}\,, \tag{4.9}$$

where γ is the interfacial tension, d the thickness of the layer, and A_{eff} the effective Hamaker constant of the system. Furthermore, large wavelengths will be suppressed by gravity and cause an additional cutoff $a_{\text{grav}} = \frac{2\gamma}{g\Delta\rho}$, with g being the gravitational

acceleration and $\Delta\rho$ the difference in mass densities of two phases. However, this length scale is on the order of a few mm and is thus far greater than the lateral neutron coherence length $\lambda_{\text{coh}} \sim \frac{2\pi}{\Delta q_x}$, which on D17 is in the range of $20\,\mu\text{m} < \lambda_{\text{coh}} < 150\,\mu\text{m}$. Taking now into consideration our model from eq. 3.20, critically assessing the contributions to the spectrum, one can neglect the contribution of a very low wavevector cutoff by the coherence length, as its effects are already contained inside the width of the specular Gaussian peak. Secondly, the high wavevector cutoff by the statistical monomer segment length can also be neglected, as such a small length causes scattering into a very broad area, which in our experiments is indistinguishable from incoherent scattering and background. Finally, we are left with one cutoff ξ, namely the one coming from the van der Waals force limiting the capillary wave spectrum. As a reference, all the experimental fits are shown in table 4.4.

For our experimental system of Si / SiO2 / d-PS / h-PMMA / Air, we can estimate the Hamaker constant between two macroscopic phases (1 - air) and (3 - PS), separated by a medium (2 - PMMA), with the Lifshitz theory [84]:

$$A_{\text{eff}} = \frac{3k_BT}{4}\left(\frac{\epsilon_1-\epsilon_2}{\epsilon_1+\epsilon_2}\right)\left(\frac{\epsilon_3-\epsilon_2}{\epsilon_3+\epsilon_2}\right) + \frac{3h\nu_e}{8\sqrt{2}}\frac{(n_1^2-n_2^2)(n_3^2-n_2^2)}{\sqrt{n_1^2+n_2^2}\sqrt{n_3^2+n_2^2}\left(\sqrt{n_1^2+n_2^2}+\sqrt{n_3^2+n_2^2}\right)}, \quad (4.10)$$

with ϵ_i and n_i being the dielectric constant and refractive index of medium i, and ν_e the main electronic absorption frequency in the UV ($\nu_e \sim 2.3 \times 10^{15}\,\text{s}^{-1}$). By inserting the numbers we get an estimation of $A_{\text{eff}} = -1.56 \times 10^{-20}\,\text{J}$. The interfacial tension γ between PS and PMMA can be estimated using [85]:

$$\gamma = a\rho k_BT\sqrt{\frac{\chi}{6}}, \quad (4.11)$$

with $a = 7\,\text{Å}$ being the statistical segment monomer length, $\rho^{-1} = 174\,\text{Å}^3$ being the volume of the monomer repeat unit, $T = 433\,\text{K}$ the annealing temperature and $\chi = 0.037$ the interaction parameter as defined before [68]. Inserting the numbers, one obtains $\gamma = 1.9 \times 10^{-23}\,\text{J}\,\text{Å}^{-2} = 1.9\,\text{mJ}\,\text{m}^{-2}$.

Assessing now the expected dispersive capillary wave cutoff length from self-consistent field theory as defined by equation 4.9 with the numbers derived above, one obtains the relation shown in figure 4.10. As can be seen in figure 4.9, the integrated measured off-specular spectrum differs considerably for both series of samples. The extracted cutoff length ξ at the interface is shown in figure 4.11a. They are in the range of a few thousands Å, meaning that apart from the thinnest two preannealed samples, the cutoff length is lower than that predicted by the theory.

As the result of equation 4.9 is linearly dependent on the Hamaker constant and the approximation used does not take the Si / polymer interaction into account, it is worth

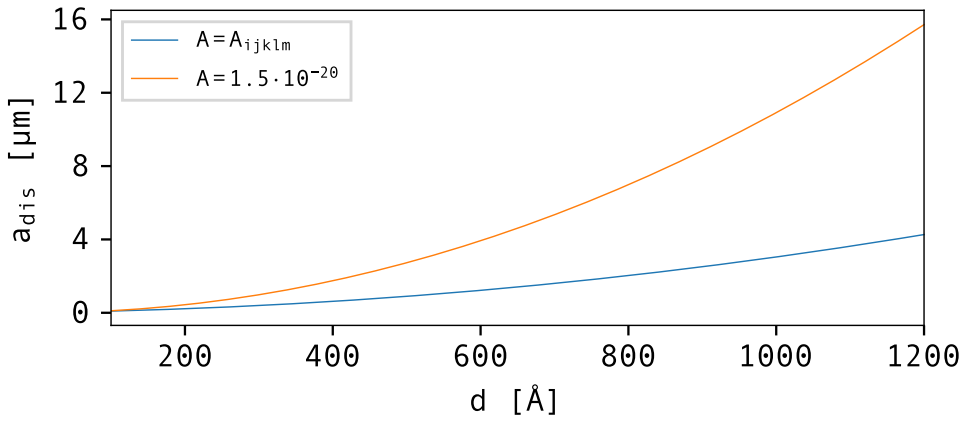

Figure 4.10: Theoretically predicted dispersive cutoff due to capillary waves from eq. 4.9, once for a constant Hamaker constant $A = 1.5 \times 10^{-20}$ J and once using the thickness-dependent Hamaker constant of a 5-layer system, as defined in eq. 4.15.

further assessing it. The constant value obtained before has been used by relevant studies in the past [68], but it can be further expanded to obtain the thickness dependence and to include the effects of Si and SiO_2 and effectively treat the full 5-layer experimental system (Si / SiO_2 / PS / PMMA / Air). This can be done through the procedure described in [86]. First, let us consider a general expression for the Hamaker constant between materials i and k, interacting over the medium j:

$$A_{ijk} = \frac{3k_BT}{4}\left(\frac{\epsilon_i - \epsilon_j}{\epsilon_i + \epsilon_j}\right)\left(\frac{\epsilon_k - \epsilon_j}{\epsilon_k + \epsilon_j}\right) + \frac{3h\nu_e}{8\sqrt{2}} \frac{(n_i^2 - n_j^2)(n_k^2 - n_j^2)}{\sqrt{n_i^2 + n_j^2}\sqrt{n_k^2 + n_j^2}\left(\sqrt{n_i^2 + n_j^2} + \sqrt{n_k^2 + n_j^2}\right)}, \quad (4.12)$$

with the quantities being the same as in eq. 4.10. Now, we can define the effective Hamaker constant of a 4-layer system (Si / SiO_2 / PS / PMMA), acting on the PS layer [86]:

$$A_{1234} = A_{234} + \frac{A_{134} - A_{234}}{\left(1 + \frac{d_4}{d_3}\right)^3}, \quad (4.13)$$

with 1, 2, 3, 4 being the respective layer in the system. In order to correctly describe all the interactions, another 4-layer system has to be calculated, taking into account the interaction with air (Si / SiO_2 / PS / Air):

$$A_{1235} = A_{235} + \frac{A_{135} - A_{235}}{\left(1 + \frac{d_2}{d_3}\right)^3}. \quad (4.14)$$

Finally, the expression for a thickness-dependent effective Hamaker constant of a 5-layer system on PS layer is:

$$A_{\text{eff, PS}} = A_{1235} + \frac{A_1234 - A_{1235}}{\left(1 + \frac{d_3}{d_4}\right)^3}\,. \tag{4.15}$$

Now plotting the expression 4.9, a slightly smaller dispersive length is obtained, as shown in figure 4.10, and its plot with the experimental values of ξ obtained from the data can be seen in figure 4.11a. Looking closely at the figure, one can see that the first 2 values of the preannealed samples match up with the predicted length, but further on, the values start to deviate, as the theory is predicted to grow with d^4. This shows that for a sufficiently thin film, the whole film is adsorbed and cannot break, which is also reflected in the fact that for these two films, a 3-layer specular model does not differ significantly from a 4-layer model. Assessing the two points further, one can run multiple calculations and estimate the error as well.

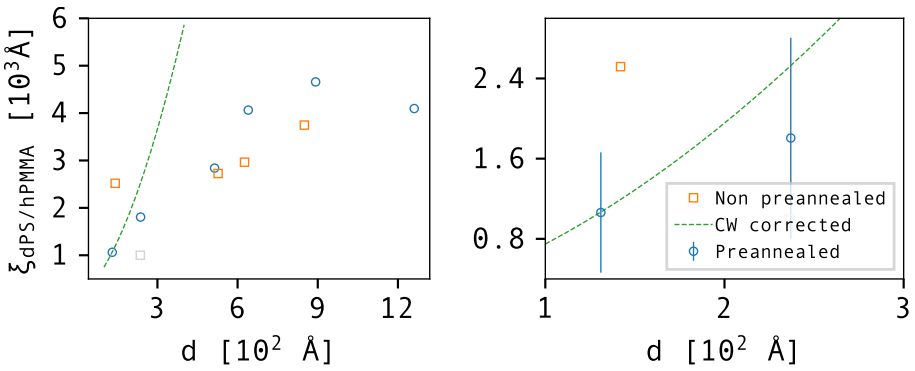

(a)

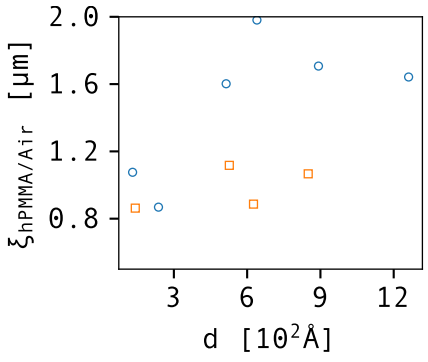

(b)

Figure 4.11: The two correlation lengths ξ shown side by side. (a, left) The $\xi_{\text{dPS/hPMMA}}$ is at the interface between the dPS and the hPMMA, the dashed line is showing the equation 4.9 with A from eq. 4.15. (a, right) Showing the inset of the two thinnest layers, which nicely align with the prediction of formula 4.15. (c) $\xi_{\text{hPMMA/Air}}$ is showing the distance between the holes in the top layer.

Table 4.4: List of samples with their corresponding fits from the text.

Name	Annealing [h]	Fig. $(\lambda, \theta_i + \theta_f)$	Fig. $(p_i - p_f, p_i + p_f)$
A	48 + 12	4.19, 4.17b	A.2
B2	48 + 12	4.29	A.9
C	48 + 12	4.22, 4.20b	A.4
D	48 + 12	4.25, 4.23b	A.6
E	48 + 12	4.28, 4.26b	A.8
A1	12	4.18, 4.17a	A.1
B1	12	Bent sample	
C1	12	4.21, 4.20a	A.3
D1	12	4.24, 4.23a	A.5
E1	12	4.27, 4.26a	A.7

4.3.3 Top surface

Atomic force microscopy (AFM) in tapping mode (Asylum Research MFP-3D) was used to verify the top surface for holes. The size of scans was 50 Å × 50 Å in 512 × 512 grid of square points with the size of 97 nm.

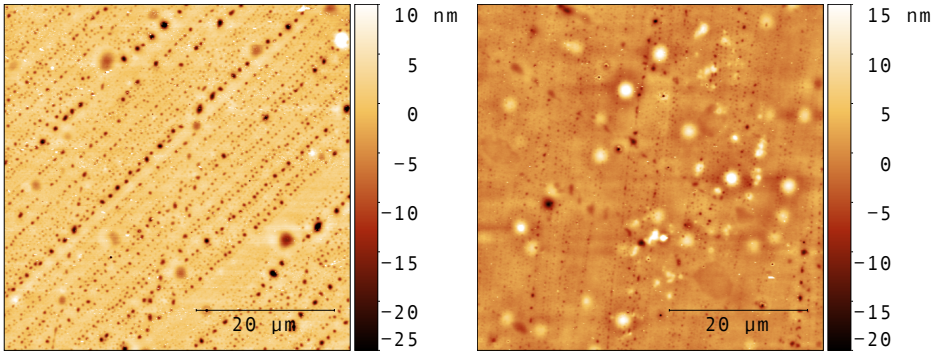

(a) (b)

Figure 4.12: AFM topographies (height traces) of the top surface at the same annealing time as reflectivity measurements. Both samples show aligned holes visible as black spots. They are caused by heterogeneous nucleation of the top h-PMMA layer, aligned due to the floating from glass. (a) Sample A1. (b) Sample D.

Two such images are shown in figures 4.12a and 4.12b, where the top surface shows aligned features in the form of holes. We suspect that these are a consequence of replication of roughness from the glass slides, which were used for floating the top layer. This could potentially be improved by spin coating on mica, as it can be polished to a much lower surface roughness. In any case, the roughness would pin the holes. Despite the

coverage being very low, on percent level, the majority of the off-specular signal is coming from these holes. Another contribution to the spectrum was therefore applied throughout the top layer, which for a very low concentration of holes in h-PMMA ($c < 5\%$) would not change the mean SLD much and is within the fitting error of specular fits. As will be visible in the next section, such an addition is crucial. The values of the correlation length ξ are shown in figure 4.11b and appear to be more or less constant for the two series. The error of the fit from a genetic algorithm is rather hard to estimate, as multiple fits have to be performed, comparing the χ^2 simultaneously.

4.3.4 Contributions to off-specular intensity

In order to corroborate the results described above, a series of figures is presented here, showing how different contributions add up to the total spectrum. As the measurement is the total off-specular intensity coming from the samples, each individual contribution is individually assessed here. This cannot be done experimentally, unless the observed system is changed and re-measured. Using a computational algorithm presented before, the contributions can easily be turned on and off and inspected.

The total spectrum consists of two contributions: the scattering coming from the perturbation caused by holes (filled with air) in the top h-PMMA layer, and the scattering from the interface of interest, between h-PMMA and d-PS. The first one scales with d^2, where d is the thickness of h-PMMA. Therefore, already a very small concentration of holes causes huge contribution to the spectrum, as $d \sim 1100\,\text{Å}$. As can be seen in figure 4.13, the scattering is mostly concentrated in the high-wavelength region, close to the h-PMMA critical angle, and falls quickly at higher q_z. The holes are represented as two distinct phases with two SLDs, one inside the hole and one in the rest of the layer. The differential scattering cross-section can then be calculated using the equation 2.79. In the case of holes filled with air, the contrast between air and h-PMMA is very low. Such scattering would be negligible without a very large scattering volume in which it takes place. Without this contribution, the shape of the specular beam at high wavelengths cannot be correctly reproduced, as seen in both 4.14 and 4.15, which lack the aforementioned contribution. The specular ridge is noticeably broadened at higher wavelengths. Due to the broadening being wavelength dependent, it cannot be a geometrical property of the beam and must come from the sample itself. As it turns out, each layer with its respective contrast influences a different part of the spectrum, its position roughly being defined by the corresponding critical edge. The position of the features is therefore qualitatively very indicative of the source of the perturbation in the sample, giving rise to the intensity in the off-specular spectrum.

The other source of off-specular scattering is located at the interface of interest between the h-PMMA and d-PS. However, the amplitude of Gaussian roughness is not enough to describe it. The shape of the curve and its features in the spectrum are of course correctly described even by the Gaussian roughness from a 3-layer model (fig. 4.14), since they come from the same wave field modulation. However, their absolute intensity is almost an order of magnitude weaker, as their intensity scales with σ^2. This is much less than

the real total extent of the interface, which was described by adding a layer of mixed h-PMMA and d-PS of thickness d_{mixed} (shown before in figure 4.8). By considering a larger scattering volume, the features very nicely line up with the experimental data in the low-wavelength region (high q_z), which is dominated by the critical reflection of d-PS, and therefore the information coming from its interface. The contribution to off-specular intensity coming from the extended interface is shown in figure 4.15. In figure 4.16, the same plots are presented also in $(p_i - p_f, p_i + p_f)$ space.

Finally, the full, fitted spectrum is shown in figures 4.19 and 4.17b in $(\lambda, \theta_i + \theta_f)$ space. As shown, it is a combination of the two contributions, the holes in the top layer, correctly describing the high-wavelength region, and the extended interfacial region, correctly describing the low-wavelength region. It has to be noted that, if fitting the OSS in arbitrary scale, one can easily be misled by the nicely aligned features described already by the Gaussian roughness from the 3-layer model.

All the fits to samples of different thicknesses are presented in the following figures: A 4.19, 4.17b), B2 (4.29), C (4.22, 4.20b), D (4.25, 4.23b), E (4.28, 4.26b), A1 (4.18, 4.17a), C1 (4.21, 4.20a), D1 (4.24, 4.23a), E1 (4.27, 4.26a). Additional, transformed plots in $(p_i - p_f, p_i + p_f)$ space are shown in appendix A.

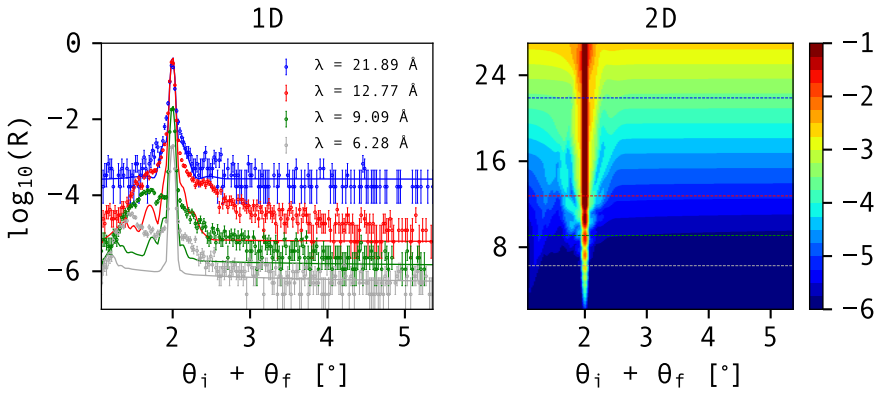

Figure 4.13: Sample A, off-specular intensity coming from the holes in the top h-PMMA layer. Area concentration of holes is 1%.

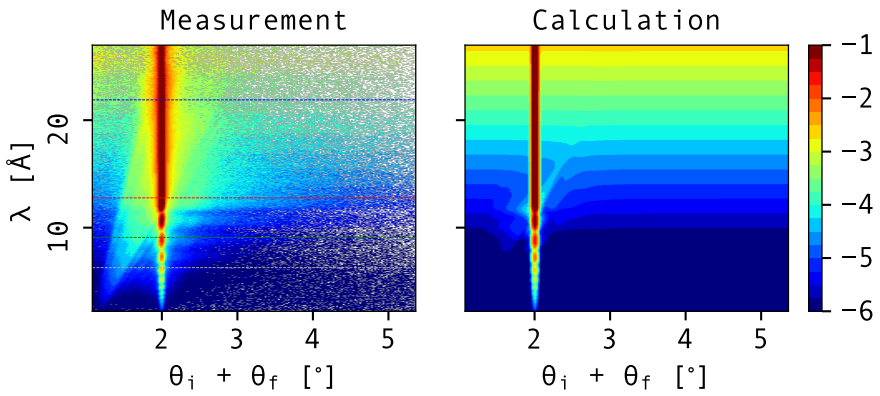

Figure 4.14: Sample A, off-specular intensity is only coming from the roughness σ at the interface between d-PS and h-PMMA, as predicted by the 3-layer model.

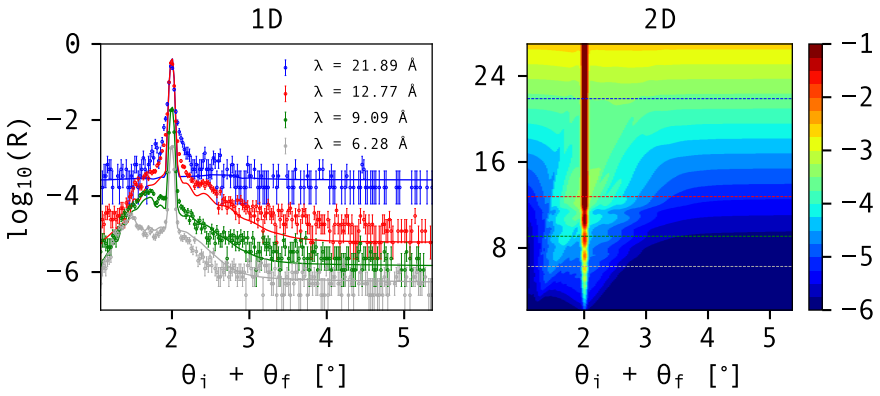

Figure 4.15: Sample A, off-specular intensity is coming from the extended interface between d-PS and h-PMMA, meaning an increased scattering volume.

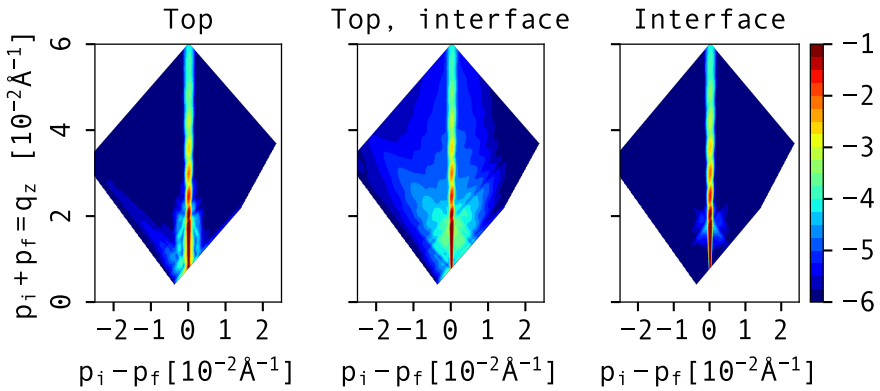

Figure 4.16: Different contributions in $(p_i - p_f, p_i + p_f)$ space, namely with top interface contribution, top and interfacial contribution, and only the interfacial contribution from the 3-layer model.

4.4 Outlook and conclusion

Firstly, as can be seen, the off-specular scattering yields additional information, which not only improves the specular fits, but also influences their general outcome and physical interpretation. Sometimes, this can mean that a significant departure from the original simple model is necessary. In our case, the fits with the 3-layer model could easily be considered good enough, if only looking at specular reflectivity. However, by fitting both the specular and off-specular part at the same time, it becomes obvious that, there is simply not enough scattering volume (considering only a Gaussian interface) between the two polymers, to correctly describe the results. Despite not being able to show the influence of a pre-adsorbed layer on the overlying polymer-polymer interface by the change of capillary wave amplitude (represented as the roughness at the interface σ) as hypothesized, we were able to quantitatively show the change in cutoff length between the two series of samples and furthermore confirm the effect that pre-annealing has on a bilayer system.

Qualitatively, the effect can be seen in figure 4.9. The difference between the two series is apparent and it seems that the preannealing stabilizes the layer by adsorption of polymer onto the substrate. It is, however, impossible to determine whether the adsorbed amount of the polymer was higher in one or another series. An independent measurement on single dPS layers pre-annealed for different times showed that in 12 h annealing, only a thin layer is irreversibly adsorbed onto the silicon, independent on the initial film thickness. In 60 h the entire film starts interacting with the silicon [38], which qualitatively corroborates the difference between pre-annealed and non-preannealed samples, shown in the current study.

Besides that, such a bilayer is a rather complicated example of off-specular scattering, which is also reflected in the amount of information that was needed to fit the result. This clearly demonstrates the power and necessity of the previously presented complete reflectometry algorithm, which enables one to fit specular and off-specular reflectivity simultaneously in absolute scale. A further step in investigations of the effect of adsorbed molecules on the overlying polymer-polymer interface would be to measure the stable, inversed Si / d-PMMA / h-PS / air system. Because such a system is stable [68], the roughness at the interface could only come from the intrinsic interfacial width and the capillary waves. This way, only the contribution of the latter could be quantified. However, for predicted amplitudes, the scattered signal is rather low and would be very challenging to detect, as shown in figure 4.14.

One of the main goals of this research was also to measure the bilayers of different thicknesses as model systems for the validation of the off-specular scattering algorithm presented in chapter 3. This was very successful, as we have managed not only to correctly identify the individual contributions to the scattering pattern, but also to quantitatively disentangle the effects from the total spectrum. Furthermore, different types of physical phenomena responsible for the features in the spectrum, optical or structural, have also been identified and the algorithm correctly reproduces them. This opens up new possibilities for a more general use of off-specular reflectivity also to

unknown systems, as, by constraining the intensity to the structural parameters (just like in specular reflectivity) and their ratio to the specular peak, it significantly improves the specular fits.

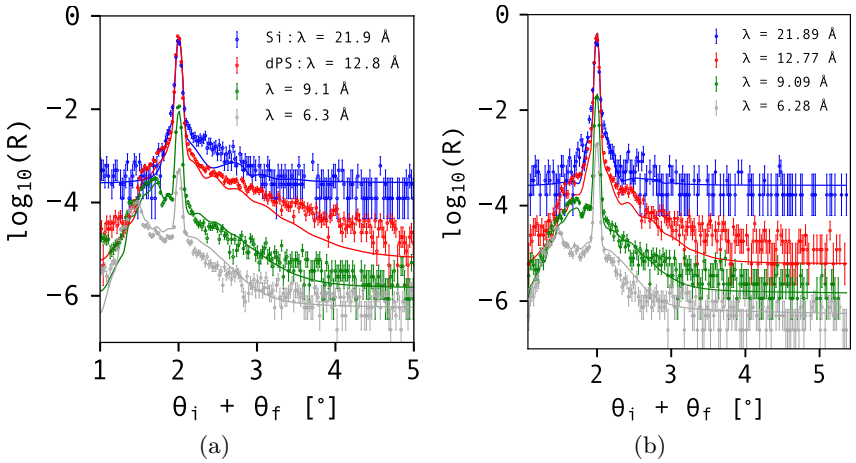

(a) (b)

Figure 4.17: (a) Non-preannealed sample A1, with thickness of dPS, $d_{\mathrm{dPS}} = 850\,\text{Å}$. (b) Preannealed sample A, with thickness of dPS, $d_{\mathrm{dPS}} = 892\,\text{Å}$.

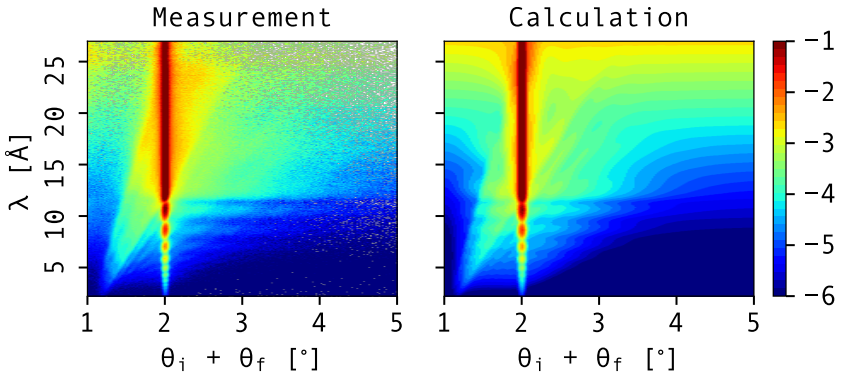

Figure 4.18: Sample A1, thickness of dPS, $d_{\mathrm{dPS}} = 850\,\text{Å}$.

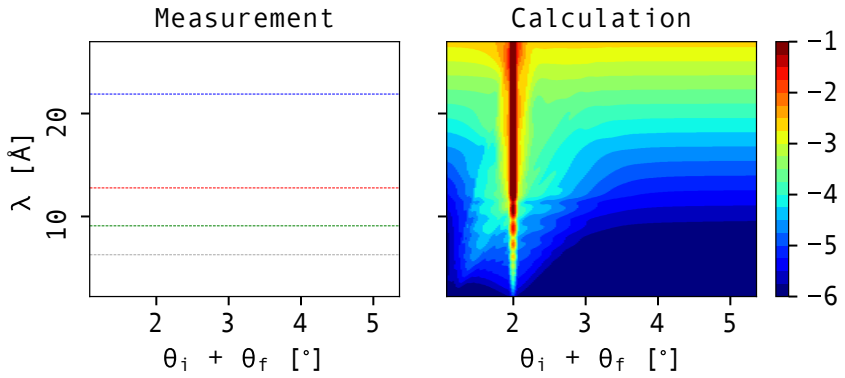

Figure 4.19: Sample A, thickness of dPS, $d_{\mathrm{dPS}} = 892\,\text{Å}$.

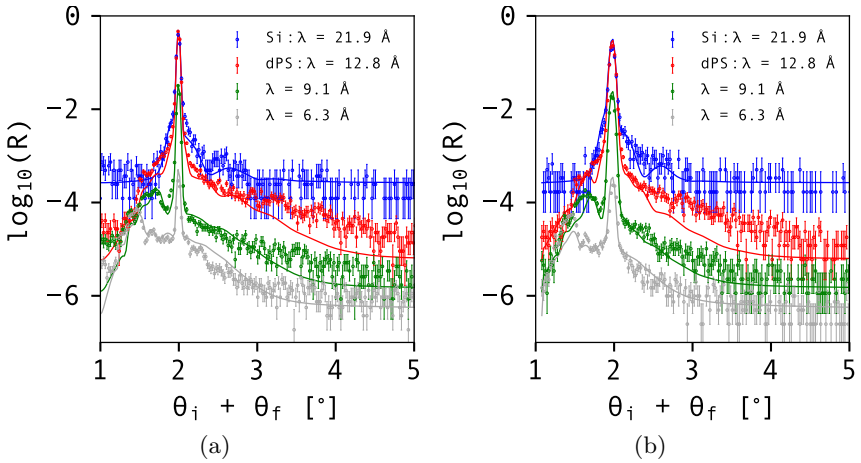

Figure 4.20: (a) Non-preannealed sample C1, with thickness of dPS, $d_{\mathrm{dPS}} = 626\,\text{Å}$. (b) Preannealed sample C, with thickness of dPS, $d_{\mathrm{dPS}} = 640\,\text{Å}$.

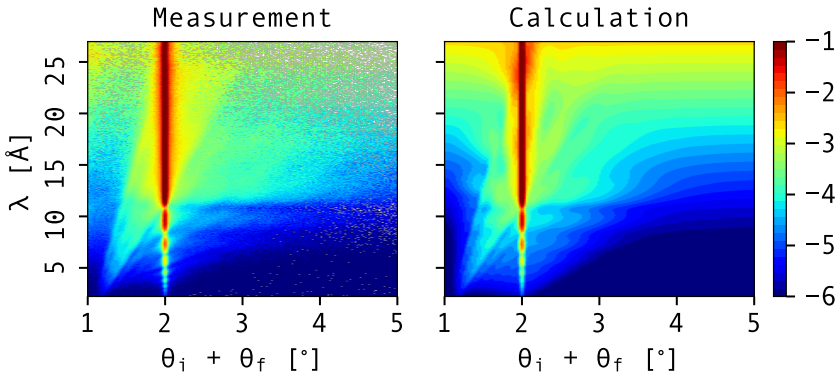

Figure 4.21: Sample C1, thickness of dPS, $d_{\mathrm{dPS}} = 626\,\text{Å}$.

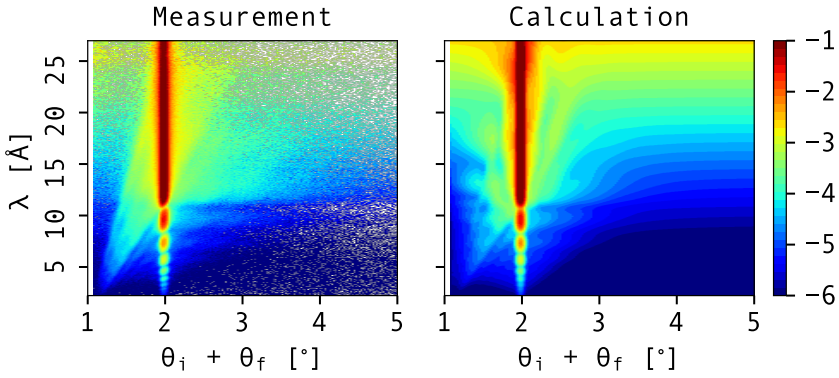

Figure 4.22: Sample C, thickness of dPS, $d_{\mathrm{dPS}} = 640\,\text{Å}$.

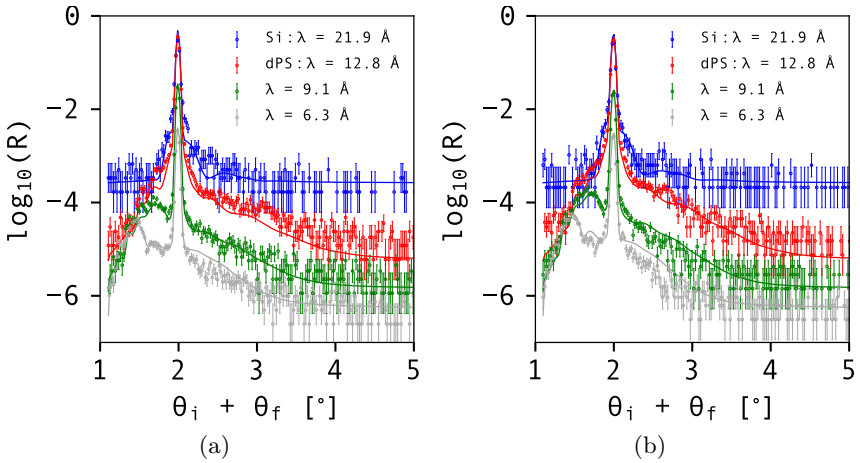

Figure 4.23: (a) Non-preannealed sample D1, with thickness of dPS, $d_{\mathrm{dPS}} = 527\,\text{Å}$. (b) Preannealed sample D, with thickness of dPS, $d_{\mathrm{dPS}} = 514\,\text{Å}$.

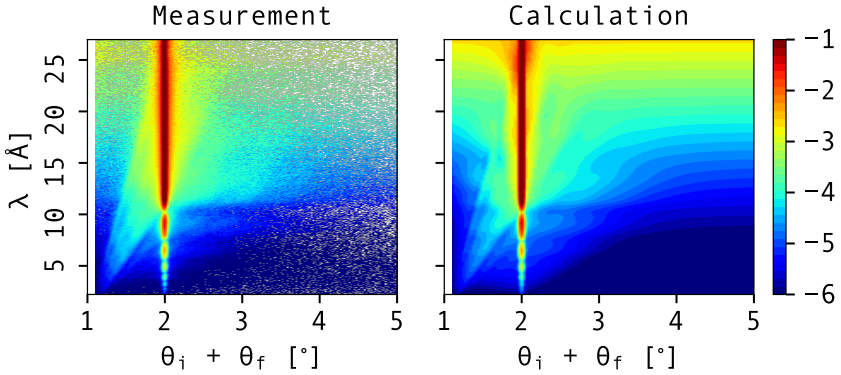

Figure 4.24: Sample D1, thickness of dPS, $d_{\mathrm{dPS}} = 527\,\text{Å}$.

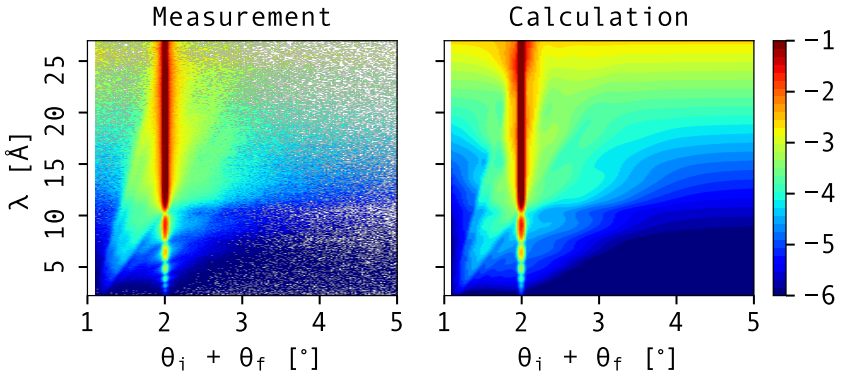

Figure 4.25: Sample D, thickness of dPS, $d_{\mathrm{dPS}} = 514\,\text{Å}$.

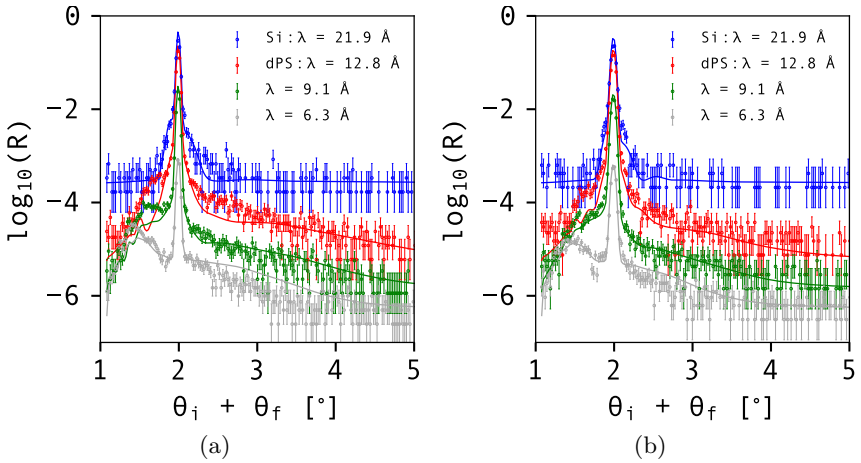

Figure 4.26: (a) Non-preannealed sample E1, with thickness of dPS, $d_{\mathrm{dPS}} = 236\,\text{Å}$. (b) Preannealed sample E, with thickness of dPS, $d_{\mathrm{dPS}} = 237\,\text{Å}$.

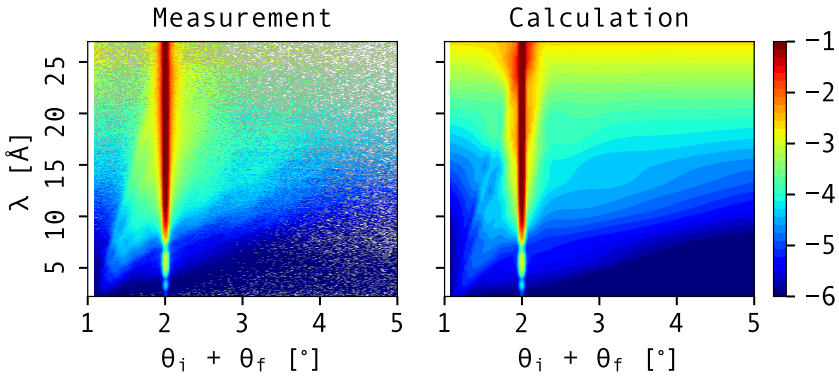

Figure 4.27: Sample E1, thickness of dPS, $d_{\mathrm{dPS}} = 236\,\text{Å}$.

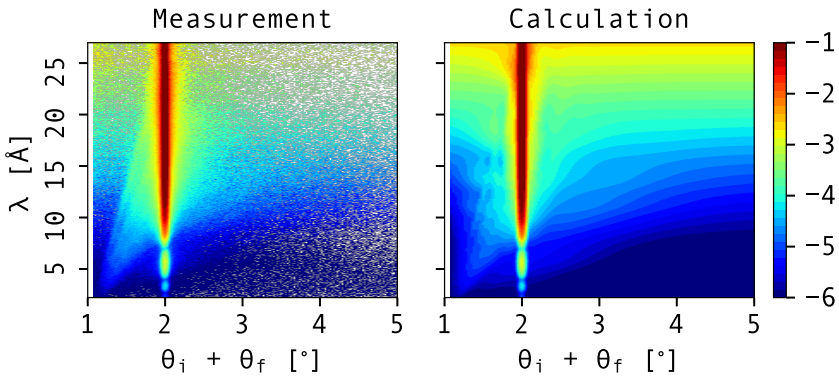

Figure 4.28: Sample E, thickness of dPS, $d_{\mathrm{dPS}} = 237\,\text{Å}$.

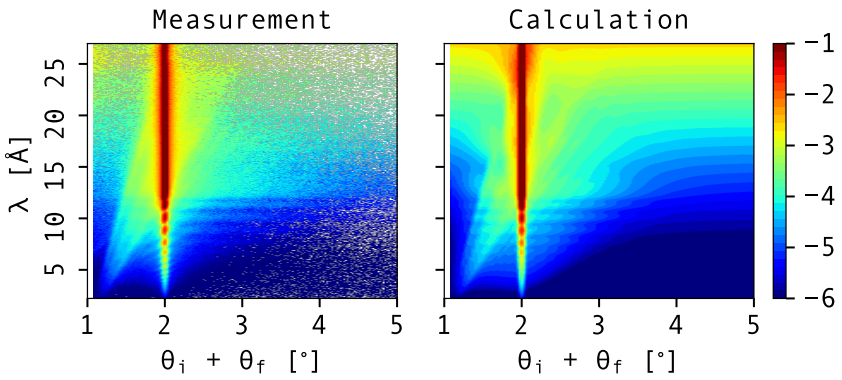

Figure 4.29: Sample B2, thickness of dPS, $d_{\mathrm{dPS}} = 1261$ Å.

5 Destabilization of a buried thin polymer film

5.1 Introduction

As discussed in chapter 4, confinement effects on the buried polymer-polymer interface can be tuned by changing the thickness of different layers. The results shown in figure 4.9 show a clear difference between the pre-annealed and non pre-annealed samples. However, as we detected various additional features, such as a formation of holes in the top layer and a possible onset of breakup of the bottom layer, due to the extended interfacial region, further investigations will be discussed in this chapter.

Firstly, a system of a 155 Å thin d-PS on Si, capped with 1700 Å h-PMMA, was prepared. The system was observed without preannealing and the whole process of breakup of a buried layer was measured as a function of annealing time in steps of 10 min at $T = 160\,^{\circ}\mathrm{C}$. This gives the evolution of the breakup of the buried thin layer, as well as the breakup of the top thicker layer. The experiment and its results are described in 5.2.

Secondly, a much thicker film, ~ 3000 Å instead of ~ 1200 Å, was deposited on top of a 120 Å thin d-PS layer. A layer of such thickness is itself already too thick to show any thin film confinement effects and furthermore makes the distance from the polymer-polymer interface to the free surface very large. Thus making its contribution negligible. It is still thin enough to be investigated by reflectometry, as the perpendicular coherence length is on the order of $\sim 1\,\mu\mathrm{m}$. As shown in the results in section 5.3.1, the neutron reflectivity and OSS are distinctively different due to the top layer being stable and do not show any extended interfacial region, with only a growth of thermal fluctuations at the interface. Furthermore, a sample was prepared with an inhomogeneous layer by using a very low concentration of the solution when spin coating. Such a sample was pre-dewetted with holes acting as nucleation sites. It acts as a model of assessment of an unknown buried morphology and is described in 5.3.2.

The breakup of a single PS layer on Si substrate has already been extensively studied [23], [25], [26]. Starting with the original publication of Vrij [87], where a decomposition of thin liquid films is described, analogies were found between this description and that of viscoelastic liquids. A spinodal decomposition type of dewetting, called *spinodal dewetting*, has been hypothesized and observed [26], [88], [89], [90]. The observed wavelengths are far more broadly distributed in reality than those predicted by the Cahn-Hilliard

theory [27, 90, 91]. The observed peak of the fastest growing wavelengths is broadly distributed and has a maximum of only $\sim 5 - 10\%$ above the rest of the wavelengths [26].

The heterogeneous and spinodal nucleation processes are indistinguishable only in a single time scattering pattern. In a spinodal process, a narrow band of fluctuations will grow exponentially as a function of time, but only until the film rupture [32]. After that, the signal of dewetting will be indistinguishable, whether the layer broke up by heterogeneous or spinodal nucleation. It is therefore crucial that the whole process is observed, which poses some experimental challenges, as the films are very thin, but the growth time τ of the fastest growing wavelength λ_s grows with $\tau \sim h^5$ [24].

A buried polymer-polymer interface poses even further complication, as it is not accessible to any standard probes. The work done previously involved the use of neutron reflectometry, which, as already discussed, is a suitable tool for the study of buried soft interfaces. Latter work focused on bilayer and trilayer samples [92], [93], [94], but stopped short of a full analysis of the buried interface in the lateral direction. This could yield information on the existence of spinodal breakup [95] at polymer-polymer interfaces and furthermore elucidate the breakup mechanism in polymer thin systems, where the influence of substrate or the air could be mitigated by increasing or decreasing the distance to them.

5.2 Annealing of a system with thin capping layer

As will be demonstrated in this chapter, a breakup of an unstable bilayer of immiscible polymers, when capped with an insufficiently thick layer on a solid substrate, is a rather complex process. When the top h-PMMA layer is not thick enough, the top layer was observed to nucleate on its own. We have observed the kinetics of the process using specular reflectivity and off-specular neutron scattering. The OSS is capable of following the morphology changes during the process for each layer.

The sample was prepared using the technique previously described in sec. 4.2.2. The Si substrate was first cleaned with the 4-step procedure and subsequently spin coated with a d-PS ($M_w = 66\,\mathrm{kDa}$) of thickness $d_{\text{d-PS}} = 155\,\text{Å}$. A layer of h-PMMA ($M_w = 298\,\mathrm{kDa}$) was first spin coated on a glass slide, which had been cleaned with the same 4-step procedure, then floated on water and finally deposited on the Si / d-PS system. In order to speed up the kinetics, a d-PS layer with lower molecular weight was used than before. The annealing times therefore cannot be directly compared; however, one can rescale the times using polymer scaling laws [96]. The obtained times range from the beginning ($t = 0\,\mathrm{min}$), to beyond the state achieved before in chapter 4.

5.2.1 Specular reflectivity

The experiments were performed in ToF mode at the D17 reflectometer at ILL in Grenoble, France. The samples were annealed at $T = 160\,^{\circ}\mathrm{C}$, ex-situ in a vacuum oven, quenched at room temperature (well below T_g) and then measured in the glassy state.

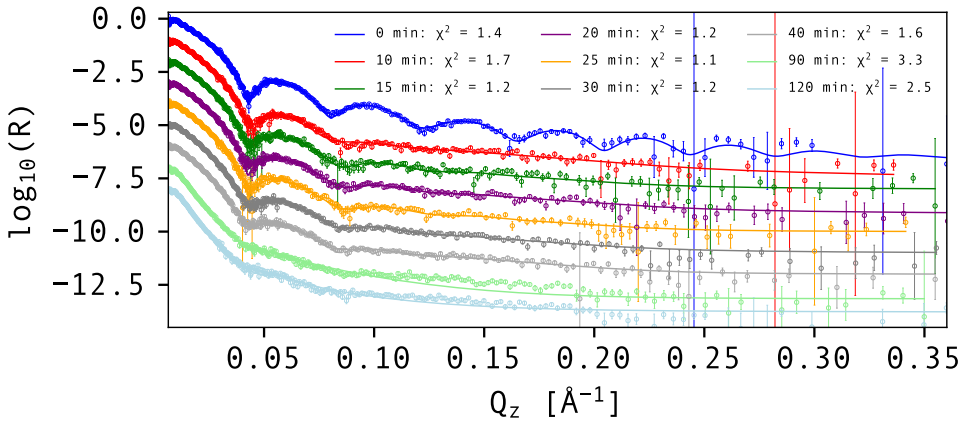

Figure 5.1: Reflectivity of the DW4 PS/PMMA bilayer sample with thin capping layer, profiles are shifted by a factor of 10 for clarity.

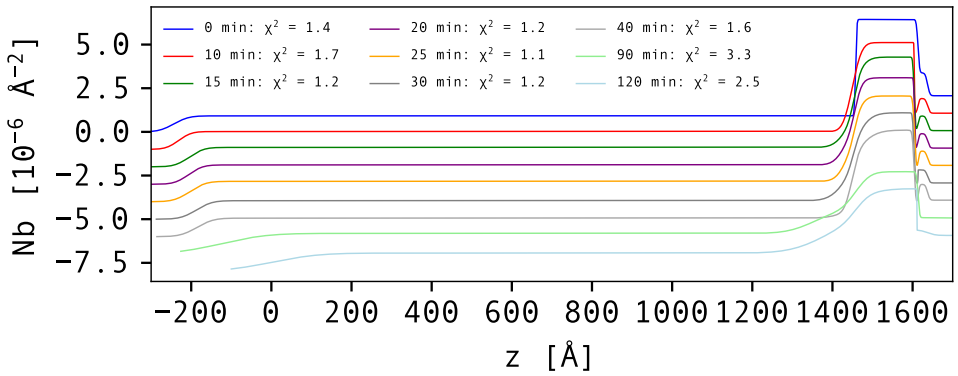

Figure 5.2: SLD of the DW4 PS/PMMA bilayer sample with thin capping layer, profiles are shifted by a factor of 10 for clarity.

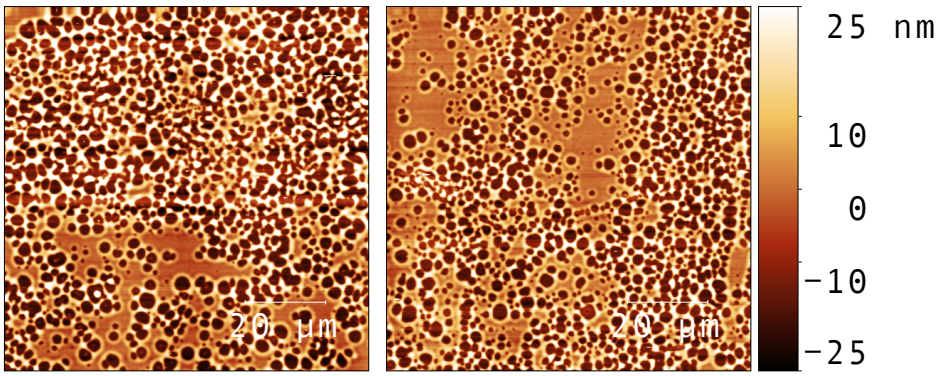

Figure 5.3: AFM pictures of the final state of the DW4 bilayer sample taken at two different positions.

Table 5.1: Fitted structural parameters for sample DW4 as a function of annealing time. Parameters without a fit error were fixed, due to otherwise non convergent fit. The errors are from the fit. The respective fits are shown in figures 5.1 and 5.2.

t_{ann} [min]	d_{dPS} [Å]	d_{hPMMA} [Å]	Nb_{hPMMA} [10^{-6} Å^{-2}]	Nb_{dPS} [10^{-6} Å^{-2}]
0	155 ± 1	1700 ± 3	0.91 ± 0.02	6.43 ± 0.03
10	154 ± 1	1680 ± 3	1.01 ± 0.02	6.11 ± 0.01
15	151 ± 1	1646 ± 3	1.11 ± 0.02	6.28 ± 0.03
20	149 ± 1	1643	1.10 ± 0.02	6.1
25	151 ± 51	1646 ± 4	1.16 ± 0.02	6.05 ± 0.03
30	153 ± 14	1629 ± 2	1.059	6.09 ± 0.02
40	155 ± 19	1632 ± 2	1.059	6.1
90	154 ± 2	1482 ± 28	1.18 ± 0.03	4.72 ± 0.03

Specular reflectivity was recorded under two different incoming angles, to increase the q_z range and maintain a good resolution.

The results were fitted with 2 different models. Initially, the layer can be very nicely fitted with the 3-layer model: h-PMMA / d-PS / SiO_2. The initial fit at $t = 0$ min shows the system as it is, after deposition. Many well-defined Kiessig fringes, coming from both the thin and thick layers, can be seen, showing a good homogeneity of the sample. The roughness between the layers is initially also very small, $\sigma \sim 5$ Å. Starting to anneal the sample, we can immediately see an increase in the roughness at the polymer-polymer interface, as the well-defined fringes start to disappear. Eventually, they are completely gone, signifying a complete rupture of the buried layer. After the second annealing step at $t = 15$ min, in order to maintain the quality of the fit, as before, a 4th layer must be introduced. It represents the extended interfacial region, which is a mixture between the d-PS and h-PMMA. This signifies the beginning of a breakup of the bottom layer and simultaneously the dewetting of the top layer. Since h-PMMA has a stronger dipolar interaction with the Si surface, the stable system would be the reversed Si / SiO_2 / PMMA / PS / air system. If the bottom layer has no time to irreversibly adsorb prior to the top layer deposition, both will tend to fulfill their lowest energy state. For all further steps until $t = 90$ min, the 4-layer model can be used and the mass conservation in the fits is strictly obeyed. However, after that step, the sample cannot be fitted well with such a model anymore. We consider it to be in a completely dewetted state, as the Kiessig fringes are completely gone and therefore cannot be fitted with a slab model anymore. The AFM pictures at two different positions on the surface are shown in figure 5.3.

All the structural parameters are presented in table 5.1, their corresponding reflectivity fits are shown in figure 5.1 and the SLD profiles in figure 5.2.

5.2.2 Off-specular scattering model and results

As already mentioned, the initial 2 fits are fitted with a 3-layer model, meaning that the only source of perturbation and thus contribution to the OSS is the growth of the holes in the top layer (not for the initial film) and the Gaussian roughness at the interface between the two polymers. The fits nicely follow the experimental data and due to the low intensity, a Gaussian roughness is a sufficient contribution to describe the spectrum. As we further anneal the system, the OSS grows and, just as in specular reflectivity, a 4-layer model is needed, with the majority of scattering intensity coming from the larger and larger scattering volume from the extended interfacial region. Furthermore, the holes in the top layer are growing and are the dominant contribution to the spectrum. The interference of the neutrons inside the layer is visible as parallel lines at constant $p_i - p_f$ in the $(p_i - p_f, p_i + p_f)$ space measurements, shown schematically in figure 5.4a. First is the black, specular line, broadened by the resolution. The green parallel lines at constant $p_i + p_f$ arise due to the interference between the top and bottom interface and have the same spacing as the Kiessig fringes coming from this layer in specular reflectivity. The parallel lines at constant $p_i - p_f$, marked with red, are caused by the interference of neutrons inside the top layer due to holes filled by air. This is a sign that the top layer is also dewetting. As can be seen in [97], such lines are not visible in stable bilayers, where only the constant $p_i + p_f$ lines are present. Both layers are stable and show no dewetting, but have correlated interfaces out-of-plane. The two effects are purely optical phenomena and do not carry any quantitative information beyond that already obtained by specular fits. In the calculations, they are carried by the wave field terms and not the form factor. Finally, the lines marked with blue are the various Yoneda peaks, the origin of which has already been described in eq. 2.50. The same features are marked for the $(\lambda, \theta_i + \theta_f)$ space in figure 5.4b, but due to the considerations mentioned in sec. 2.2, they do not appear as parallel lines.

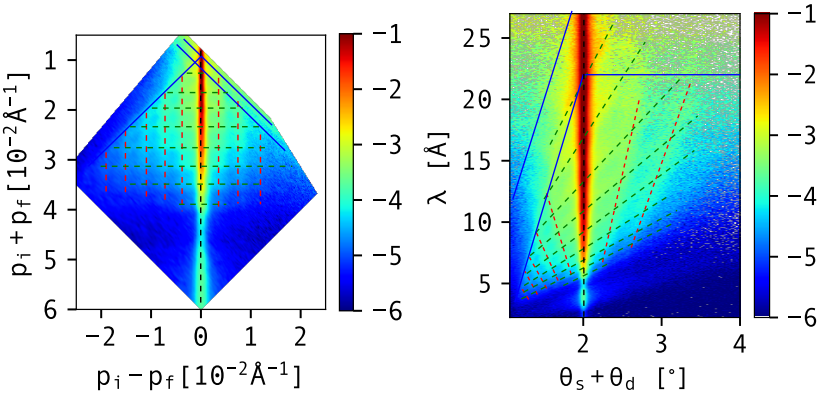

(a) (b)

Figure 5.4: Features in (a) $(p_i - p_f, p_i + p_f)$ and (b) $(\lambda, \theta_i + \theta_f)$ space. Green lines come from the interference between the bottom and the top interface and are spaced according to the thickness of the top layer. Red lines are caused by the interference of the neutrons, due to the holes present in the top layer. Their spacing is the same as for the green lines. Blue lines are Yoneda peaks of different materials, namely Si and h-PMMA. d-PS is not seen, as it is too thin in this example. The black line is the specular peak.

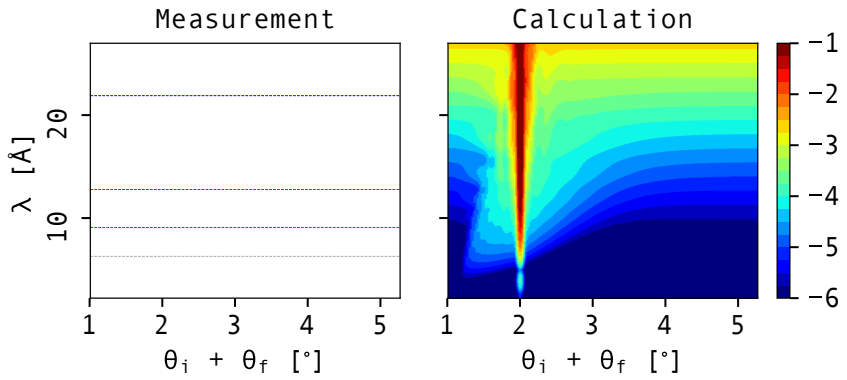

Figure 5.5: Measurement and DWBA calculation for $t = 10\,\text{min}$ annealed sample in the $(\theta_i + \theta_f, \lambda)$ space.

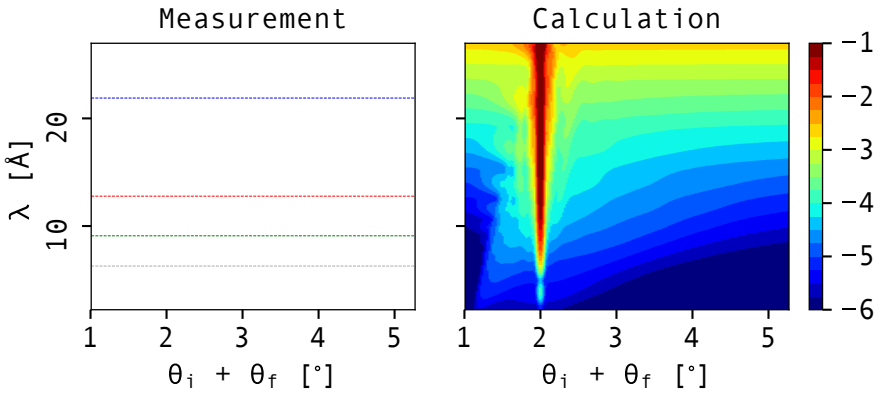

Figure 5.6: Measurement and DWBA calculation for $t = 15\,\text{min}$ annealed sample in the $(\theta_i + \theta_f, \lambda)$ space.

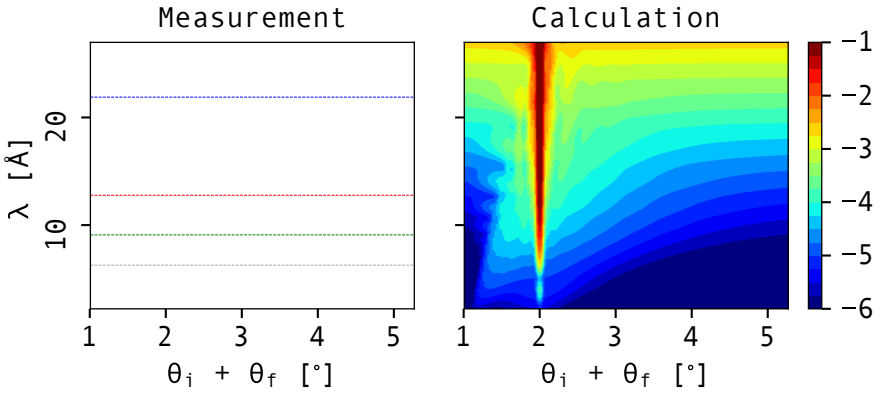

Figure 5.7: Measurement and DWBA calculation for $t = 20\,\text{min}$ annealed sample in the $(\theta_i + \theta_f, \lambda)$ space.

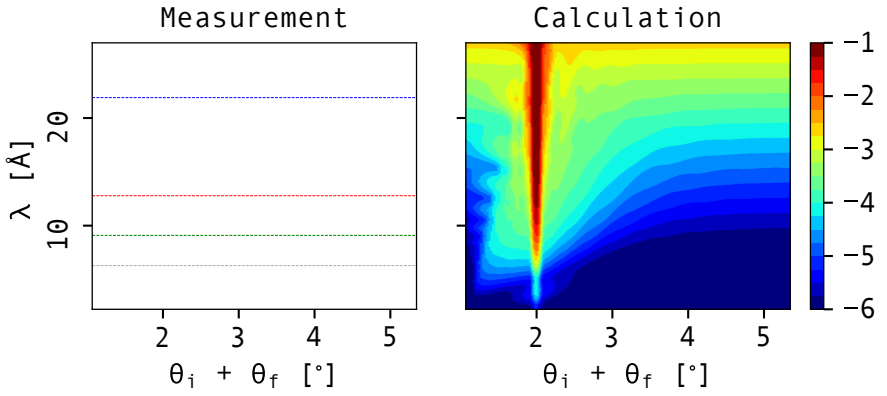

Figure 5.8: Measurement and DWBA calculation for $t = 40\,\text{min}$ annealed sample in the $(\theta_i + \theta_f, \lambda)$ space.

From such an experimental spectrum, we can see that there are a few distinct contributions to the scattering. Firstly, the top interface is modelled with holes in the top layer. Since a small concentration of holes (surface fraction $< 5\%$) would change the SLD in specular reflectivity only within the experimental error, the concentration c used for the fits is the first fitting parameter for OSS intensity. Secondly, in the first two annealing steps, the only other contribution is the Gaussian roughness at the interface between the h-PMMA and d-PS. In all the other annealing steps, an extended interfacial layer is used to fit the specular reflectivity and the perturbation in off-specular scattering is assumed to be coming from there. An overview of the OSS fit parameters is given in table 5.2.

Table 5.2: Parameters used in the model. All the SLDs are fitted in specular reflectivity. The only fitting parameters are the ones presented in the last column. In the first two annealing times ($t = 0\,\text{min}$, $t = 10\,\text{min}$), the 2nd, extended interfacial layer does not exist.

Layer	Material	ΔNb	Parameters
1	h-PMMA	$\overline{Nb}_1 - Nb_{\text{air}}$	c, ξ_1
2	d-PS/h-PMMA	$\overline{Nb}_2 - Nb_{\text{hPMMA}}$, $\overline{Nb}_2 - Nb_{\text{dPS}}$	ξ_2
3	d-PS	$\overline{Nb}_2 - \overline{Nb}_3$	ξ_3

Due to attractive short-range forces, h-PMMA tends to be in contact with the substrate and at the same time push d-PS to the top. As the process progresses, an SLD gradient appears through the h-PMMA layer. This happens due to the holes being wider at the top and thinner at the bottom, where they are in contact with the ridges of the underlying d-PS layer. Modelling uniform holes through the top layer and extending the d-PS / h-PMMA interface are therefore simplifications. It turns out that the approximations are very reasonable, as it is demonstrated in figures 5.5, 5.6, 5.7, 5.8 and 5.9. This analysis, combined with chapter 4, shows that the top layer in an Si / SiO_2 / PS / PMMA / air

bilayer is inherently unstable for sufficiently thin PMMA (and PS) films and that the breakup starts very early on in the process.

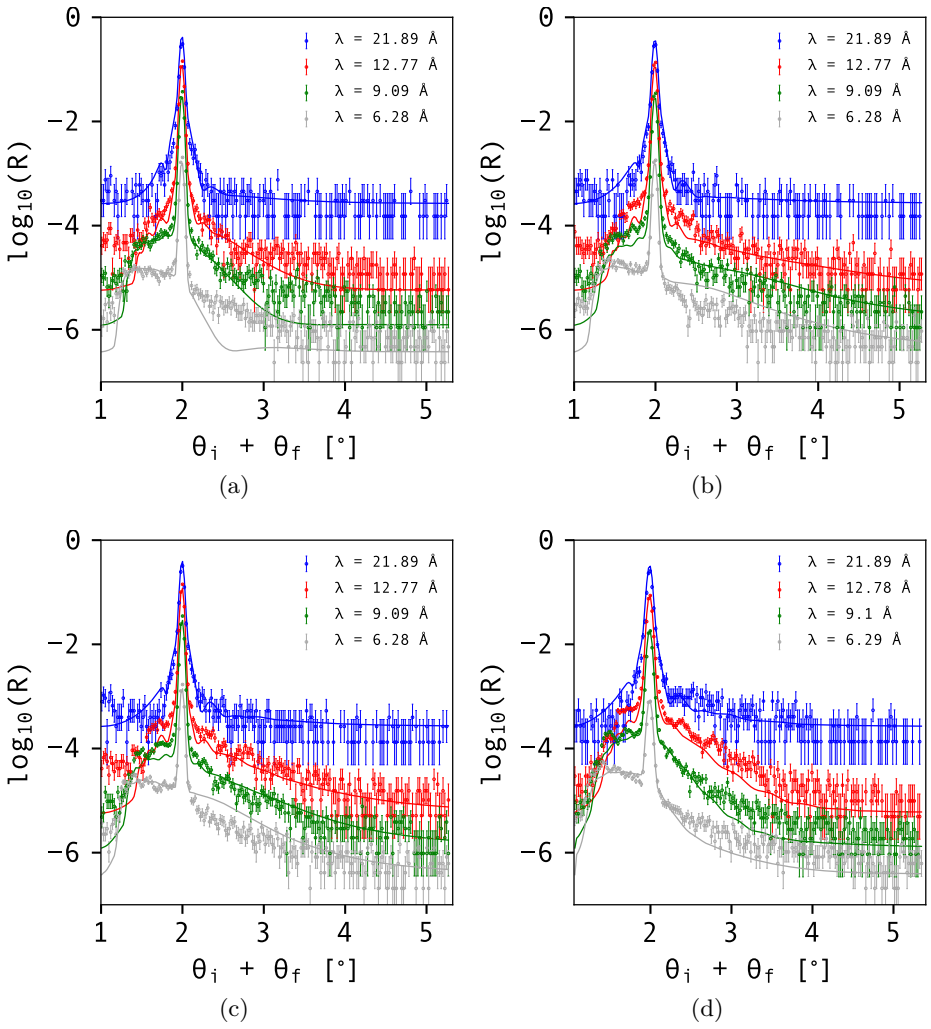

Figure 5.9: DW4 bilayer with thin PMMA capping layer. (a) $t = 10\,\text{min}$, (b) $t = 15\,\text{min}$, (b) $t = 20\,\text{min}$, (b) $t = 40\,\text{min}$. The different lines are fits to the data. Four wavelength cuts are shown.

5.3 Annealing of a system with thick capping layer

In order to further investigate the kinetics of destabilization of a buried polymer-polymer interface, a system of thin PS on an Si substrate with a thick PMMA capping layer was chosen. The thick PMMA capping layer isolates the van der Waals contribution of PMMA, as the influence of the interface with the free surface becomes negligible over

Table 5.3: List of samples with their structural properties, as deposited. The SLD indicates the nominal SLD, showing that the PMMA 3500 sample was not properly deposited to cover the whole wafer, with pre-existing holes.

Name	d_{dPS} [Å] $M_w = 60\,\mathrm{kDa}$	d_{hPMMA} [Å]	Remark
PMMA 3500	107	3627 ($M_w = 310\,\mathrm{kDa}$)	Incomplete dPS coverage
PMMA BI	115	2994 ($M_w = 230\,\mathrm{kDa}$)	

the large distance. In order to achieve contrast in scattering length density (SLD), the bottom layer was deuterated, with the top being protonated. We have managed to measure two samples of the same chemical composition, but slightly different thicknesses of the bottom and top layers. Their structural properties from the fits and names are shown in table 5.3.

Systems with very thick top capping layer were prepared to minimize the influence of the free interface on the underlying buried polymer-polymer interface. On the other hand, the sample called PMMA 3500 did not have a properly deposited lower layer, showing the initial SLD of $Nb_{\mathrm{dPS}} = 5.5 \times 10^{-6}\,\mathrm{Å}^{-2}$. The results of the measurements are still relevant, as they serve as a very interesting model system with a different topography of the buried interface. As described below, the model works very well and shows the capabilities of the algorithm in determining the unknown structure of buried systems.

Both systems were first measured as prepared and then annealed in 5 min steps at $T = 160\,^{\circ}\mathrm{C}$. Both times, specular reflectivity was measured and a dedicated off-specular measurement was performed. This ensures that the specular curves are of the best possible quality, since they are very important for the establishment of the ideal potential structure.

5.3.1 Initiated nucleation of a buried thin film

Let us first assess the case where the initially prepared film already had holes after the spin-coating process, meaning that the d-PS coverage was incomplete. This *failed* sample preparation is in fact a precursor to another process that we called initiated dewetting. In case of any perturbations causing gradients in the deposited film, the dewetting will immediately start from those sites and will proceed much faster than any other form of spontaneous dewetting. This gives us a unique opportunity to construct a hypothetical structural model for the buried layer and investigate it with our algorithm. The specular reflectivity in figure 5.10 clearly shows that the bottom d-PS layer has imperfections going through the layer and that the imperfections are rather well defined. As shown in figure 5.11, the d-PS SLD was measured as $Nb_{\mathrm{dPS}} = 5.5 \times 10^{-6}\,\mathrm{Å}^{-2}$, instead of the nominal $Nb_{\mathrm{dPS}} = 6.407 \times 10^{-6}\,\mathrm{Å}^{-2}$. Furthermore, the Kiessig fringes coming from the thin layer are very well defined for the initial measurement at $t = 0\,\mathrm{min}$ annealing, which is a very good indication that the layer is rather homogeneous in thickness, but with

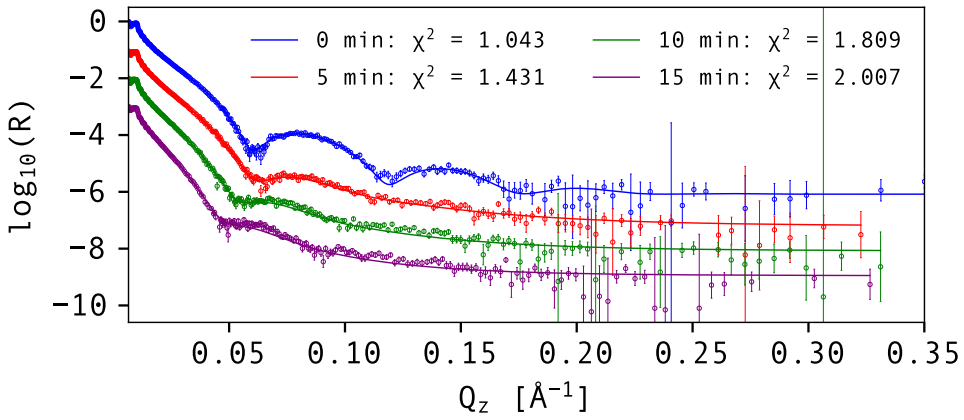

Figure 5.10: Reflectivity of the PMMA 3500 PS/PMMA bilayer sample with a thick capping layer.

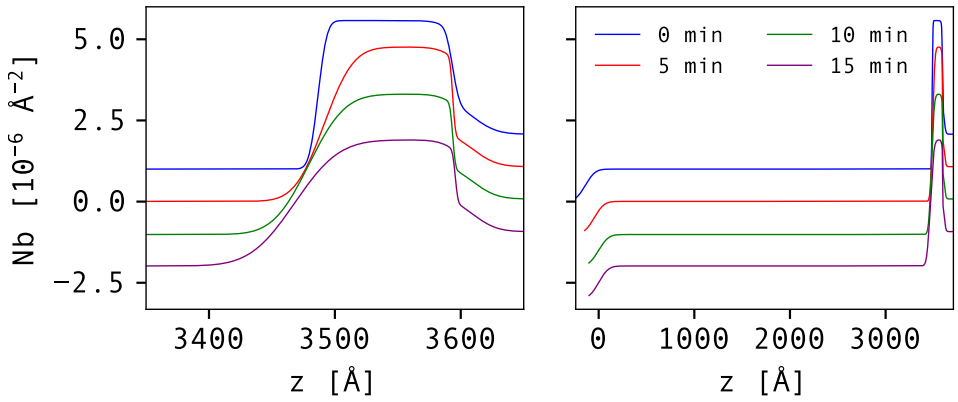

Figure 5.11: SLD of the PMMA 3500 PS/PMMA bilayer sample with a thick capping layer, profiles are shifted by a factor of 10 for clarity. (left) Zoom into interfacial region between the two polymers. (right) Whole SLD profile.

holes present. It is also not an incoherent sum of the regions without and with the layer, indicating that the holes are indeed much smaller than the lateral coherence length. This can happen when the concentration of the solution used in spin coating is too low. It is not possible to determine whether the holes are initially filled with h-PMMA, residual water molecules due to floating, or (most likely) air, as PS is hydrophobic and the SLDs are very close ($Nb_{\text{air}} = 0\,\text{Å}^{-2}$, $Nb_{\text{hPMMA}} = 1.059 \times 10^{-6}\,\text{Å}^{-2}$). Logically, we could assume the latter, as the top layer is prepared in a glassy state and floated onto the bottom dPS. Since air has a lower SLD, this explains the fact that we see an increase in SLD of the bottom layer in the first annealing step, as the top layer relaxes and the holes are filled by the polymer.

Annealing the sample further, an evolution of the breakup of the layer is nicely visible, both in the specular reflectivity data, shown in fig. 5.10, and its corresponding SLD

profiles, shown in fig. 5.11, where the interfacial width is also visibly increased between annealing times. The depth-dependent 1D density profile obtained by the specular reflectivity serves as a good indication of the process. However, for more direct observation of the process happening in the buried layer, the OSS offers additional information.

Looking now into off-specular scattering, one can see a clear evolution of the diffuse spectrum, both in $(\lambda, \theta_i + \theta_f)$ (fig. 5.14) and $(p_i - p_f, p_i + p_f)$ spaces (fig. A.15).

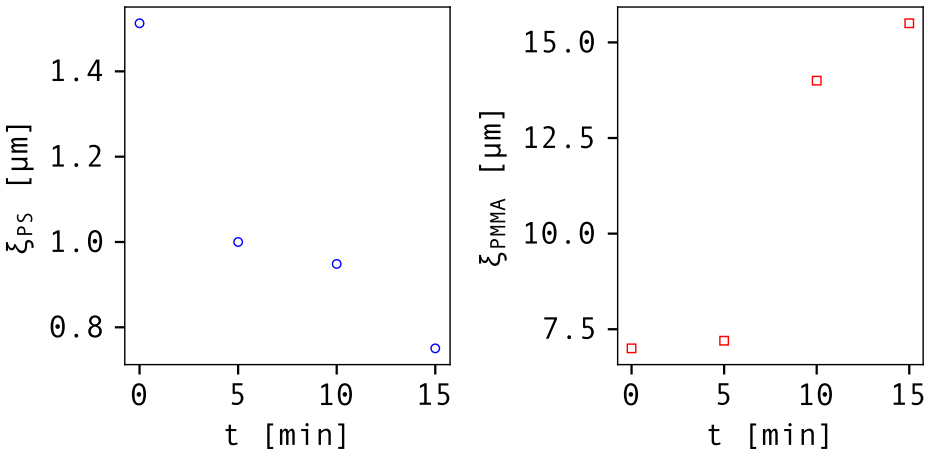

(a) (b)

Figure 5.12: (a) The ξ_{PS} is the average size of d-PS regions and is shrinking with time. (b) The ξ_{PMMA} is the average size of h-PMMA regions inside of the bottom layer, showing the growing average size of the holes.

Constructing the model, we assume that the bottom layer is composed out of two laterally separated compounds (which is a reasonable assumption, given that PS and PMMA are immiscible) with two independent correlation lengths ξ_{PMMA} and ξ_{PS}, where the first represents the average size of the holes and the second the average size of the PS droplets. The total contrast ΔNb in this layer is:

$$\Delta Nb = c|\overline{Nb} - Nb_{\mathrm{dPS}}|^2 + (1-c)|\overline{Nb} - Nb_{\mathrm{hPMMA}}|^2 - c(1-c)(\overline{Nb} - Nb_{\mathrm{dPS}})(\overline{Nb} - Nb_{\mathrm{hPMMA}})\,, \quad (5.1)$$

with c and $(1-c)$ being the d-PS and h-PMMA volume fractions in the layer, respectively, and $\overline{Nb}$ is the SLD read from the specular fit. This way, a minimum number of parameters is required: the correlation lengths of each of the phase. The concentration can be defined as:

$$c = \frac{\overline{Nb} - Nb_{\mathrm{hPMMA}}}{Nb_{\mathrm{dPS}} - Nb_{\mathrm{hPMMA}}}\,, \quad (5.2)$$

with $Nb_{\mathrm{dPS}} = 6.407 \times 10^{-6}\,\text{Å}^{-2}$ and $Nb_{\mathrm{hPMMA}} = 1.059 \times 10^{-6}\,\text{Å}^{-2}$ being the nominal SLDs. Each phase contribution has its own correlation length, so that the number of parameters is 2. In order to minimize the number of free parameters, the simplest assumption is made concerning the cross-term correlation length, namely the average between the dPS and hPMMS correlations: $\xi_{\mathrm{cross}} = \frac{\xi_{\mathrm{PMMA}}+\xi_{\mathrm{PS}}}{2}$. Estimating the initial c of d-PS in the layer:

$$c = \frac{5.5 \times 10^{-6}\,\text{Å}^{-2} - 1.059 \times 10^{-6}\,\text{Å}^{-2}}{6.407 \times 10^{-6}\,\text{Å}^{-2} - 1.059 \times 10^{-6}\,\text{Å}^{-2}} = 0.83\,, \tag{5.3}$$

it can be seen that the two phases, the d-PS and h-PMMA respectively, contribute almost equally, as the d-PS contrast with the mean SLD is lower than that of the h-PMMA. Examining now the fits of off-specular scattering shown in figure 5.13, it can be seen that the model very nicely reproduces the results. The trend of larger and larger holes, hypothesized before, is clearly visible in figure 5.12. At short annealing times, the size of the droplets is the dominant contribution. However, at $t_{\mathrm{ann}} = 15\,\mathrm{min}$, the scattering from the d-PS becomes very weak and loses the intensity of its features, appearing almost incoherent, and the prevailing contribution are the holes, which greatly increase in size.

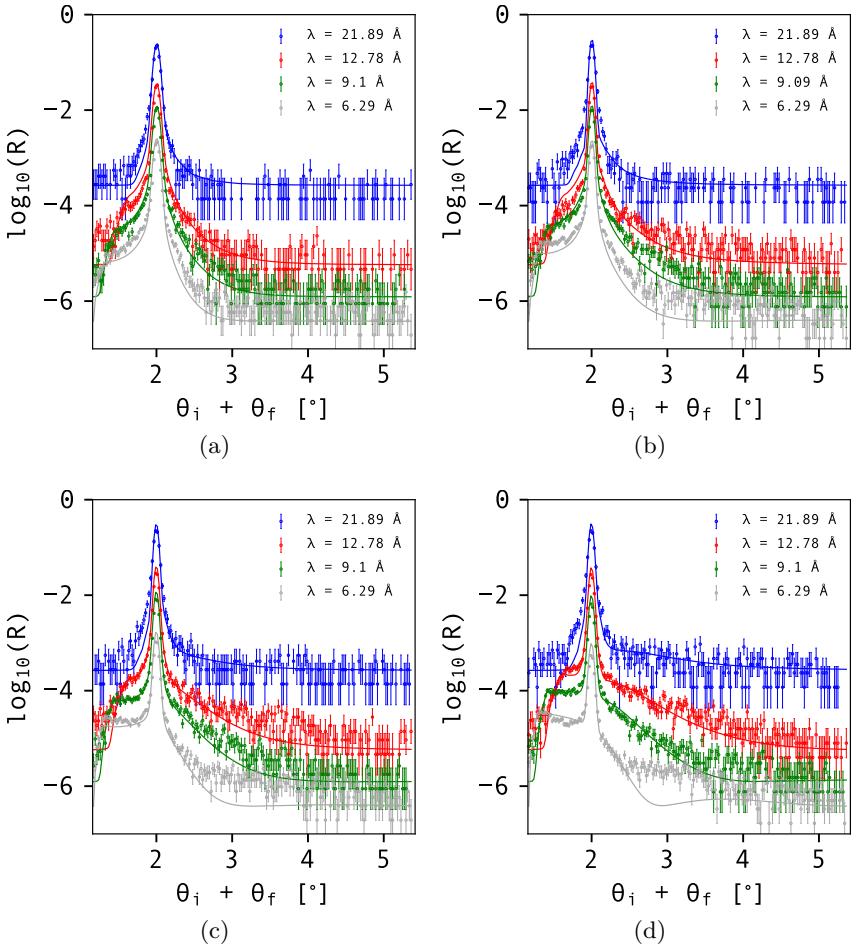

Figure 5.13: PMMA 3500. (a) $t = 0\,\text{min}$, (b) $t = 5\,\text{min}$, (c) $t = 10\,\text{min}$, (d) $t = 15\,\text{min}$.

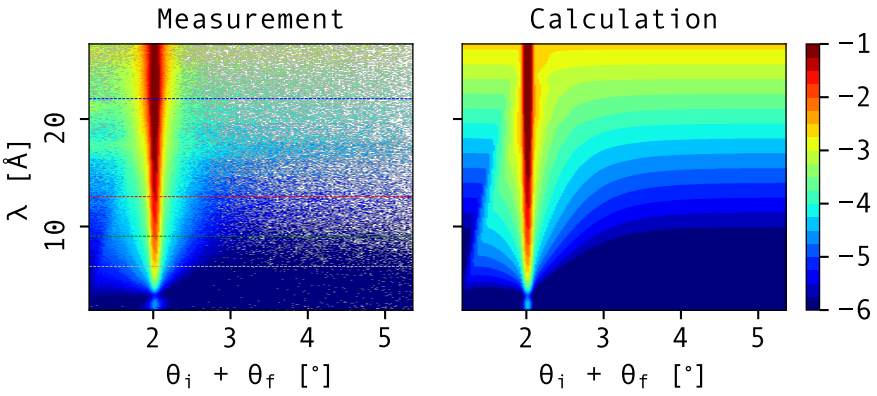

Figure 5.14: PMMA 3500 in $(\lambda, \theta_i + \theta_f)$ space, $t_{\text{annealing}} = 0\,\text{min}$.

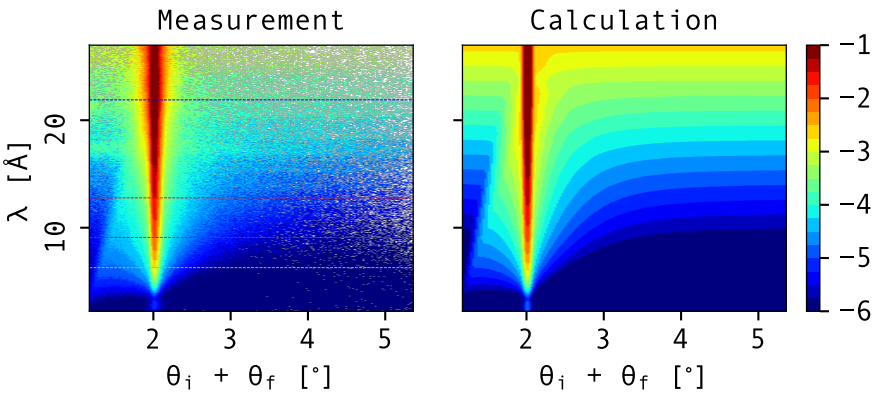

Figure 5.15: PMMA 3500 in $(\lambda, \theta_i + \theta_f)$ space, $t_{\text{annealing}} = 5\,\text{min}$.

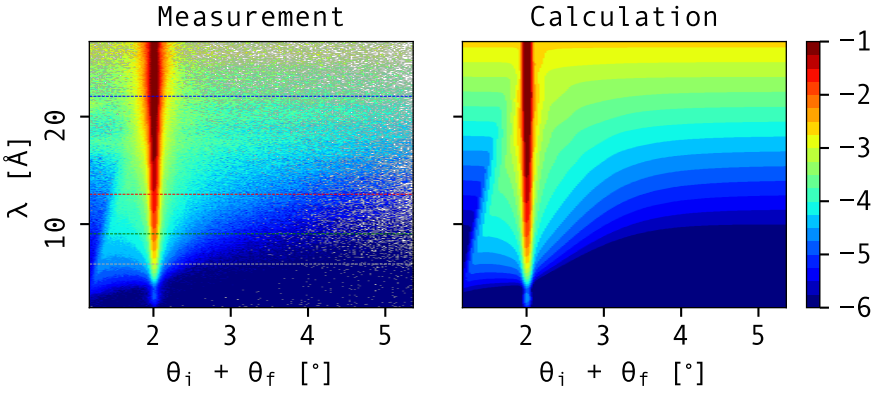

Figure 5.16: PMMA 3500 in $(\lambda, \theta_i + \theta_f)$ space, $t_{\text{annealing}} = 10\,\text{min}$.

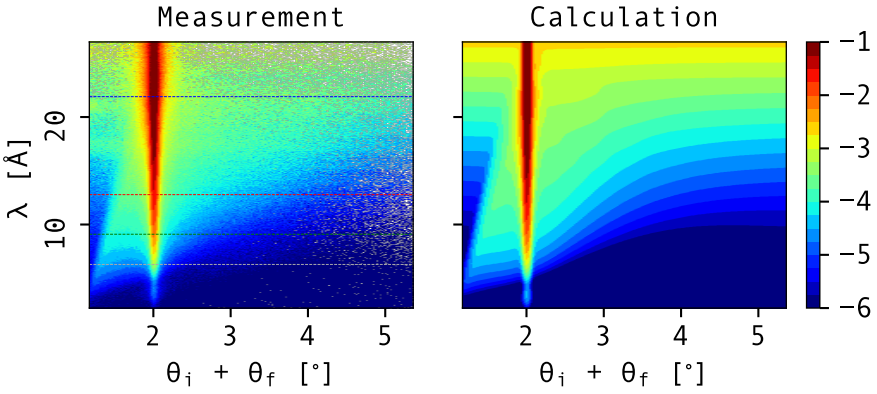

Figure 5.17: PMMA 3500 in $(\lambda, \theta_i + \theta_f)$ space, $t_{\text{annealing}} = 15\,\text{min}$.

5.3.2 Unstable system of thin and thick capping films

As was described before in chapter 4, the interplay between the short- and long- range forces can be adjusted by the thicknesses of different layers. As it was also demonstrated, the thickness of $d \sim 1200\,\text{Å}$ of the top capping layer is not enough to isolate the effect of the top free interface. The issue was addressed by preparing a sample with a very thick capping layer (sample PMMA Bi from table 5.3).

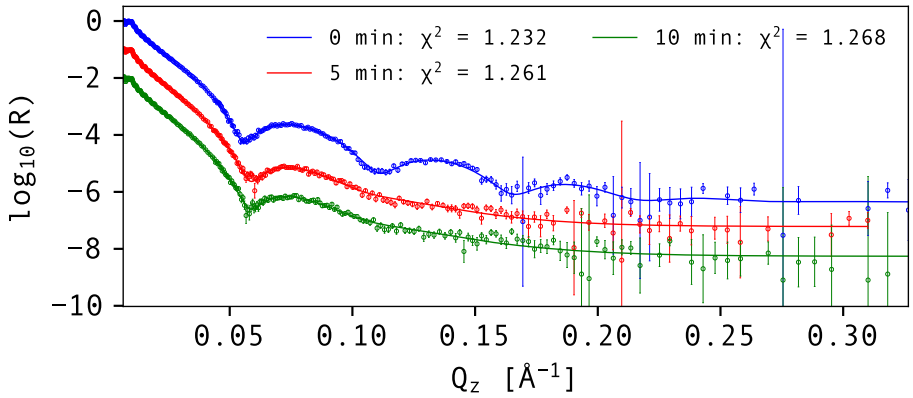

Figure 5.18: Reflectivity of the PMMA BI PS/PMMA bilayer sample with thick capping layer, profiles are shifted by a factor of 10 for clarity.

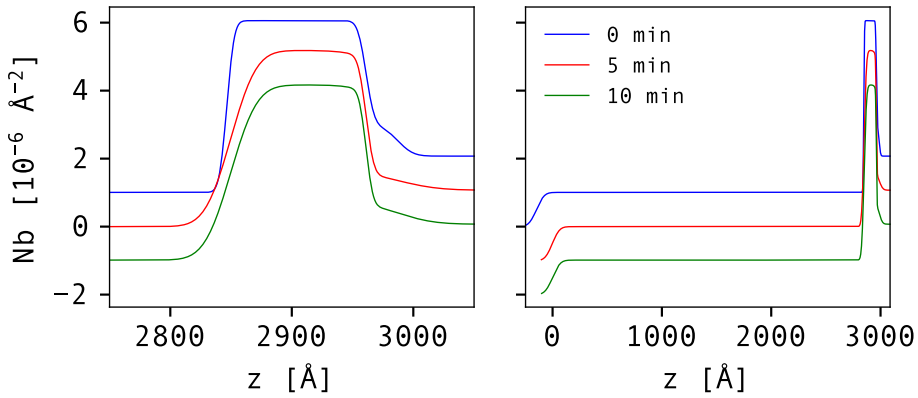

Figure 5.19: SLD of the PMMA BI PS/PMMA bilayer sample with thick capping layer, profiles are shifted by a factor of 10 for clarity. (left) Zoom into interfacial region between the two polymers. (right) Whole SLD profile.

The sample was prepared using the same procedure as PMMA 3500, by first spin coating a d-PS layer onto the Si and then floating the thick h-PMMA layer on top. Specular reflectivity shows that initially, its SLD is very close to the nominal SLD of d-PS. This means that the layer is uniform. This is also reflected in the behavior after annealing, as shown in figures 5.18 and 5.19. Initially, the Kiessig fringes, arising due to the bottom

Table 5.4: Fitted structural parameters for sample PMMA BI as a function of annealing time. $\sigma_{\mathrm{PS/PMMA}}$ is the Gaussian roughness between the d-PS and h-PMMA layers. The fits are shown in figures 5.18 and 5.19.

t_{ann} [min]	d_{dPS} [Å]	d_{hPMMA} [Å]	Nb_{hPMMA} [10^{-6} Å^{-2}]	Nb_{dPS} [10^{-6} Å^{-2}]	$\sigma_{\mathrm{PS/PMMA}}$ [Å]
0	114 ± 1	2994 ± 5	1.00 ± 0.09	6.05 ± 0.15	6.8 ± 0.1
5	111 ± 1	2852 ± 4	0.99 ± 0.09	6.17 ± 0.18	23.6 ± 0.2
10	111 ± 1	2849 ± 5	1.0 ± 0.1	6.17 ± 0.20	24.1 ± 0.3

thin d-PS layer, are nicely pronounced. After the first annealing step, no considerable d-PS SLD drop is observable, indicating that the layer is still homogeneous, while the roughness at the d-PS / h-PMMA interface increases. All the structural parameters of the sample are shown in table 5.4. This, combined with the stability of the top layer, shows that spinodal dewetting is a likely scenario of the buried layer breakup.

Such behavior of the observed SLD profile signifies that the layers are still homogeneous and only the thermal fluctuations at the interface are growing, pointing to either the film stability or an early stage of spinodal dewetting. In such case, one should not detect noticeable change in SLD of the layers, but only the increase in interfacial roughness [92]. Most importantly, there is no change in the h-PMMA layer, pointing to it being stable and therefore no holes forming from the top. As was shown before, nucleation (heterogeneous or homogeneous) leads to a change in SLD.

The OSS measurements back up the stability of the top layer, as no characteristic grid-like structure, such as the one in figure A.14, is seen. The measurements are shown in plots in $(p_i - p_f, p_i + p_f)$ space: A.19, A.20 and A.21. Rather than any regular structure appearing, there is a change in the diffuse spectrum. Such signal could be a sign of a breakup of the buried layer. At this stage, it is hard to assess whether spinodal dewetting will proceed faster than heterogeneous nucleation. However, an assessment of the fastest growing wavelength, the macroscopic spinodal length, can be done. As the stability condition of the dewetting mechanism depends on the effective interfacial potential, we can first define the potential and then its second derivative, which will be used in the calculation of the spinodal length λ_s. The potential consists of a short-range term, proportional to h^{-8}, and the van der Waals terms, proportional to h^{-2} [98]:

$$\phi(h) = \frac{C}{h^8} - \frac{A_{123}}{12\pi h^2} - \frac{A_{1234}}{12\pi(h+d)^2}\,, \tag{5.4}$$

where $C = 5.1 \times 10^{-77}\,\mathrm{J\,m^6} = 5.1 \times 10^{-17}\,\mathrm{J\,Å^6}$ is the interaction constant with the substrate, A_{123} is the Hamaker constant of Si / PS / Air, A_{1234} the Hamaker constant of Si / PS / PMMA / Air, h is the thickness of PS and d of PMMA. The second derivative of the potential is then equal to:

$$\phi''(h) = \frac{72C}{h^{10}} - \frac{A_{123}}{2\pi h^4} - \frac{A_{1234}}{2\pi(h+d)^4}\,. \tag{5.5}$$

The macroscopic spinodal length is then defined as [24]:

$$\lambda_s(h) = \sqrt{-\frac{8\pi^2\gamma}{\phi''(h)}}\,. \tag{5.6}$$

By taking the Hamaker constants calculated by [93], for films between thicknesses from 100 Å to 180 Å, one obtains length from $\lambda_s(100\,\text{Å}) \sim 300\,\text{nm}$ to $\lambda_s(180\,\text{Å}) \sim 1\,\mu\text{m}$, clearly much larger than the correlation lengths found experimentally for the thin capping layer (see fig. 4.11a, left). However, there is quite a wide discrepancy between Hamaker constant estimations and measurements [37, 68, 93, 98]. As the $\phi''(h)$ is a second derivative of the reconstructed effective potential, the value of the Hamaker constant is crucial for determination of the macroscopic spinodal length. By using the following values of Hamaker constants [93]:

$$A_{\text{Si/PS/PMMA}} = 3.2 \times 10^{-20}\,\text{J}\,,$$
$$A_{\text{Si/PS/PMMA/air}} = -3.7 \times 10^{-19}\,\text{J}\,,$$

we can calculate the spinodal length for a 114 Å-thin d-PS film, capped with 2994 Å-thick h-PMMA, as being equal to $\lambda_s(114\,\text{Å}) = 3975\,\text{Å} = 0.3975\,\mu\text{m}$. The correlation length extracted from the measurement for different annealing times is shown in figure 5.20d and is extracted from fits shown in figure 5.20. All the off-specular measurements with their corresponding fits are shown in figures 5.21, 5.22 and 5.23. Despite the experimentally determined correlation length being too high at current annealing times, there is a tendency of the system to reduce its length with increasing annealing time. Furthermore, the time for the fastest growing instable mode grows with film thickness as $\tau \propto h^5$ [94].

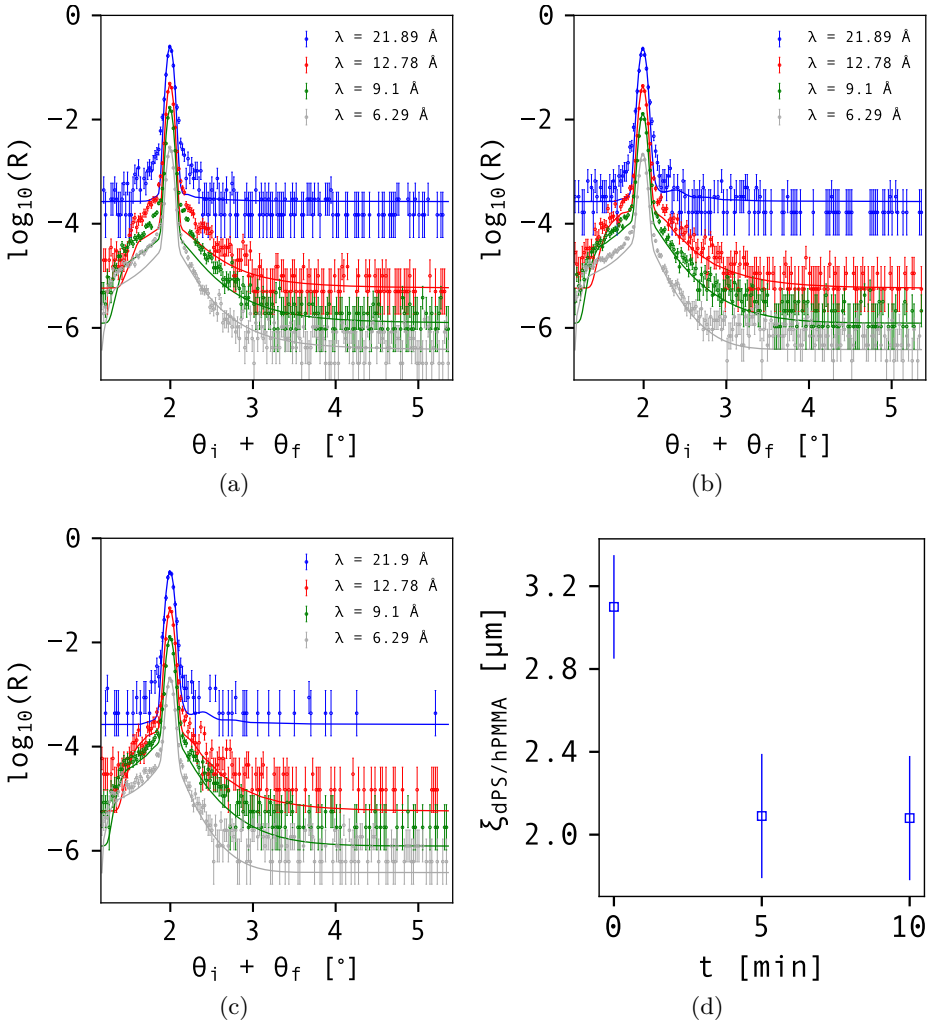

Figure 5.20: PMMA BI (a) $t = 0\,\text{min}$, (b) $t = 5\,\text{min}$, (c) $t = 10\,\text{min}$ and the evolution of the in-plane correlation length xi at the interface between d-PS and h-PMMA.

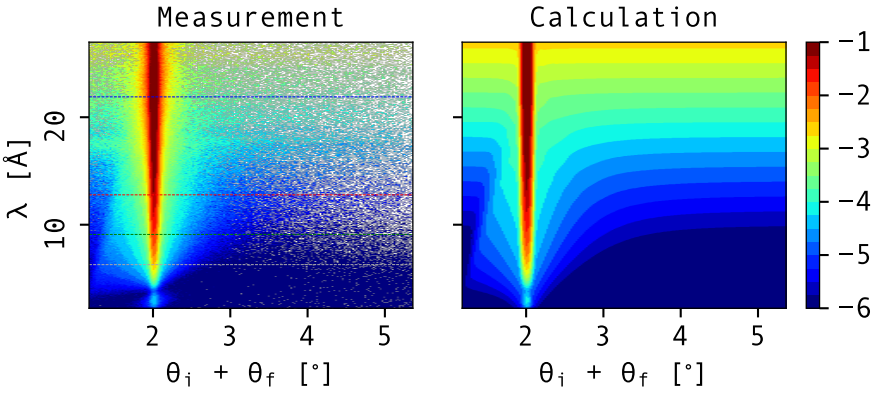

Figure 5.21: PMMA BI in $(\lambda, \theta_i + \theta_f)$ space, $t_{\text{annealing}} = 0\,\text{min}$.

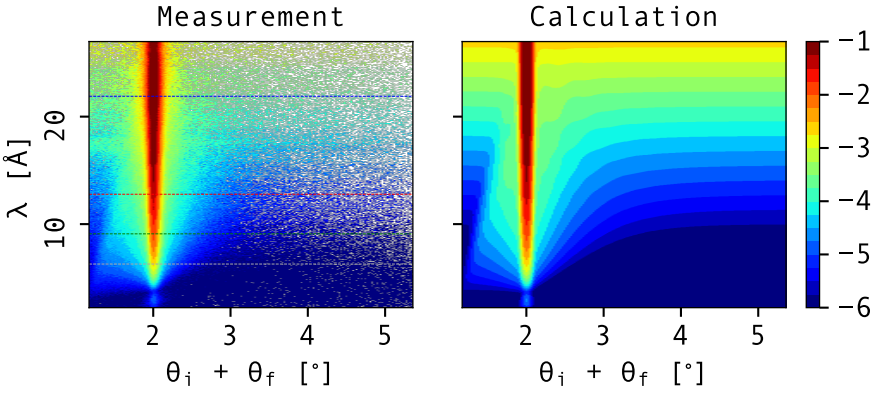

Figure 5.22: PMMA BI in $(\lambda, \theta_i + \theta_f)$ space, $t_{\text{annealing}} = 5\,\text{min}$.

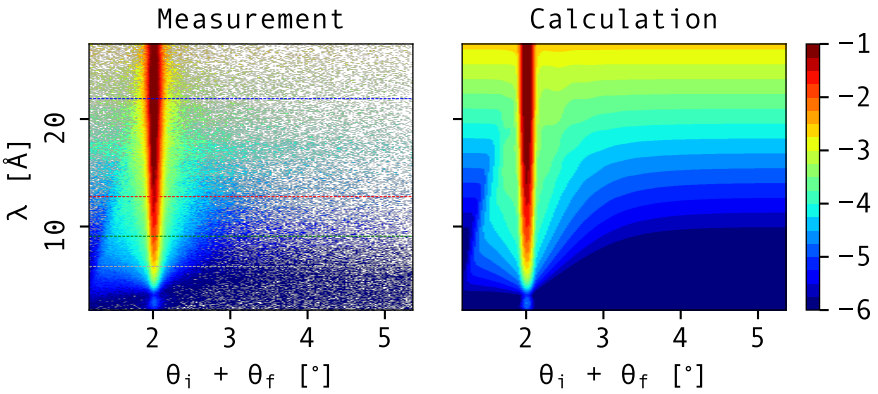

Figure 5.23: PMMA BI in $(\lambda, \theta_i + \theta_f)$ space, $t_{\text{annealing}} = 10\,\text{min}$.

5.4 Three layer system and beyond

As shown on various different examples throughout this chapter, the off-specular scattering offers a unique way for qualitative and quantitative investigations of buried interfaces. Building on this, the bilayer system can be further extended by including another layer. This gives an insight into the simultaneous behavior of two buried polymer - polymer interfaces instead of one. A three-layer system of thick-thin-thick layers on Si substrate was prepared, where the influence of the substrate on the two interfaces of the thin layer is reduced to a negligible level. This kind of system also permits access to two polymer-polymer interfaces dewetting simultaneously.

The system of Si / h-PS ($M_w = 630\,\mathrm{kDa}$) / d-PMMA ($M_w = 53\,\mathrm{kDa}$) / h-PS ($M_w = 630\,\mathrm{kDa}$) / air was prepared by first spin coating the bottom layer onto the Si substrate, then spin coating a solution of PMMA in acetic acid onto the h-PS. Such molecular weights were chosen that the viscosity of the two polymers was as close as possible [94]. Finally, a thick top layer was first spin coated from the same solution as the bottom layer onto a glass slide and then floated on top of the bilayer.

Table 5.5: Fitted structural parameters for trilayer sample s99 as a function of annealing time. The fits are shown in figures 5.25 and 5.26.

t_{ann} [min]	$\sigma_{\mathrm{hPS/dPMMA}}$ [Å]	$\sigma_{\mathrm{dPMMA/hPS}}$ [Å]	Nb_{dPMMA} [$10^{-6}\,\mathrm{Å}^{-2}$]	$Nb_{\mathrm{top\ hPS}}$ [$10^{-6}\,\mathrm{Å}^{-2}$]
0	9.4 ± 0.1	2.3 ± 0.5	6.8 ± 0.1	1.39 ± 0.02
10	15.1 ± 0.2	15.9 ± 0.5	6.8 ± 0.2	1.39 ± 0.05
17	15.4 ± 0.3	17.6 ± 0.4	6.7 ± 0.2	1.37 ± 0.03
25	16.9 ± 0.2	15.6 ± 0.3	6.7 ± 0.3	1.37 ± 0.02
30	16.9 ± 0.3	16.2 ± 0.4	6.7 ± 0.3	1.37 ± 0.03
35	18.8 ± 0.5	16.7 ± 0.1	6.7 ± 0.1	1.36 ± 0.01
50	18.0 ± 0.5	18.9 ± 0.2	6.4 ± 0.3	1.36 ± 0.02
80	20.4 ± 0.2	27.5 ± 0.5	5.5 ± 0.2	1.1 ± 0.1
110	28.0 ± 0.8	34.9 ± 0.5	4.9 ± 0.2	1.2 ± 0.4

As shown in figure 5.25, the specular reflectivity shows an increase in roughness at both the top PS / PMMA and bottom PMMA / PS interface. This is consistent with previous measurements where the PMMA layer is in contact with the PS of the same molecular weight on both sides [94]. As the evolution of the SLD in figure 5.26 shows, the mean SLD of the middle layer is stable up to the annealing time around $t = 35\,\mathrm{min}$. The top layer's SLD starts to noticeably fall as well around that time and its roughness (h-PS / air) is growing very fast. All the parameters of the fits are shown in table 5.5. However, the specular reflectivity only offers a limited view into the processes involved both at the interfaces and in the layers, as only the mean SLD projection on the perpendicular

axis is recorded.

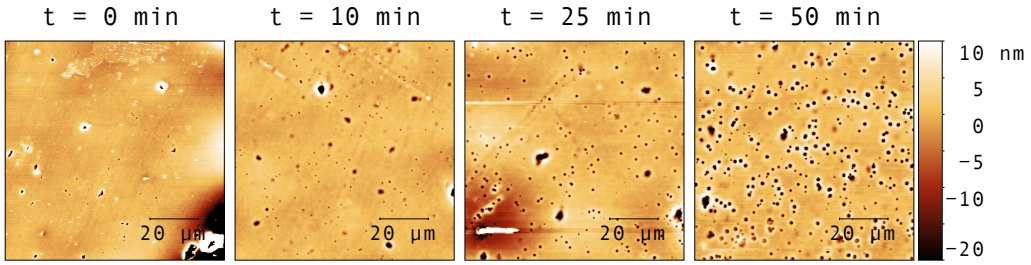

Figure 5.24: Evolution of the top surface of the trilayer s99, observed under the AFM. The appearance of holes is clearly visible.

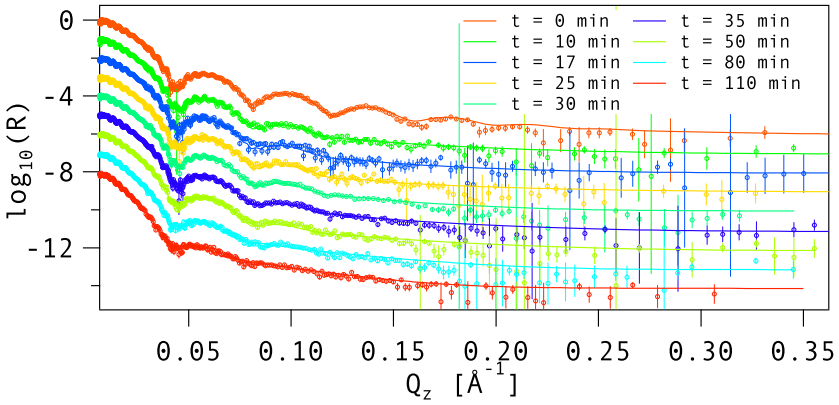

Figure 5.25: Reflectivity of the Si/PS/PMMA/PS/air trilayer sample. Profiles are shifted by a factor of 10 for clarity.

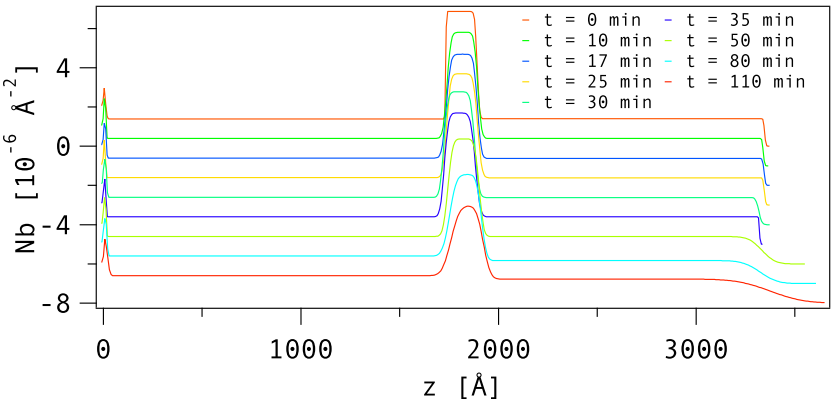

Figure 5.26: SLD of the Si/PS/PMMA/PS/air trilayer sample. Profiles are shifted by a factor of 10^{-6} for clarity.

The top surface topography was monitored with AFM and is shown for different annealing times in figure 5.24. The surface coverage of holes is steadily increasing as a function of time, despite the initial film being perfectly homogeneous. At the same time, the roughness in areas not affected by the holes remains fairly constant. The averaged line-by-line power spectral density of such an AFM image is in fact very close to what is measured by OSS from the top surface. The shape of the neutron beam on D17 is a rectangle of 3 cm × 1 cm and its coherence rectangle, due to the slit setting being very narrow in one direction and wide in another, is 50 µm × 100 nm [55]. This corresponds to the size of aforementioned AFM images very nicely, as the pixel size is ∼ 100 nm and the total width of the scan is 50 µm. A perturbation is therefore introduced through the top layer, with $\Delta Nb = \overline{Nb}_1 - Nb_{\text{air}}$. Then, further two contributions to the off-specular scattering are introduced at both d-PMMA interfaces. Off-specular measurements were recorded for the whole annealing series and an overview of the measurements is shown in figure 5.29. Due to the appearance of the stripes, caused by the dewetting in the top layer, a similar model was used to fit the data as before. Whether the interfaces oscillate in-phase or in anti-phase can now be verified by setting one of the roughnesses negative. This causes the correlator term from eq. 3.21 to become negative when calculating the cross-terms and their anti-phase contribution, changing the result slightly. The preliminary fits for $t = 25$ min are shown in figure 5.27.
In figure 5.28, a hypothetical situation is calculated for scattering from the interfaces below and above the thin layer, whether they oscillate in-phase or in anti-phase. The difference is very small and barely detectable for the trilayer. The multilayer, presented on the left (fig. 5.28) is a 3-times repetition of the trilayer and contains 3 dewetting thin layers. It can be seen that by adding three times the scattering volume of a trilayer, the intensity is clearly increased. Adding additional thin layers with high SLD also adds to the complexity of the potential and gives rise to more pronounced out-of-plane interference. Although the qualitative result is unchanged, the maxima and minima are almost at the same positions, the absolute intensity is changed. This shows the prediction capabilities of the OSS calculation routines and can help in designing suitable experiments in the future.

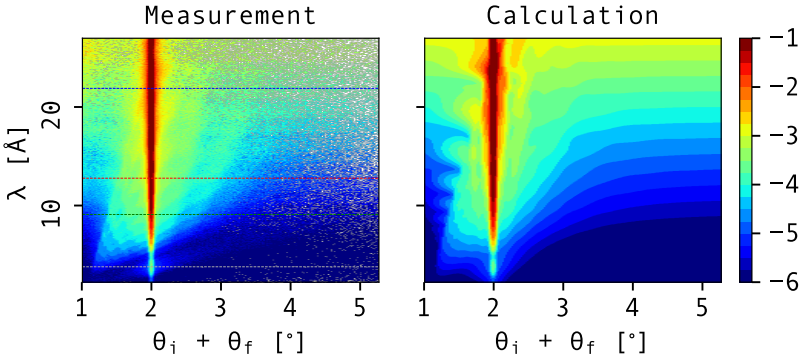

Figure 5.27: DWBA calculations compared to the measurements for s99 trilayer sample at $t = 25$ min annealing.

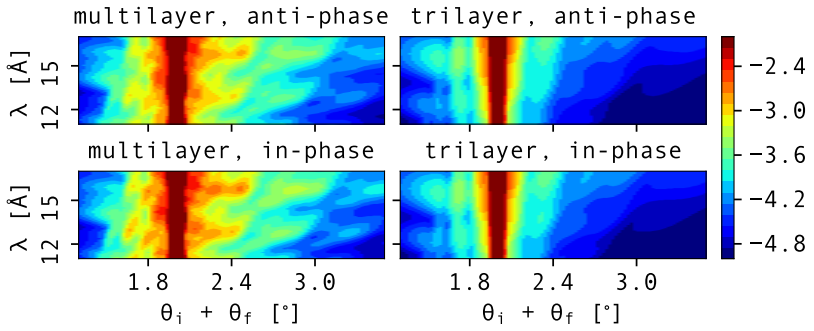

Figure 5.28: DWBA calculations for in-phase and anti-phase oscillations of the buried interfaces, showing the difference for the (left) multilayer and (right) trilayer. The difference in trilayer case is negligible.

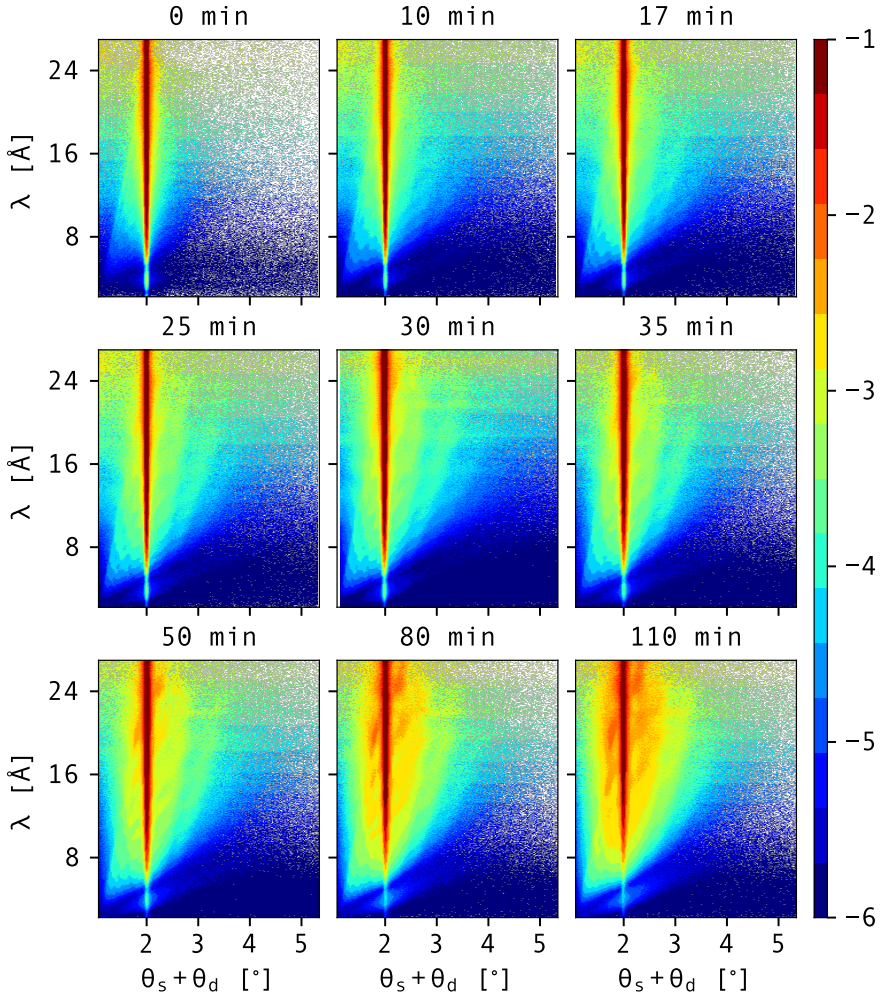

Figure 5.29: All the 2D measurements of the PS/PMMA/PS trilayer sample in the $(\theta_i + \theta_f, \lambda)$ space.

5.5 Outlook

A series of polymer bilayers and trilayers was measured by specular reflectivity and off-specular scattering in order to further study the behavior of the stability and instability in compound systems. It turns out that an insufficiently thick top layer tends to dewet spontaneously via heterogeneous nucleation. The nucleation could be induced by the layer preparation or the dewetting of the underlying thin layer as first, an increase in roughness at the interface is visible, and further on, bottom film rupture is imminent. However, for a sufficiently thick top layer, stability is reached despite the breakup of an underlying thin layer. This behavior is expected, as a very thick layer should not be susceptible to any influence of the substrate or layers below.

A further study could be made by varying the top layer roughness at a few different bottom layer thicknesses, simultaneously measured by the AFM and combined neutron reflectivity and off-specular scattering. This way, the morphology of the top layer could be fixed from the AFM data and then the underlying morphology of a number of buried interfaces could be resolved much better. Due to the majority of off-specular scattering coming from such a very thick dewetting layer, it is very hard to determine unknown buried morphology, as it is sitting on top of a dominating signal which is irrelevant for the desired information.

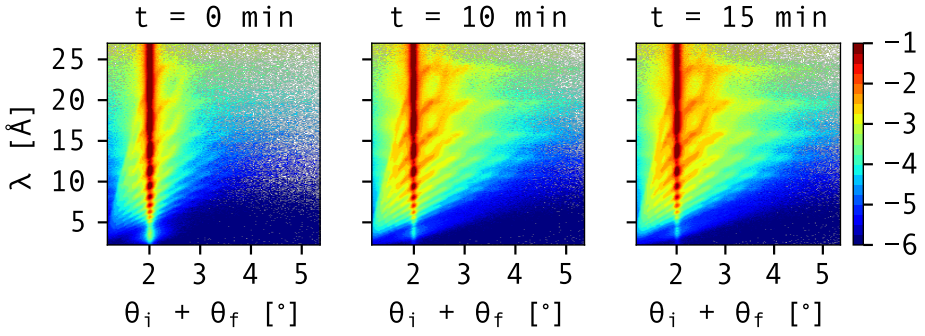

Figure 5.30: Off-specular scattering evolution of an Si / h-PS / d-PMMA / h-PS / d-PMMA / h-PS / d-PMMA / h-PS / air multilayer. The thickness of the h-PS (M_w = 526 kDa) layers is 1350 Å and 150 Å for the d-PMMA (M_w = 264 kDa).

We have addressed the problem of low signal by preparing a multilayer of 6 dewetting interfaces, namely Si / h-PS / d-PMMA / h-PS / d-PMMA / h-PS / d-PMMA / h-PS / air. The thickness of the h-PS (M_w = 526 kDa) layers is 1350 Å and 150 Å for the d-PMMA (M_w = 264 kDa). The enhanced signal coming from the interfaces should yield a higher signal. This is qualitatively visible in figure 5.30. However, there are too many interfaces and thus free parameters to achieve a sufficiently reasonable fit for specular reflectivity at this stage. A solution could be to measure the system with X-ray reflectivity and then simultaneously fit both X-ray and neutron data. A simulation based on a preliminary fit shown in figure 5.28 shows a noticeable difference between the in-

phase and anti-phase oscillations of the interfaces of the thin layers in the multilayer. A comparison between the data and the simulations is shown in figure 5.31. The combined effect, coming from 3 dewetting layers, increases the scattering volume substantially. The development of the off-specular scattering algorithm certainly offers new possibilities for investigation of a variety of systems. As it was shown, it is not only the features' position, but rather the absolute intensity which is equally important in detecting tiny differences in scattering coming from non-periodic structures.

This study illustrated the complexity of the possible effects taking place in our thin films (nucleation on the surface, increase of the roughness at the buried interfaces, dewetting of the buried thin film) and the capability of the OSS, combined with neutron reflectivity, to investigate these effects.

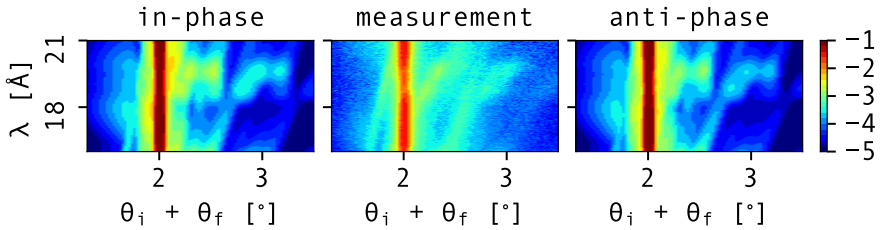

Figure 5.31: Comparison of in-phase and anti-phase interfacial shape calculations with the measurements for the multilayer sample.

6 Conclusion and outlook

6.1 Conclusion

The full reflectometry, a combination of specular reflectivity and off-specular scattering, is a technique which yields quantitative information of the 3D structure of the buried interfaces. However, due to its nature, the technique can only be exploited to its full potential by using an advanced analysis workflow, consisting of robust data reduction and manipulation routines, and advanced analysis methods. The tools that have been developed and are presented in this thesis, have been further backed by experimental validation on model thin polymer systems. The following was achieved and thoroughly described in the thesis:

- Implementation and experimental verification of a specular reflectivity Parratt's recursive algorithm, allowing for a robust calculation of amplitudes of upward and downward moving neutrons inside the sample. This is particularly important in soft matter, as the SLD structure (due to deuteration) often has interchanging high and low SLD layers, which causes numerical instability if using common implementations of the algorithm found in literature.
- Derivation and verification of off-specular differential scattering cross-section, including low roughness approximation and perturbation located throughout the layer. Implementation of the findings in a multilayer calculation algorithm with as little free parameters as possible, similar to specular reflectivity.
- Scaling of specular reflectivity to off-specular scattering for time-of-flight instruments, enabling both the calculation of off-specular scattering intensity in absolute units and simultaneous fitting of specular and off-specular parts. This gives the ability to not only analyze, but also predict scattering patterns and the location and intensity of expected features in advance.
- Verification of the above-mentioned algorithms on various model soft matter systems: Si/PS/PMMA bilayer samples, Si/PS/PMMA/PS trilayer samples, PS/PMMA/PS multilayers on Si substrates.
- Using off-specular scattering, we were able to show that preannealing has a noticeable influence on the overlying polymer-polymer interface and that the lateral in-plane correlation length is different for preannealed and non-preannealed systems. Furthermore, it was demonstrated that by combining specular and off-specular measurements, one not only obtains additional information about the

lateral properties, but is more constrained in specular fits as well. The predicted cutoff lengths for capillary waves were obtained for the two thinnest preannealed d-PS layers.

- Investigation of Si/PS/PMMA bilayer system in our case showed the presence of holes in PMMA capping layers, independent of thickness of underlying PS layer. The process was observed from its initiation and shows the simultaneous formation of holes in the top layer and increasing roughness with annealing time in the bottom PS layer which is higher than that of stable system. The two effects strongly influence the OSS scattering pattern and were identified by detailed study of the off-specular behavior.
- A system of a thin PMMA layer sandwiched between two thick identical PS layers has been investigated. The question whether the roughness of the two interfaces of the thin layer oscillates in-phase or in anti-phase was addressed by the use of reflectometry. As shown in simulations, the change in the polymer trilayer between the two cases is very small and hardly detectable. However, this was addressed by preparing a multilayer of 3 identical thin dewetting layers. It was shown through the simulations that such increased scattering volume can yield an increase of the OSS intensity.

6.2 Outlook and discussion

As shown, the off-specular scattering is a powerful tool for investigation of various buried interfaces that show correlated lateral features. Moreover, features of length scales spanning several orders of magnitude (from $\sim$ Å to $\sim 10\,\mu m$) can be observed simultaneously using neutron reflectivity and OSS. Combined with the neutron properties, which are favorable for soft matter research, this makes it a unique tool for in-situ non-destructive investigations. However, besides the low neutron flux and 2D detectors, the lack of suitable analysis tools has significantly held the usage back for more complex systems. By making off-specular analysis more available, the space for misinterpreting the results narrows down significantly. The work presented here is one of the few recent developments in this field. It is easily implementable in a modern programming language (here in Python), making off-specular analysis more straightforward. Furthermore, it has been shown to work on various different buried morphologies with or without much prior knowledge of the buried features.

Firstly, the routines that were developed for transformation between different representations of reciprocal space allow for qualitative inspection of the data. Features dependent on the structure appear parallel in (q_x, q_z) space, as the form factor is a function of the lateral wavevector q_x. In non-periodic or non-regular structures, an exponential decay of the correlation function in real space has been shown as a very good approximation to experimental results. Features dependent on the interference of neutrons inside the sample, arising from the complex SLD structure, which is very common in soft matter (e.g. interchanging high and low SLD), are parallel in $(p_i - p_f, p_i + p_f)$ space. Depending on that, a correct fitting procedure can be selected, either at constant q_x or $p_i - p_f$. The

calculation is done in the experimental $(\lambda, \theta_i + \theta_f)$ space, due to the minimum amount of convolution steps being involved to properly implement resolution. After that, the modular design of the algorithm allows one to simulate hypothetical scenarios, such as the one presented in section 5.4. This way one of the traps of off-specular scattering, namely the wrong assignment of features and their interpretation, is avoided. In case of insufficient signal, one can then use the algorithm to design a more suitable experiment, as was done with the multilayer sample, described in section 5.5. This shows the analytical power of the proposed workflow, which enables a focus on the data interpretation, rather than manipulation, as is often the case. Furthermore, as shown in section 5.3.1, such a procedure even works on an unknown buried morphology.

Many times, performing neutron scattering alone is not sufficient and additional information has to be obtained. X-ray based techniques are often used, as they are generally available in laboratories. Further development of the algorithm lies in connecting the X-ray reflectivity and off-specular scattering with neutron one, where the same algorithm is used to simultaneously analyze and fit the data of both contrasts. This way, the models would be narrowed down much quicker and more precisely. Some parts of the algorithm would have to be modified for that, especially the resolution part, which is negligible but finite for X-rays. Furthermore, it could be expanded into the so-called grazing incidence small angle scattering, where the same kind of concerns about the absolute scattering intensity and the interpretation of different features are present. In such experiments, the Θ_y and θ_f are both changed in order to obtain information in (q_x, q_y) or (q_z, q_y) space. This would however require major modifications, as the equations have been integrated over the Θ_y angle in equation 2.63. Then all the grazing incidence geometry could be united under one common calculation procedure, giving the ability to simulate data in advance, decide on the proper technique, apply for experiment and then analyze the data, all within the common framework. The work required for that is substantial, as it is not only of computational or programming effort, but would require verification and comparison of calculations to real measurements, as was done in this work.

Even though the polymer bilayer breakup was studied in the past, the OSS specifically allows one to focus on the buried polymer-polymer interface. We have been able to show that preannealing has a clear influence on the overlying interface. For the two thinnest preannealed bottom layers ($d_{\mathrm{PS}} = 131\,\text{Å}$ and $d_{\mathrm{PS}} = 237\,\text{Å}$), the observed in-plane cutoff length fits with the ones predicted for capillary waves. For the thicker PS layers, the cutoff length departs significantly from it. This is due to the breakup of the layer, as the top PMMA layer is dewetting. The observations would not have been possible without the combined use of specular reflectivity and off-specular scattering, as the latter provides additional constraints to the structural parameters. Two contributions to the OSS intensity were identified and quantified, the holes in the top layer and the interfacial roughness. A system with a thin d-PS of thickness $d_{\mathrm{dPS}} = 155\,\text{Å}$ with the top h-PMMA layer of thickness $d_{\mathrm{hPMMA}} = 1700\,\text{Å}$ of lower molecular weight was prepared and studied as a function of time. The molecular weight was chosen in such a way as to speed up the process and cover the whole evolution from the beginning to complete breakup via heterogeneous nucleation. When the top thickness was further increased

($d > 3000\,\text{Å}$), the expected bulk behavior was reached, the bottom thin d-PS dewetting without influencing the thick layer.

A polymer trilayer was measured with the aim of observing the symmetric instability of the two interfaces of a thin layer of d-PMMA, sandwiched between two identical thick layers of h-PS. It is hypothesized that a sufficiently thin layer ($< 200\,\text{Å}$) will undergo spinodal decomposition and that the two interfaces will break up in anti-phase, finally forming droplets of d-PMMA, surrounded by the h-PS. The samples were successfully measured and analyzed as shown in section 5.4. However, our subsequent analysis with the OSS program has shown that the intensity scattered only from 2 interfaces is weak and furthermore modulated by the scattering coming from the holes in the top layer. We have come up with a solution to overcome the problem by preparing a multilayer with 3 such repeating units of thick / thin / thick layers. As shown qualitatively in section 5.5, the simulations differ for the two, anti-phase and in-phase, cases. As previously, different contributions to OSS have to be understood separately and then reconstructed into a final spectrum. Due to the amount of free parameters (8 layers), this task has presently not been solved, nevertheless it remains an exciting outlook for the use of the algorithm and the contribution to fundamental polymer physics.

Overall, off-specular neutron scattering has been successfully implemented and used for quantitative analysis of experimental data of various systems. It has been demonstrated that the described algorithm works on several different model systems of known and unknown morphology. It also constrains the specular fits, not only providing additional information, but almost acting as additional contrast. In the future, the technique will be fully employed and our studies have elucidated the importance of fully understanding the different components that form the off-specular scattering intensity.

Acknowledgements

First of all, I would like to thank my academic supervisor, Prof. Michele Sferrazza, for giving me the oportunity to work on this very interesting project, combining experimental, theoretical and numerical work. During my independent working process, I have not only learned a lot of new things about soft matter, scattering and chemistry, but also how to work for long periods of time on a single problem. Every single detail has been a problem on its own and an important piece in the whole puzzle that was created almost from scratch.

The thesis would have been completely impossible if it had not been for my ILL supervisor, Philipp Gutfreund, who has wholeheartedly and unconditionally supported me for the last three years with his optimism and unbelievable patience. I hope that he will benefit from me at least a fraction of what I have benefited from him. Thank you, Philipp!

All the hardest parts from the first two chapters of the thesis are entirely a product of an eye-opening and fruitful collaboration with Boris P. Toperverg, an amazing scientist and man. Since he was only occasionally coming from Saint Petersburg, he could easily bear a nickname *White (K)night*. With his immense experience and knowledge, he showed me how to approach things without prejudice and analytically, step-by-step.

A huge thanks also goes to all the people at ILL with whom I have spent a lot of time, both at and outside of work. Without them, the stay in Grenoble would have been boring and meaningless. Andrea Tummino has helped me become a person I am today and I will never forget our late-night discussions. With Nico Carl we have in reality known each other only for a year and a half, but it feels like I would have known him for my whole life. I guess this tells everything about what I think of him. Bruno Tomasello helped me get by with our long and exciting, existentialist discussions. I hope Sebastian and Tetiana do not mind my random visits to their office, which became especially regular when I was working on one of those details mentioned earlier. At least to Sebastian I managed to compensate the damage by regularly buying him beers (he did the same of course). Even though he was here only during my first year, I have to mention Samuel Freeman, with whom I shared the office and had some great times and discussions. Emily Lin was here just for a few months, but left a big mark on my stay in Grenoble.

I had the opportunity to collaborate with some great people and their contribution should not be forgotten. Firstly, Andrew Wildes, who was always willing to offer advice, either technical or psychological. Due to his involvement in the project, he is also my *never to be* co-supervisor. Secondly, Henry Fischer, who once himself worked on a similar task, but with X-rays and with solid state physics. I have to thank Yuri Gerelli, who is in general a great person and has helped me quite a bit, both with work-related problems, as well as other things that came by. I have to mention all my friends from Slovenia, Peter Šušnjar, Matija Strniša, Vid Jan and Matija Oblak. Even though they were not

physically here, they were always in my mind.

I would never have done it without my parents. Even though they have luckily not helped me with the thesis, it seems that they have successfully taught me how to distinguish good from bad and beautiful from ugly, a task so great, making every other contribution insignificant. Please consider this thesis as a big thanks for everything!

During these three years, I have also had the greatest pleasure of seeing my brother transform from a child into a man. A thing already amazing on its own, but just like that, he also managed to learn German in the meantime. Thank you for regularly visiting me and speaking to me during the PhD, as I was constantly reminded that being a teenager is much harder than doing a PhD. I am really looking forward to spending more time with him in the future.

Finally, without doubt, the most important and biggest thanks goes to my girlfriend Vita, who has moved to France, found a job, then found another job, and then did everything again, just because of me. And she does not even seem upset that all this time I was doing just scattering. Maybe the thesis will serve as a proof that I was not just goofing around. This shows how unbelievable she is and how much she has supported me during these three great and (sometimes not) exciting years of our lives.

Bibliography

1. Pattie, R. W. *et al.* Measurement of the Neutron Lifetime Using a Magneto-Gravitational Trap and in Situ Detection. *Science* **360,** 627–632 (May 2018).
2. Sivia, D. S. *Elementary Scattering Theory: For X-Ray and Neutron Users* ISBN: 978-0-19-922867-6 978-0-19-922868-3 (Oxford University Press, Oxford ; New York, 2011).
3. Parratt, L. G. Surface Studies of Solids by Total Reflection of X-Rays. *Physical Review* **95,** 359–369 (July 1954).
4. Vidal, B. & Vincent, P. Metallic Multilayers for x Rays Using Classical Thin-Film Theory. *Applied Optics* **23,** 1794–1801 (1984).
5. Hamley, I. W. & Pedersen, J. S. Analysis of Neutron and X-Ray Reflectivity Data. I. Theory. *Journal of applied crystallography* **27,** 29–35 (1994).
6. Névot, L. & Croce, P. Caractérisation des surfaces par réflexion rasante de rayons X. Application à l'étude du polissage de quelques verres silicates. *Revue de Physique Appliquée* **15,** 761–779 (Mar. 1980).
7. Strazielle, C. & Benoit, H. Some Thermodynamic Properties of Polymer-Solvent Systems. Comparison between Deuterated and Undeuterated Systems. *Macromolecules* **8,** 203–205 (Mar. 1975).
8. Salditt, T., Münster, C., Mennicke, U., Ollinger, C. & Fragneto, G. Thermal Fluctuations of Oriented Lipid Membranes by Nonspecular Neutron Reflectometry. *Langmuir* **19,** 7703–7711 (Sept. 2003).
9. Gerelli, Y., Porcar, L. & Fragneto, G. Lipid Rearrangement in DSPC/DMPC Bilayers: A Neutron Reflectometry Study. *Langmuir* **28,** 15922–15928 (Nov. 2012).
10. Russell, T. X-Ray and Neutron Reflectivity for the Investigation of Polymers. *Materials Science Reports* **5,** 171–271 (Jan. 1990).
11. Sinha, S. K., Sirota, E. B., Garoff, S. & Stanley, H. B. X-Ray and Neutron Scattering from Rough Surfaces. *Physical Review B* **38,** 2297–2311 (Aug. 1988).
12. Daillant, J. & Bélorgey, O. Surface Scattering of x Rays in Thin Films. Part I. Theoretical Treatment. *The Journal of Chemical Physics* **97,** 5824 (1992).
13. Holy, V., Kubena, J., Ohli, I., Lischka, K., Plotz, W., *et al.* X-Ray Reflection from Rough Layered Systems. *Physical review B* **47,** 15896 (1993).
14. Sinha, S. K. Reflectivity Using Neutrons or X-Rays? A Critical Comparison. *Physica B: Condensed Matter* **173,** 25–34 (1991).

15. Zabel, H., Siebrecht, R. & Schreyer, A. Neutron Reflectometry on Magnetic Thin Films. *Physica B: Condensed Matter* **276-278,** 17–21 (Mar. 2000).
16. Toperverg, B. P. Specular Reflection and Off-Specular Scattering of Polarized Neutrons. *Physica B: Condensed Matter. Proceeding of the Third International Workshop on Polarised Neutrons* **297,** 160–168 (Mar. 2001).
17. Majkrzak, C. F., O'Donovan, K. V. & Berk, N. F. Polarized Neutron Reflectometry. *NIST Center for Neutron Research, http://www. ncnr. nist. gov/instruments/ng1refl/pnrchapti. pdf* (2004).
18. Jablin, M. S. *et al.* In-Plane Correlations in a Polymer-Supported Lipid Membrane Measured by Off-Specular Neutron Scattering. *Physical Review Letters* **106** (Mar. 2011).
19. Pynn, R. Neutron Scattering by Rough Surfaces at Grazing Incidence. *Physical Review B* **45,** 602–612 (Jan. 1992).
20. Hunter, J. D. Matplotlib: A 2D Graphics Environment. *Computing in Science Engineering* **9,** 90–95 (May 2007).
21. Kim, S., Hewlett, S. A., Roth, C. B. & Torkelson, J. M. Confinement Effects on Glass Transition Temperature, Transition Breadth, and Expansivity: Comparison of Ellipsometry and Fluorescence Measurements on Polystyrene Films. *The European Physical Journal E* **30,** 83 (Sept. 2009).
22. Craster, R. V. & Matar, O. K. Dynamics and Stability of Thin Liquid Films. *Reviews of Modern Physics* **81,** 1131–1198 (Aug. 2009).
23. Reiter, G. *et al.* Thin Film Instability Induced by Long-Range Forces. *Langmuir* **15,** 2551–2558 (Mar. 1999).
24. Seemann, R. *et al.* Dynamics and Structure Formation in Thin Polymer Melt Films. *Journal of Physics: Condensed Matter* **17,** S267–S290 (Mar. 2005).
25. Sharma, A. & Reiter, G. Instability of Thin Polymer Films on Coated Substrates: Rupture, Dewetting, and Drop Formation. *Journal of Colloid and Interface Science* **178,** 383–399 (Mar. 1996).
26. Xie, R., Karim, A., Douglas, J. F., Han, C. C. & Weiss, R. A. Spinodal Dewetting of Thin Polymer Films. *Physical Review Letters* **81,** 1251 (1998).
27. Langer, J. & Bar-on, M. Theory of Early-Stage Spinodal Decomposition. *Annals of Physics* **78,** 421–452 (June 1973).
28. Cahn, J. W. On Spinodal Decomposition. *Acta Metallurgica* **9,** 795–801 (Sept. 1961).
29. Kim, J., Lee, S., Choi, Y., Lee, S.-M. & Jeong, D. Basic Principles and Practical Applications of the Cahn–Hilliard Equation. *Mathematical Problems in Engineering* **2016,** 1–11 (2016).
30. Herminghaus, S. Wetting and Dewetting in Bio-Related Systems. *Journal of Physics: Condensed Matter* **17,** S637–S637 (Mar. 2005).
31. Pototsky, A., Bestehorn, M., Merkt, D. & Thiele, U. Alternative Pathways of Dewetting for a Thin Liquid Two-Layer Film. *Physical Review E* **70** (Aug. 2004).

32. Pototsky, A., Bestehorn, M., Merkt, D. & Thiele, U. Morphology Changes in the Evolution of Liquid Two-Layer Films. *The Journal of Chemical Physics* **122,** 224711 (June 2005).
33. Peschka, D. *et al.* Signatures of Slip in Dewetting Polymer Films. *Proceedings of the National Academy of Sciences* **116,** 9275–9284 (May 2019).
34. Napolitano, S. & Wübbenhorst, M. The Lifetime of the Deviations from Bulk Behaviour in Polymers Confined at the Nanoscale. *Nature Communications* **2,** 260 (Mar. 2011).
35. Housmans, C., Sferrazza, M. & Napolitano, S. Kinetics of Irreversible Chain Adsorption. *Macromolecules* **47,** 3390–3393 (May 2014).
36. He, Q., Narayanan, S., Wu, D. T. & Foster, M. D. Confinement Effects with Molten Thin Cyclic Polystyrene Films. *ACS Macro Letters,* 999–1003 (Aug. 2016).
37. Nieto Simavilla, D., Huang, W., Housmans, C., Sferrazza, M. & Napolitano, S. Taming the Strength of Interfacial Interactions via Nanoconfinement. *ACS Central Science* **4,** 755–759 (June 2018).
38. Gin, P. *et al.* Revealed Architectures of Adsorbed Polymer Chains at Solid-Polymer Melt Interfaces. *Physical Review Letters* **109** (Dec. 2012).
39. Pynn, R., Baker, S. M., Smith, G. & Fitzsimmons, M. Off-Specular Scattering in Neutron Reflectometry. *Journal of Neutron Research* **7,** 139–158 (1999).
40. Stone, V. W., Arys, X., Legras, R. & Jonas, A. M. An Attempt to Separate Roughness from Interdiffusion in the Interfacial Broadening between Two Immiscible Polymers. *Macromolecules* **33,** 3031–3041 (2000).
41. M ller-Buschbaum, P. Dewetting and Pattern Formation in Thin Polymer Films as Investigated in Real and Reciprocal Space. *Journal of Physics: Condensed Matter* **15,** R1549–R1582 (Sept. 2003).
42. Lauter, V., Lauter, H., Glavic, A. & Toperverg, B. in *Reference Module in Materials Science and Materials Engineering* (Elsevier, 2016). ISBN: 978-0-12-803581-8.
43. Ott, F. & Kozhevnikov, S. Off-Specular Data Representations in Neutron Reflectivity. *Journal of Applied Crystallography* **44,** 359–369 (Apr. 2011).
44. Adlmann, F. A. *et al. Överlåtaren* : A Fast Way to Transfer and Orthogonalize Two-Dimensional off-Specular Reflectivity Data. *Journal of Applied Crystallography* **49,** 2091–2099 (Dec. 2016).
45. Schlomka, J.-P. *et al.* X-Ray Diffraction from Si/Ge Layers: Diffuse Scattering in the Region of Total External Reflection. *Physical Review B* **51,** 2311–2321 (Jan. 1995).
46. Nylander, T. *et al.* Neutron Reflectometry to Investigate the Delivery of Lipids and DNA to Interfaces (Review). *Biointerphases* **3,** FB64–FB82 (June 2008).
47. Tatur, S., Maccarini, M., Barker, R., Nelson, A. & Fragneto, G. Effect of Functionalized Gold Nanoparticles on Floating Lipid Bilayers. *Langmuir* **29,** 6606–6614 (June 2013).
48. Kiessig, H. Interferenz von Röntgenstrahlen an Dünnen Schichten. *Annalen der Physik* **402,** 769–788 (1931).
49. Fermi, E. & Zinn, W. H. Reflection Of Neutrons On Mirrors. **70,** 103 (1946).

50. Saerbeck, T. *et al.* Recent Upgrades of the Neutron Reflectometer D17 at ILL. *Journal of Applied Crystallography* **51,** 249–256 (Apr. 2018).
51. Gutfreund, P. *et al.* Towards Generalized Data Reduction on a Chopper-Based Time-of-Flight Neutron Reflectometer. *Journal of Applied Crystallography* **51,** 606–615 (June 2018).
52. *X-Ray and Neutron Reflectivity* (eds Daillant, J. & Gibaud, A.) ISBN: 978-3-540-88587-0 978-3-540-88588-7 (Springer Berlin Heidelberg, Berlin, Heidelberg, 2009).
53. Born, M. & Wolf, E. *Principles of Optics: Electromagnetic Theory of Propagation, Interference and Diffraction of Light* 7th expanded ed. ISBN: 978-0-521-64222-4 978-0-521-63921-7 (Cambridge University Press, Cambridge ; New York, 1999).
54. Als-Nielsen, J. & McMorrow, D. *Elements of Modern X-Ray Physics* 2nd ed. ISBN: 978-0-470-97395-0 978-0-470-97394-3 (Wiley, Hoboken, 2011).
55. Dorner, B. & Wildes, A. R. Some Considerations on Resolution and Coherence Length in Reflectrometry †. *Langmuir* **19,** 7823–7828 (Sept. 2003).
56. Holỳ, V. & Baumbach, T. Nonspecular X-Ray Reflection from Rough Multilayers. *Physical Review B* **49,** 10668 (1994).
57. Mikulik, P. *X-Ray Reflectivity from Planar and Structured Multilayers* PhD thesis (1997).
58. Daillant, J. & Bélorgey, O. Surface Scattering of x Rays in Thin Films. Part II. Experiments on Thin Soap Films. *The Journal of Chemical Physics* **97,** 5837 (1992).
59. Tolan, M. *X-Ray Scattering from Soft-Matter Thin Films* ISBN: 978-3-540-65182-6 (Springer Berlin Heidelberg, Berlin, Heidelberg, 1999).
60. Falconer, K. *Fractal Geometry: Mathematical Foundations and Applications* ISBN: 978-0-470-01385-4 978-0-470-84861-6 978-0-470-84862-3 (John Wiley & Sons, Ltd, Chichester, UK, Sept. 2003).
61. Cubitt, R., Saerbeck, T., Campbell, R. A., Barker, R. & Gutfreund, P. An Improved Algorithm for Reducing Reflectometry Data Involving Divergent Beams or Non-Flat Samples. *Journal of Applied Crystallography* **48,** 2006–2011 (Dec. 2015).
62. Toperverg, B. Off-Specular Polarized Neutron Scattering from Magnetic Fluctuations in Thin Films and Multilayers. *Applied Physics A* **74,** s1560–s1562 (Dec. 2002).
63. *FORTRAN Numerical Recipes: Modeling Data* 2nd ed (ed Press, W. H.) ISBN: 978-0-521-43064-7 978-0-521-57439-6 (Cambridge University Press, Cambridge [England] ; New York, 1996).
64. Reiter, G. & Napolitano, S. Possible Origin of Thickness-Dependent Deviations from Bulk Properties of Thin Polymer Films. *Journal of Polymer Science Part B: Polymer Physics* **48,** 2544–2547 (Dec. 2010).
65. Ruderer, M. A. & Müller-Buschbaum, P. Morphology of Polymer-Based Bulk Heterojunction Films for Organic Photovoltaics. *Soft Matter* **7,** 5482–5493 (June 2011).
66. *Non-Equilibrium Phenomena in Confined Soft Matter: Irreversible Adsorption, Physical Aging and Glass Transition at the Nanoscale* (ed Napolitano, S.) ISBN: 978-3-319-21947-9 978-3-319-21948-6 (Springer International Publishing, Cham, 2015).

67. O'Shaughnessy, B. & Vavylonis, D. Non-Equilibrium in Adsorbed Polymer Layers. *Journal of Physics: Condensed Matter* **17,** R63–R99 (Jan. 2005).
68. Sferrazza, M. *et al.* Evidence for Capillary Waves at Immiscible Polymer/Polymer Interfaces. *Physical review letters* **78,** 3693 (1997).
69. Tolan, M. *et al.* Evidence for Capillary Waves on Dewetted Polymer Film Surfaces: A Combined X-Ray and Atomic Force Microscopy Study. *Physical Review Letters* **81,** 2731–2734 (Sept. 1998).
70. Jiang, Z. *et al.* Evidence for Viscoelastic Effects in Surface Capillary Waves of Molten Polymer Films. *Physical Review Letters* **98** (May 2007).
71. Sferrazza, M, Xiao, C, Bucknall, D. G. & Jones, R. A. L. Interface Width of Low-Molecular-Weight Immiscible Polymers. *Journal of Physics: Condensed Matter* **13,** 10269–10277 (Nov. 2001).
72. *PVC Handbook* (eds Wilkes, C. E., Summers, J. W., Daniels, C. A. & Berard, M. T.) ISBN: 978-3-446-22714-9 978-1-56990-379-7 (Hanser, Munich ; Cincinnati, 2005).
73. Scriven, L. E. Physics and Applications of Dip Coating and Spin Coating. *MRS Online Proceedings Library Archive* **121** (1988).
74. Hall, D. B., Underhill, P. & Torkelson, J. M. Spin Coating of Thin and Ultrathin Polymer Films. *Polymer Engineering & Science* **38,** 2039–2045 (Dec. 1998).
75. Schubert, D. W. Spin Coating as a Method for Polymer Molecular Weight Determination. *Polymer bulletin* **38,** 177–184 (1997).
76. Lawrence, C. J. The Mechanics of Spin Coating of Polymer Films. *Physics of Fluids* **31,** 2786 (1988).
77. Schubert, D. W. & Dunkel, T. Spin Coating from a Molecular Point of View: Its Concentration Regimes, Influence of Molar Mass and Distribution. *Materials Research Innovations* **7,** 314–321 (Oct. 2003).
78. Jellison, G. Data Analysis for Spectroscopic Ellipsometry. *Thin Solid Films* **234,** 416–422 (Oct. 1993).
79. Neuwald, U., Hessel, H. E., Feltz, A., Memmert, U. & Behm, R. J. Initial Stages of Native Oxide Growth on Hydrogen Passivated Si(111) Surfaces Studied by Scanning Tunneling Microscopy. *Applied Physics Letters* **60,** 1307–1309 (Mar. 1992).
80. Morita, M., Ohmi, T., Hasegawa, E., Kawakami, M. & Ohwada, M. Growth of Native Oxide on a Silicon Surface. *Journal of Applied Physics* **68,** 1272–1281 (Aug. 1990).
81. Shull, K. R., Mayes, A. M. & Russell, T. P. Segment Distributions in Lamellar Diblock Copolymers. *Macromolecules* **26,** 3929–3936 (July 1993).
82. Semenov, A. N. Scattering of Statistical Structure of Polymer/Polymer Interfaces. *Macromolecules* **27,** 2732–2735 (May 1994).
83. Russell, T. P., Hjelm, R. P. & Seeger, P. A. Temperature Dependence of the Interaction Parameter of Polystyrene and Poly(Methyl Methacrylate). *Macromolecules* **23,** 890–893 (Feb. 1990).
84. Israelachvili, J. N. *Intermolecular and Surface Forces* Third edition. OCLC: 249272556. ISBN: 978-0-12-391927-4 978-0-12-375182-9 (Elsevier, Academic Press, Amsterdam, 2011).

85. Helfand, E. & Tagami, Y. Theory of the Interface between Immiscible Polymers. II. *The Journal of Chemical Physics* **56,** 3592–3601 (Apr. 1972).
86. Nieto Simavilla, D., Huang, W., Housmans, C., Sferrazza, M. & Napolitano, S. Taming the Strength of Interfacial Interactions via Nanoconfinement - Supplemental Information. *ACS Central Science* **4,** 755–759 (June 2018).
87. Vrij, A. Possible Mechanism for the Spontaneous Rupture of Thin, Free Liquid Films. *Discussions of the Faraday Society* **42,** 23–33 (Jan. 1966).
88. Bischof, J., Scherer, D., Herminghaus, S. & Leiderer, P. Dewetting Modes of Thin Metallic Films: Nucleation of Holes and Spinodal Dewetting. *Physical Review Letters* **77,** 1536–1539 (Aug. 1996).
89. Müller-Buschbaum, P. *et al.* Dewetting of Thin Polymer-Blend Films Examined with GISAS. *Physica B: Condensed Matter* **283,** 53–59 (June 2000).
90. Cabral, J. T. & Higgins, J. S. Spinodal Nanostructures in Polymer Blends: On the Validity of the Cahn-Hilliard Length Scale Prediction. *Progress in Polymer Science* **81,** 1–21 (June 2018).
91. Langer, J. S., Bar-on, M. & Miller, H. D. New Computational Method in the Theory of Spinodal Decomposition. *Physical Review A* **11,** 1417–1429 (Apr. 1975).
92. Sferrazza, M. *et al.* Interfacial Instability Driven by Dispersive Forces: The Early Stages of Spinodal Dewetting of a Thin Polymer Film on a Polymer Substrate. *Physical review letters* **81,** 5173 (1998).
93. de Silva, J. P. *et al.* Switching Layer Stability in a Polymer Bilayer by Thickness Variation. *Physical Review Letters* **98** (June 2007).
94. de Silva, J. P., Cousin, F., Wildes, A. R., Geoghegan, M. & Sferrazza, M. Symmetric and Asymmetric Instability of Buried Polymer Interfaces. *Physical Review E* **86** (Sept. 2012).
95. Tolan, M *et al.* X-Ray Diffraction from Laterally Structured Surfaces: Total External Reflection and Grating Truncation Rods. *Europhysics Letters (EPL)* **20,** 223–228 (Oct. 1992).
96. Doi, M. & Edwards, S. F. *The Theory of Polymer Dynamics* Reprinted. *International Series of Monographs on Physics* **73.** OCLC: 845169495. ISBN: 978-0-19-852033-7 (Clarendon Press, Oxford, 2007).
97. James, D. *et al.* Measurement of Molecular Mixing at a Conjugated Polymer Interface by Specular and Off-Specular Neutron Scattering. *Soft Matter* **11,** 9393–9403 (2015).
98. Seemann, R, Herminghaus, S & Jacobs, K. Gaining Control of Pattern Formation of Dewetting Liquid Films. *Journal of Physics: Condensed Matter* **13,** 4925–4938 (May 2001).

A Additional off-specular scattering plots

A.1 Preannealed and non-preannealed samples

This is a continuation of measurements and DWBA calculations from chapter 4. All the measurements are the same as presented before, just this time in $(p_i - p_f, p_i + p_f)$ space. They were transformed from the $(\lambda, \theta_i + \theta_f)$ space in the same way as the measurements. The samples are marked according to table 4.3.

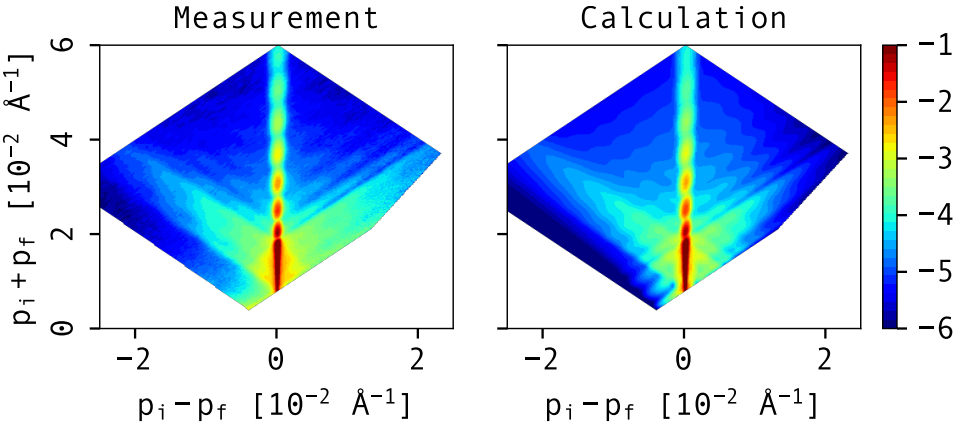

Figure A.1: Sample A1, thickness of dPS, $d_{\mathrm{dPS}} = 850\,\text{Å}$.

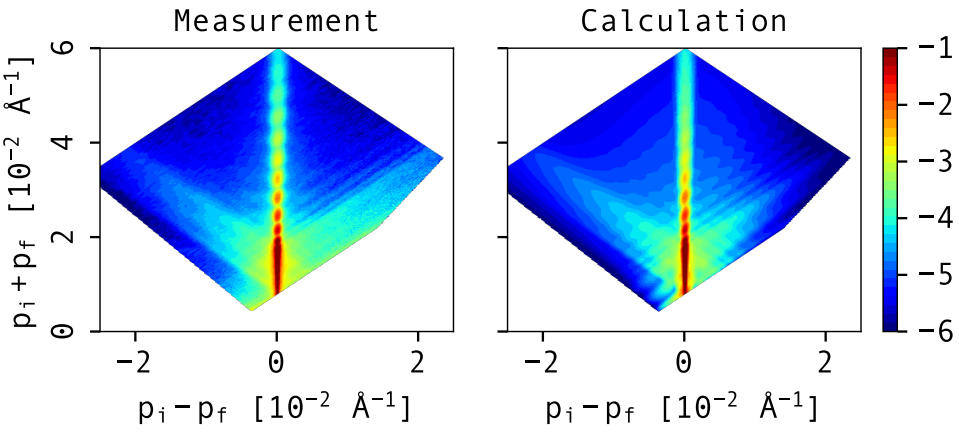

Figure A.2: Sample A, thickness of dPS, $d_{\mathrm{dPS}} = 892\,\text{Å}$.

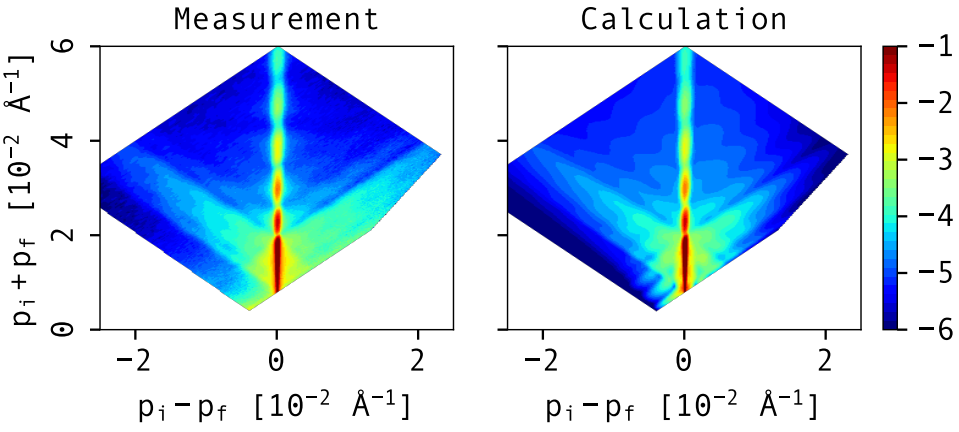

Figure A.3: Sample C1, thickness of dPS, $d_{\mathrm{dPS}} = 626\,\text{Å}$.

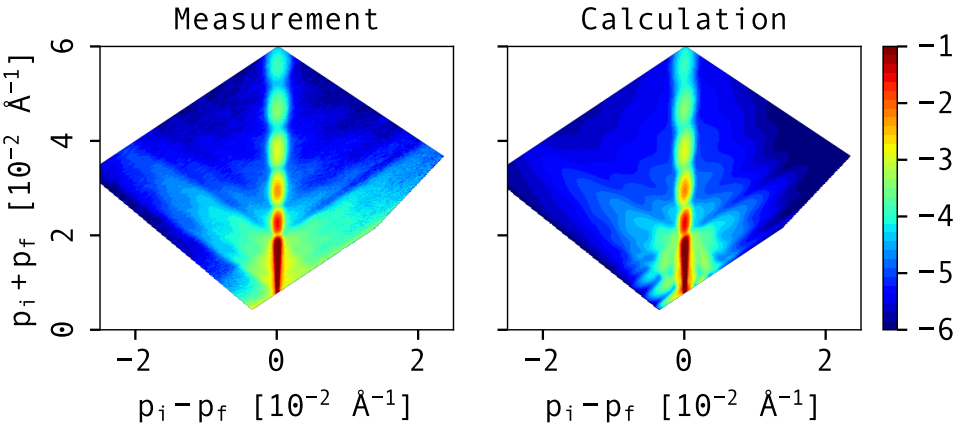

Figure A.4: Sample C, thickness of dPS, $d_{\mathrm{dPS}} = 640\,\text{Å}$.

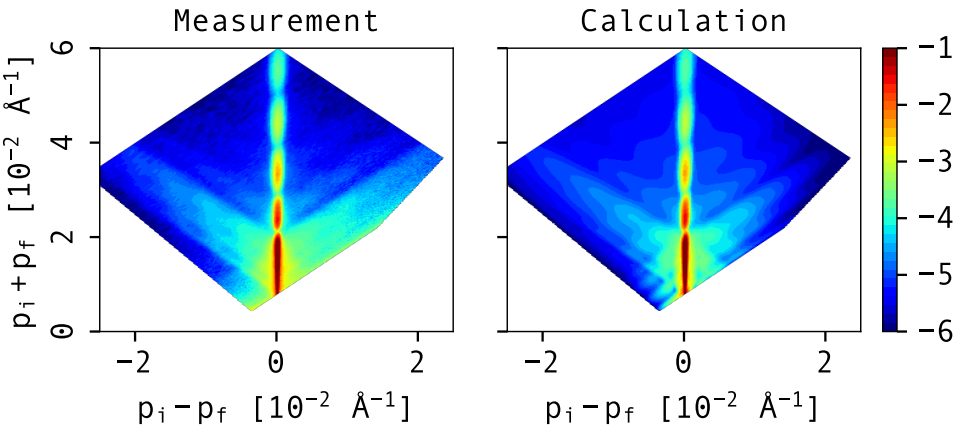

Figure A.5: Sample D1, thickness of dPS, $d_{\mathrm{dPS}} = 527\,\text{Å}$.

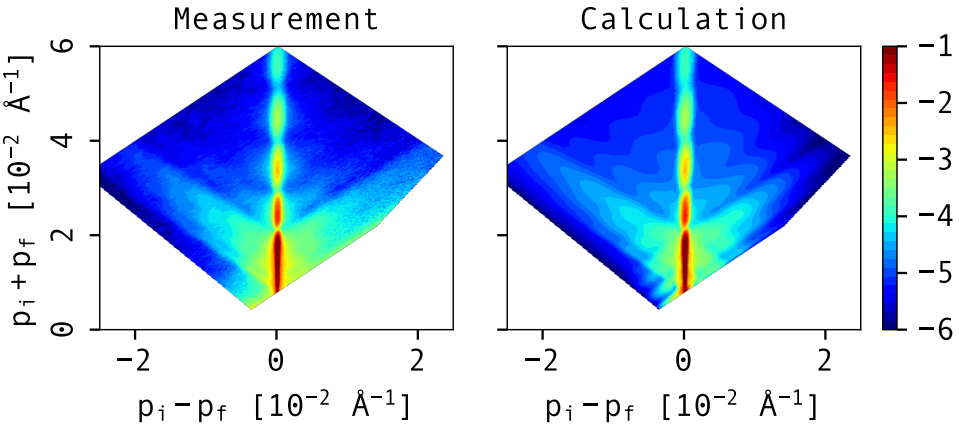

Figure A.6: Sample D, thickness of dPS, $d_{\mathrm{dPS}} = 514\,\text{Å}$.

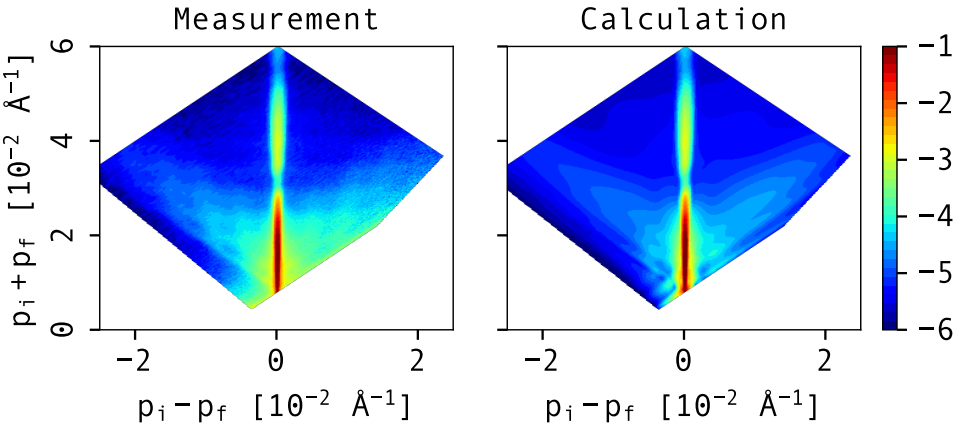

Figure A.7: Sample E1, thickness of dPS, $d_{\mathrm{dPS}} = 236\,\text{Å}$.

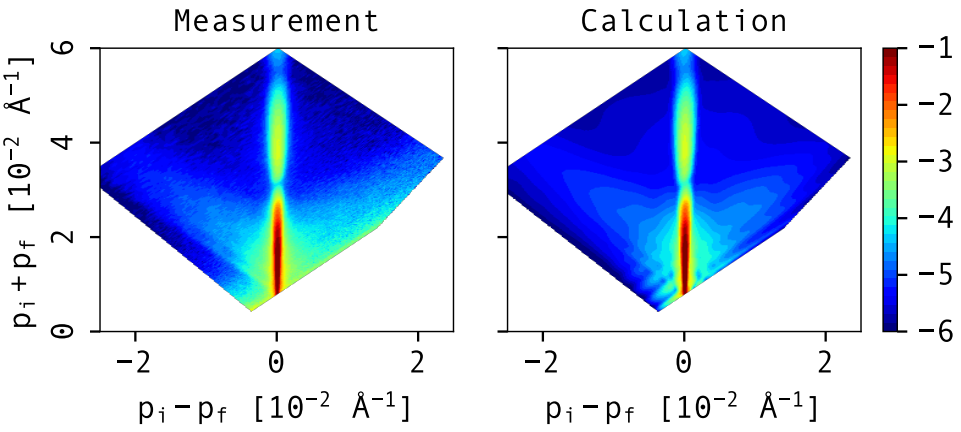

Figure A.8: Sample E, thickness of dPS, $d_{\mathrm{dPS}} = 237\,\text{Å}$.

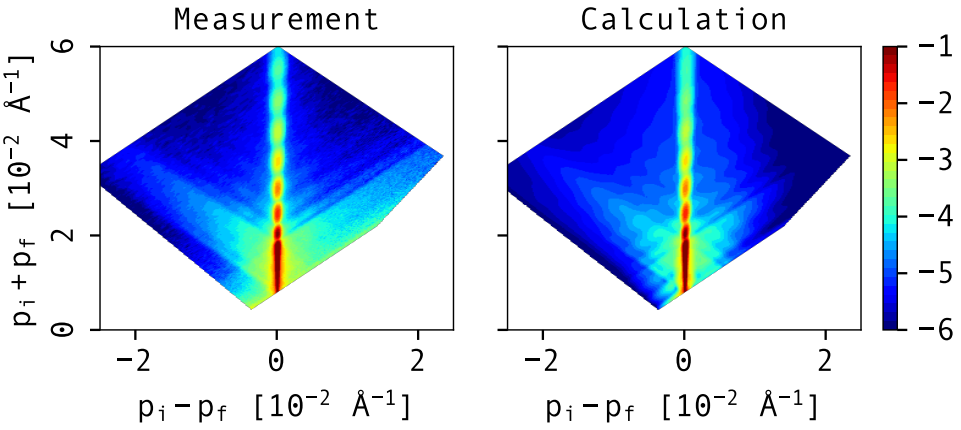

Figure A.9: Sample B2, thickness of dPS, $d_{\mathrm{dPS}} = 1261\,\text{Å}$.

A.2 Bilayer with thin capping layer

Additional calculations from section 5.2 are shown here. Same parameters were used as described in the text. The measurements are presented either in $(\lambda, \theta_i + \theta_f)$ or $(p_i - p_f, p_i + p_f)$ space.

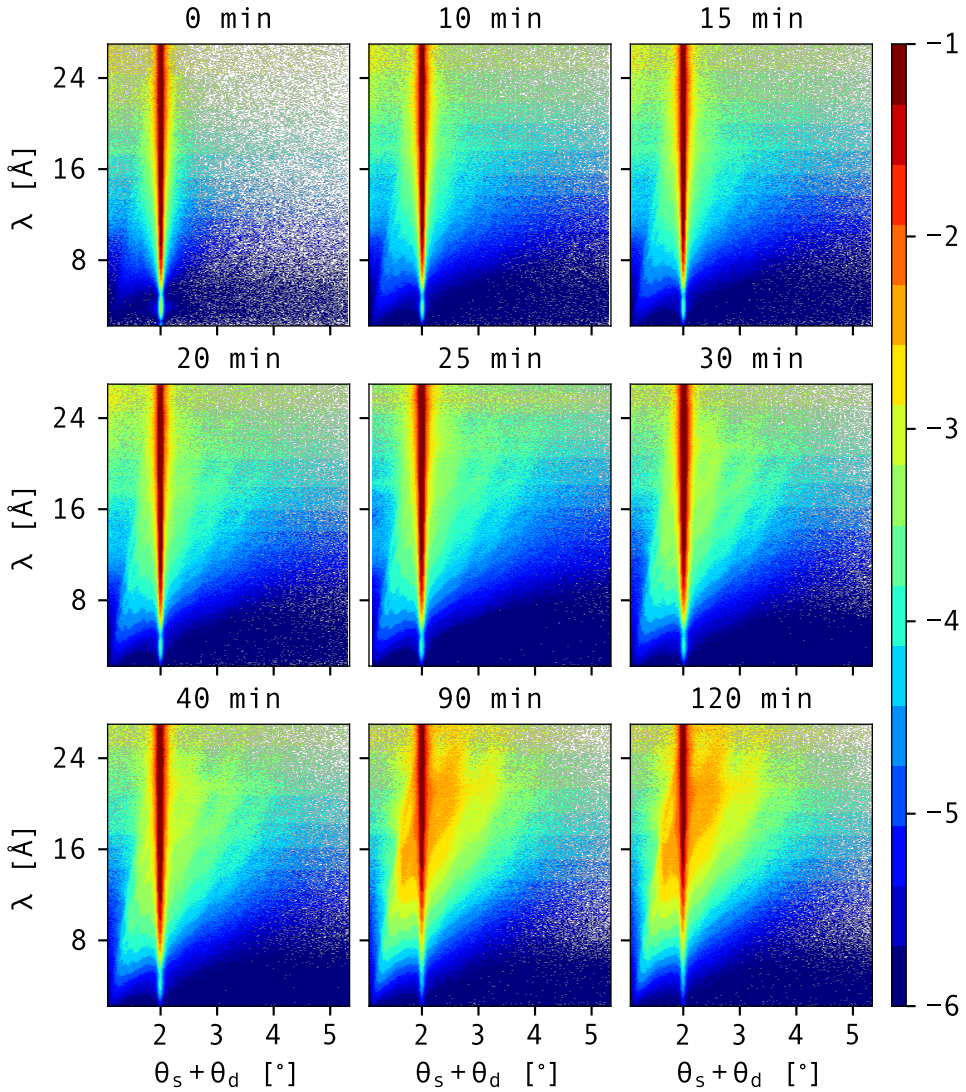

Figure A.10: All the 2D measurements of the DW4 PS/PMMA bilayer sample with thin capping layer in the $(\theta_i + \theta_f, \lambda)$ space.

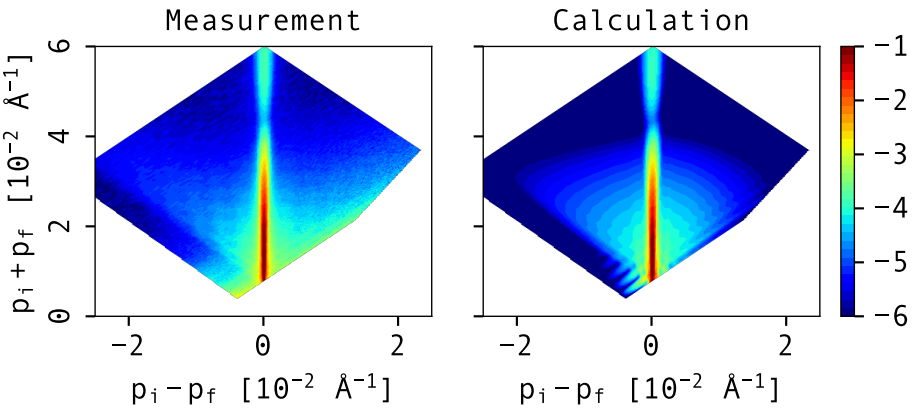

Figure A.11: Comparison of measurement to DWBA calculation for the $t = 10$ min annealed sample DW4 in the $(p_i - p_f, p_i + p_f)$ space.

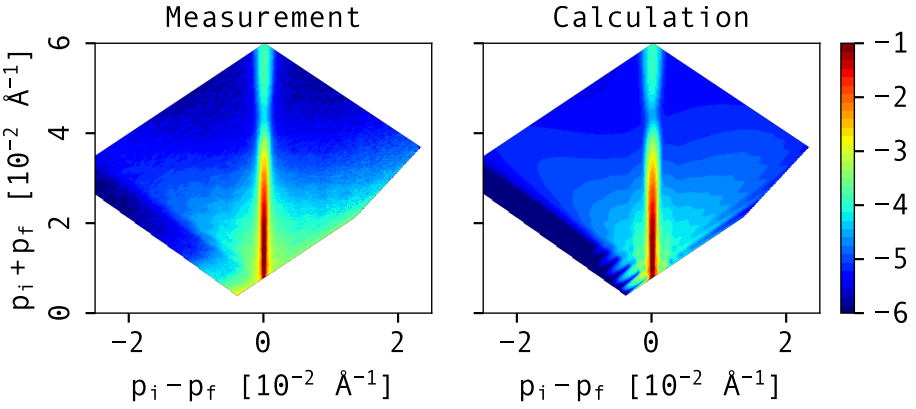

Figure A.12: Comparison of measurement to DWBA calculation for the $t = 15$ min annealed sample DW4 in the $(p_i - p_f, p_i + p_f)$ space.

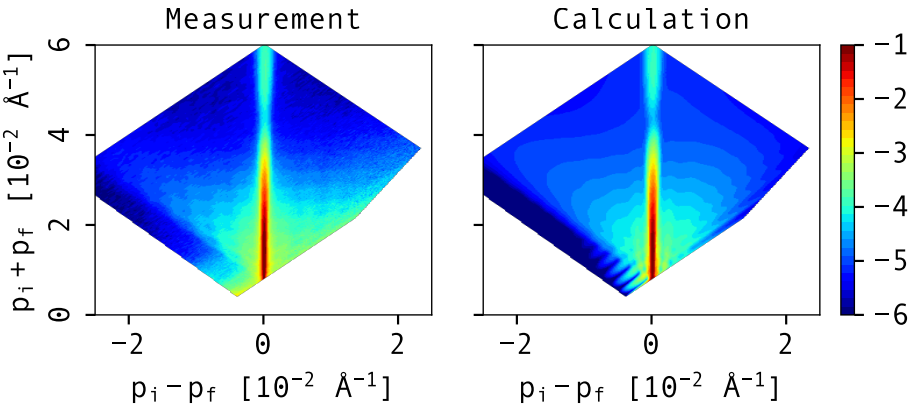

Figure A.13: Comparison of measurement to DWBA calculation for the $t = 20$ min annealed sample DW4 in the $(p_i - p_f, p_i + p_f)$ space.

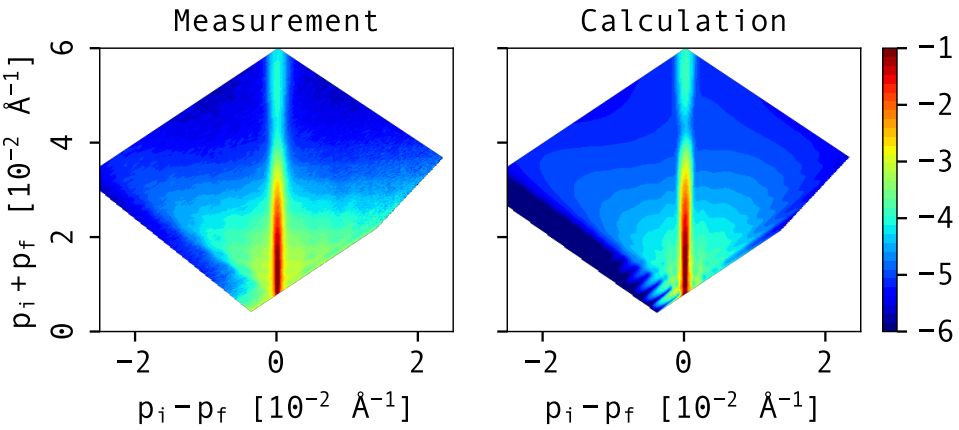

Figure A.14: Comparison of measurement to DWBA calculation for the $t = 40\,\text{min}$ annealed sample DW4 in the $(p_i - p_f, p_i + p_f)$ space.

A.3 Bilayers with thick capping layer

Samples PMMA 3500 and PMMA BI, presented in sections 5.3 and 5.3.1 are presented below in $(p_i - p_f, p_i + p_f)$ space. The parameters used are the same and the space in calculations was transformed in the same way as for the experimental data.

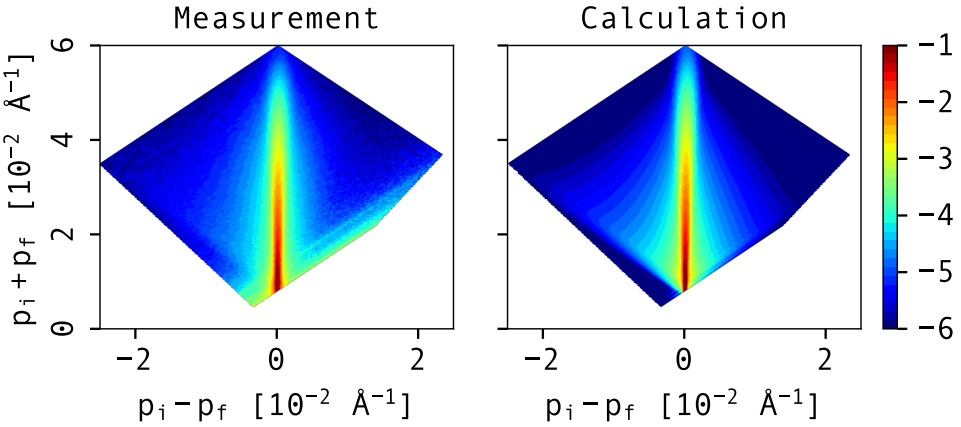

Figure A.15: PMMA 3500 in $(p_i - p_f, p_i + p_f)$ space, $t_{\text{annealing}} = 0\,\text{min}$.

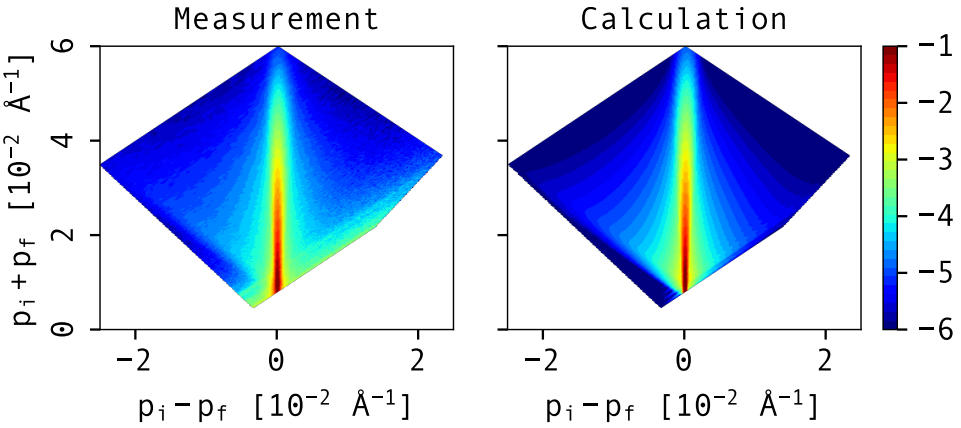

Figure A.16: PMMA 3500 in $(p_i - p_f, p_i + p_f)$ space, $t_{\text{annealing}} = 5\,\text{min}$.

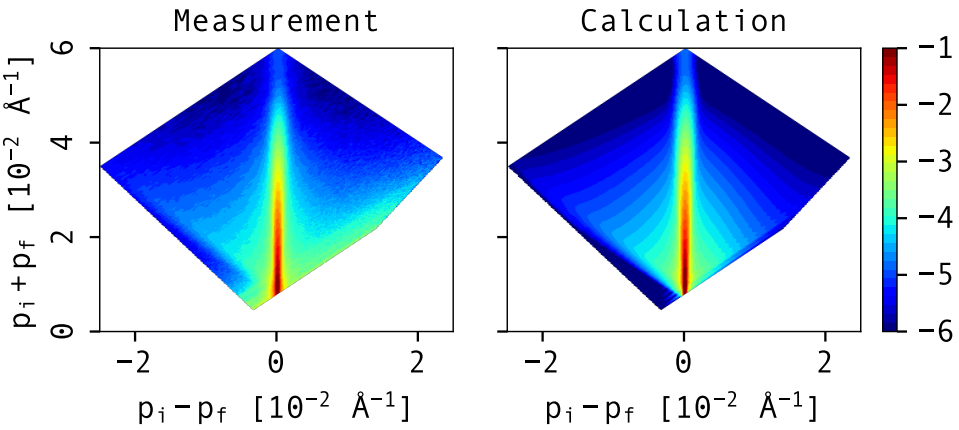

Figure A.17: PMMA 3500 in $(p_i - p_f, p_i + p_f)$ space, $t_{\text{annealing}} = 10\,\text{min}$.

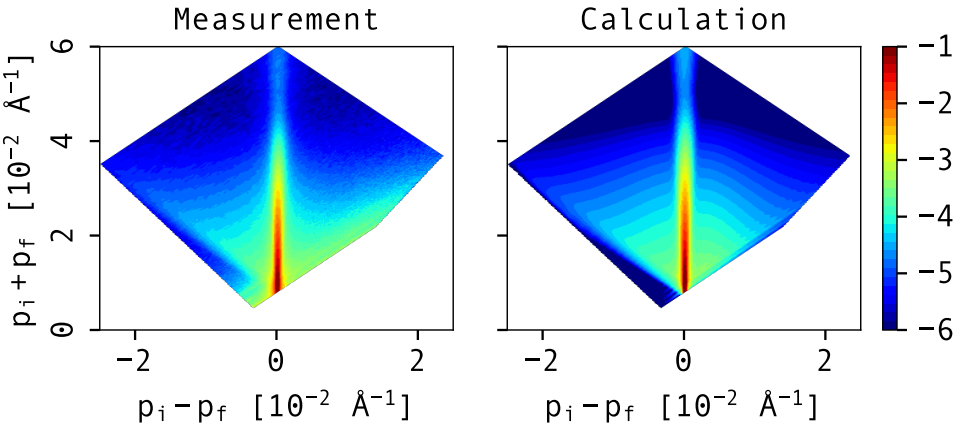

Figure A.18: PMMA 3500 in $(p_i - p_f, p_i + p_f)$ space, $t_{\text{annealing}} = 15\,\text{min}$.

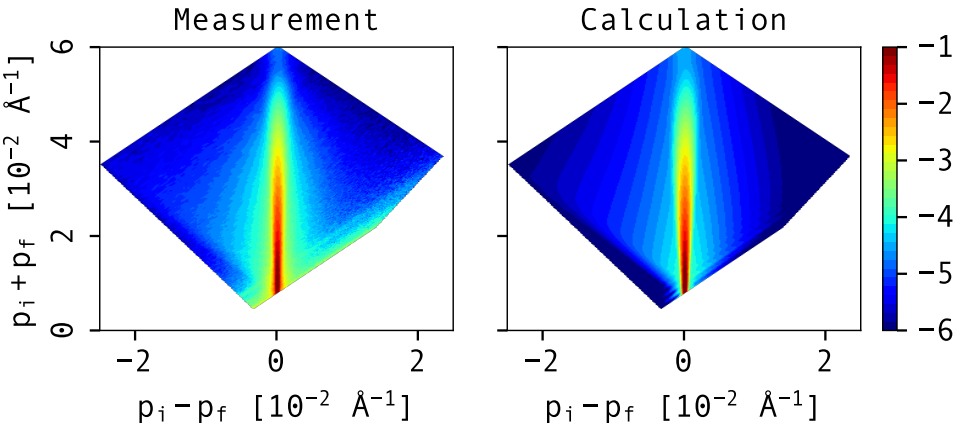

Figure A.19: PMMA BI in $(p_i - p_f, p_i + p_f)$ space, $t_{\text{annealing}} = 0\,\text{min}$.

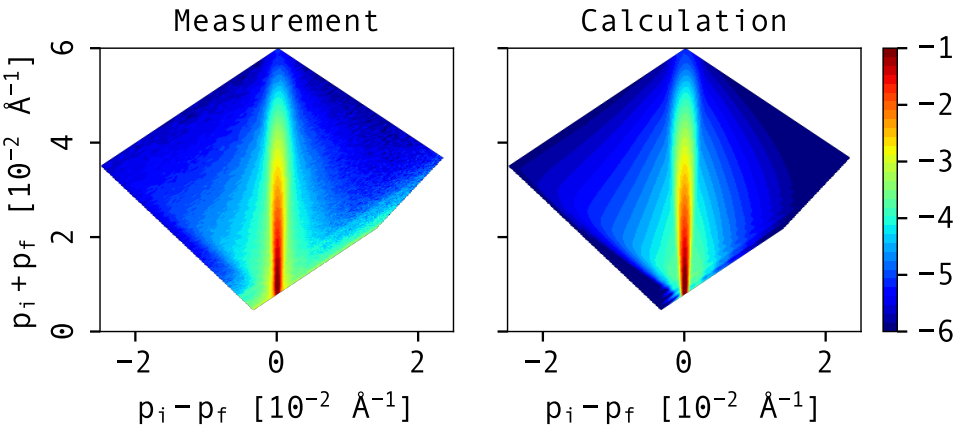

Figure A.20: PMMA BI in $(p_i - p_f, p_i + p_f)$ space, $t_{\text{annealing}} = 5\,\text{min}$.

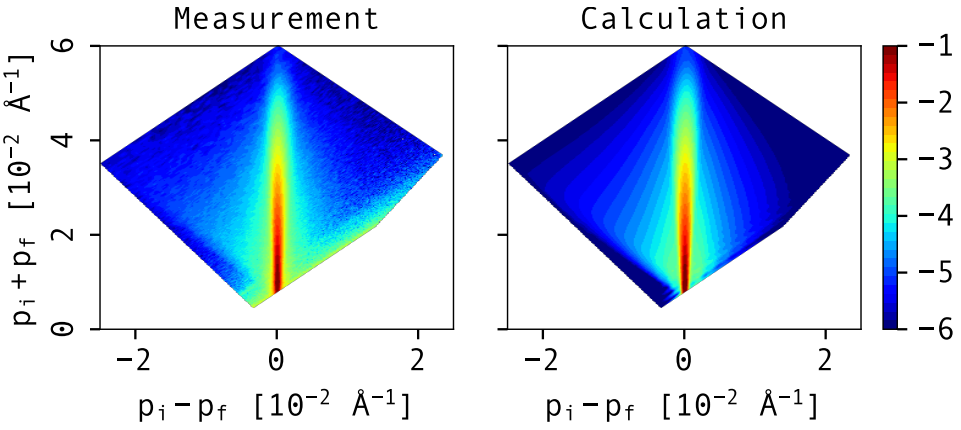

Figure A.21: PMMA BI in $(p_i - p_f, p_i + p_f)$ space, $t_{\text{annealing}} = 10\,\text{min}$.